NONEQUILIBRIUM RADIATION AND CHEMISTRY MODELS FOR AEROCAPTURE VEHICLE FLOWFIELDS

LANGLEY GRANT IN-18-CR

26779 p. 140

aerospace engineering department

Semiannual Progress Report
February 1991 -- June 1991

TEXAS A&M UNIVERSITY

TAMRF Report No. 6382-91-02

July 1991

(NASA-CR-188546) NONEQUILIBRIUM RADIATION AND CHEMISTRY MODELS FOR AEROCAPTURE VEHICLE FLOWFIELDS Semiannual Progress Report, Feb. - Jun. 1991 (Texas A&M Univ.) 140 p CSCL 22B G3/18

N91-27191

Unclas 0026779

NASA Grant No. NAG-1-1003

Leland A. Carlson
Professor of Aerospace Engineering
Texas A&M University
College Station, TX 77843-3141

TEXAS ENGINEERING EXPERIMENT STATION

NONEQUILIBRIUM RADIATION AND CHEMISTRY MODELS FOR AEROCAPTURE VEHICLE FLOWFIELDS

Semiannual Progress Report

February 1991 -- June 1991

TAMRF Report No. 6382-91-02

July 1991

NASA Grant No. NAG-1-1003

Leland A. Carlson
Professor of Aerospace Engineering
Texas A&M University
College Station, TX 77843-3141

NONEQUILIBRIUM RADIATION AND CHEMISTRY MODELS FOR AEROCAPTURE VEHICLE FLOWFIELDS

I. Introduction

This report covers approximately the period February 1991 thru June 1991. The primary tasks during this period have been the development of a second order local thermodynamic nonequilibrium (LTNE) model for atoms, the continued development of vibrational nonequilibrium models, and the development of a new multicomponent diffusion model. In addition, studies comparing these new models with previous models and results have been conducted and reported.

II. Personnel

The staff associated with this project during the present reporting period have been Dr. Leland A. Carlson, Principal Investigator, and Thomas A. Gally and Derek Green, Graduate Research Assistants. It should be noted that Mr. Gally is currently supported by a NASA Graduate Student Researchers Fellowship from NASA Johnson Space Center and will use the results of his research on this project in his Ph.D. dissertation. He research during this period has been primarily associated with the development of nonequilibrium chemical and radiation models, multicomponent diffusion models, and the radiation coupled nonequilibrium viscous shock layer code. Mr. Green's work, which constituted the basis of of masters' thesis, has been primarily concerned with the development and incorporation into the VSL code of various vibrational nonequilibrium models. Mr. Green left the project in March to accept a position with Lockheed Engineering Services at NASA Johnson and received his M.Sc. degree in May. In addition, a departmentally supported graduate student, Rajeev Koteshwar, is conducting masters'

research on flowfields involving carbon species. While not directly related to the present project, it is anticipated that portions of his work will have applications to the present effort.

III. Discussion of Research Effort

As a result of the research during the present reporting period, the coupled viscous shock layer and radiative transfer method discussed and presented in the past report has been extended significantly. Specifically, three modifications and/or options have been incorporated into the computational method.

First, a complete vibrational energy equation has been added for the calculation of a third temperature, T_V, which describes the average vibrational energy state of all the diatomic species. This energy formulation also includes electron-vibrational coupling effects as well as vibration-tranlational coupling and coupled vibration-dissociation-vibration via the MCVDV model.

Second, a new multicomponent diffusional model has been developed and incorporated into the method which should yield improved values of diffusional mass and energy flux. While this method does assume that each electron diffuses with an ion, it does not assume that any of the diffusing species are "trace species." Finally, to improve the LTNE predictions and associated radiative flux, a two-step excitation model for atomic nitrogen has been formulated and developed.

Details concerning these models and extensions, along with results comparing them to previous models and formulations, are presented in detail in AIAA Paper 91-1463. This paper was presented by Mr. Gally at the AIAA 22nd Fluid Dynamics, Plasma Dynamics & Lasers Conference in June, and a copy of this paper is included in this report in Appendix I.

Briefly, the results for AFE and Martian return cases show that the use of a three temperature model including electron-vibrational coupling can lead to significant differences in the thermal profiles from those obtained with a two temperature model in which T_e is assumed equal to T_v. The effects on chemistry are not as noticable due to the fact that the T_v=T_e model tends to predict a temperature closest to the dominant energy for the flow conditions, i.e. closer to T_v in dissociation dominated flows and closer to T_e in ionization dominated flows. The differences in the thermal profiles for the two models result in differences of 20-30% in the radiative heat flux to the wall for the cases considered. These differences would be even more significant except that LTNE effects tend to inhibit emission from the regions of thermal nonequilibrium.

With respect to the diffusional models, comparision of results obtained with the new model with those from the simple constant Lewis number multi-component model did not exhibit any signficant differences. This consequence was probably the result of the fact that for the conditions investigated the flowfield was dominantly binary.

However, the second order LTNE model developed during this period did show differences from results obtained using the first order LTNE model developed previously. While both models predict similar total heat fluxes, the spectral content of the radiation is different. Radiation reaching the wall with the second order LTNE model shows a greater IR line contribution and less UV line center absorption. The electron impact excitation calculated for the second order LTNE model is faster by an order of magnitude than the previous rate. Using the faster rate with the first order model, however, closely reproduces much of the chemical behavior of the second order model. Again the reader is referred to Appendix I for further details.

As mentioned previously, various vibrational nonequilibrium and vibration-dissociation-vibration coupling

models have been investigated during this period; and the results of these studies constitute Mr. Green's masters' thesis, which is included in this report as Appendix II. In his MCVDV model with electron-vibrational coupling, Green included a diffusive correction term on the electron-vibrational coupling term similar to the factor used for translational-vibrational relaxation. As with the translation-vibrational relaxation factor, this term is intended to increase the relaxation time or decrease the amount of coupling between the electron energy and vibrational energy. Unfortunately, the form of the correction developed for the case where T_e and T_v are intially far apart has the opposite effect for shock layer conditions where T_e and T_v are intially close together in value behind the shock. For this reason, the suggested correction has been subsequently dropped from the model; and the results presented in AIAA 91-1463 are different than those in Appendix II.

As mentioned in the last progress report, the studies associated with shock precursor phenomena resulting from continuum photochemistry, photoexcitation, and photoionization phenomena were essentially completed during the last reporting period. However, these results have been summarized and presented by Scott Stanley in AIAA Paper 91-1465 at the AIAA 22nd Fluid Dynamics, Plasma Dynamics & Lasers Conference in June. A copy of this paper is included in this report as Appendix III.

IV. Publications

During this reporting period, the following publications, which were partially supported by this project, have been issued:

Carlson, L. A. and Gally, T. A., "Effect of Electron Temperature and Impact Ionization on Martian Return AOTV Flowfields," **Journal of Thermophysics and Heat Transfer**, Vol. 5, No. 1, January 1991, pp. 9-20.

Gally, T. A., Carlson, L. A., and Green, D., "A Flowfield Coupled Excitation and Radiation Model for Nonequilibrium Reacting Flows," AIAA Paper 91-1463, June 1991.

Stanley, S. A. and Carlson, L. A., "The Effects of Shock Wave Precursors Ahead of Hypersonic Entry Vehicles," AIAA Paper 91-1465, June 1991.

The first article is a revised version of a previous AIAA paper and is included in this report as Appendix IV. The other two papers are included as Appendices I and III respectively.

V. Future Efforts

During the next reporting period, it is planned to continue the development of the nonequilibrium radiating reacting shock layer model. The primary emphasis during this period will be on extending the existing models to air, While results are currently being obtained using an air model composed of eleven species and fifty reactions, the results are very preliminary and have not yet been analyzed. Also, further investigations as to the differences between two and three temperature models and between the first and second order atomic LTNE models will be conducted as well as investigations into appropriate reaction chemistry sets.

VI. Technical Monitor

The NASA technical monitor for this grant is Dr. Lin C. Hartung, Aerothermodynamics Branch, Space Systems Division, NASA Langley Research Center, Hampton, Virginia.

APPENDIX I

"A Flowfield Coupled Excitation and Radiation Model for Nonequilibrium Reacting Flows"

by

T. A. Gally, L. A. Carlson, and D. Green

AIAA Paper 91-1463

AIAA 91-1463

A Flowfield Coupled Excitation and Radiation Model for Nonequilibrium Reacting Flows

T. A. Gally, L. A. Carlson, and D. Green
Texas A&M University
College Station, Texas

AIAA 22nd Fluid Dynamics, Plasma Dynamics & Lasers Conference
June 24-26, 1991 / Honolulu, Hawaii

For permission to copy or republish, contact the American Institute of Aeronautics and Astronautics
370 L'Enfant Promenade, S.W., Washington, D.C. 20024

A Flowfield Coupled Excitation and Radiation Model for Nonequilibrium Reacting Flows

Thomas A. Gally*, Leland A. Carlson**
and
Derek Green†
Texas A&M University
College Station, Texas

Abstract

A second order method has been developed to correct a radiative transfer analysis for possible local thermodynamic nonequilibrium effects. This method uses a two species excitation model for nitrogen with chemical reaction rates obtained from the detailed atomic transition method of Kunc and Soon. Results obtained from this new method show more atomic line radiation that the authors' previous first order method. As improvements to the flowfield representation used in the computations, a full three temperature energy model has also been incorporated and a new multicomponent diffusional model developed.

Nomenclature

B_ν = black body function
c_p = specific heat at constant pressure
D = dissociation energy
$\mathcal{D}$ = binary diffusion coefficient
e = energy per unit mass
E = electronic state energy level
E_n = integro-exponential function of order n
$\mathcal{E}$ = electostatic field strength
F = external force per unit mass
g = degeneracy
h = enthalpy per unit mass
I = ionization energy
k = Boltzmann constant
K = absorption coefficient
m = particle mass
N = number density
p = pressure
q_r = radiative heat flux
Q = electronic partition function
Q_e = electron translational partition function
r = wall reflectivity
S = source function
T = temperature
u^j = mass averaged velocity components
U = diffusion velocity
x^j = coordinate axis
Z = Molecular charge
α = wall absorptivity
ϵ = wall emissivity
ϵ = magnitude of electron charge
η = heat conduction coefficient
ρ = density
σ = radiative cross section
τ = relaxation time
τ_ν = optical thickness
ν = frequency

subscripts
e = electron
f = forward rate (production)
pc = continuum process
pq = line process
r = reverse rate (depletion)
s, t = species
sh = value at shock
tr = translational
v = vibrational
w = value at wall
ν = frequency

Introduction

A great deal of interest has been placed recently on the design of aerobraking vehicles for use with both inter-orbit maneuvering and inter-planetary deceleration. In particular, a major goal of such experimental projects as the Aeroassist Flight Experiment (AFE) is the development of the computational tools for the accurate prediction of the aerodynamic environment which determines the heating and controllabilty of such vehicles. Both low speed inter-orbit and high speed inter-planetary missions will spend the aerobraking portion of their trajectories at very high, low density altititudes where previously developed space vehicles spent only short durations. Thus, the computational aerodynamic tools to be used must correctly handle the chemical, thermal and radiative nonequilibrium phenomena associated with low-density flows.

Previous work[1,2] concentrated on some aspects of the nonequilibrium nature of aerobraking flowfields. For example, the primary topic of discussion in Ref. 1 was electron-impact ionization rates. This chemical rate is important in both determining the amount of chemical nonequilibrium in the flow and in calculating the electron temperature, T_e. Existing rates in the literature varied over several orders of magnitude with accompanying differences in T_e profiles and wall radiative heating rates, which is a strong function of T_e. In Ref.2, the effects

---

* NASA Graduate Student Researcher, Student Member
** Professor Aerospace Engineering, Associate Fellow AIAA
† Graduate Research Assistant

Copyright ©1991 by the American Institute of Aeronautics and Astronautics, Inc. All rights reserved.

of thermodynamic nonequilibrium on the magnitude and nature of the radiative environment was investigated. Comparisons were made with the FIRE II flight test measurements and a wide range of possible mission profile conditions were investigated.

A number of topics for future work were identified from the previous work. First, a two-temperature, T_{tr} and T_e, model had been used exclusively in Refs. 1 and 2, in which it was assumed that $T_v = T_{tr}$. This model is probably accurate for the higher speed conditions above 12 km/sec where the flow is ionization dominated and few diatomic particles exist. However, at the lower speeds and particularly for the speeds associated with the AFE vehicle, the flowfield is dissociation dominated; and a separate vibrational energy equation can be expected to affect the total results. In addition, electron-vibrational coupling will affect the predicted T_e profile and thus the radiative environment. Second, diffusional phenomena seemed to significantly affect chemical nonequilibrium and also the extent of atomic thermodynamic nonequilibrium. Since the diffusional model then being used was determined to be inadequate, a new model was developed as described later. Finally, a new atomic local second order thermodynamic nonequilbrium model was conceived, which is a compromise between the simple and fast method used previously and the complex methods used by other authors.

Problem Formulation

The computational model used in this report is an extension of the coupled viscous shock layer (VSL) and radiative transfer method described in detail in Refs. 1 and 2. The VSL portion of the code originated as the VSL3DNQ[3] code developed at NASA Langley. After modifications were made to the thermodynamic and transport coefficient calculations and multi-temperature effects, T_{tr} and T_e, were included, the flowfield was iteratively coupled with the radiative transfer model of Nicolet[4] in a manner which included chemical and local thermodynamic nonequilibrium (LTNE) phenomena.

Three additional modifications have been made for the present paper. First, a vibrational energy equation has been added for the calculation of a third temperature, T_v, which describes the average vibrational energy state of all the diatomic species. Second, a new diffusional model has been developed to improve the calculation of the diffusional fluxes of mass and energy. Finally, to improve LTNE predictions, second order radiative correction factors similar to those used in Refs. 1 and 2 have been devolped for a two-step excitation model for atomic nitrogen.

Vibrational Temperature Model

The vibrational energy equation added to the VSL calulations has the following form for simple Cartesian coordinates.

$$\rho u^j c_{p_v} \frac{\partial T_v}{\partial x^j} = \frac{\partial}{\partial x^j}\left(\eta_v \frac{\partial T_v}{\partial x^j}\right) + \sum_s \rho_s U_s \frac{\partial h_{v_s}}{\partial x^j} \qquad (1)$$

$$+ \sum_s \rho_s A \frac{(e_{v_s}(T_{tr}) - e_{v_s})}{\tau_s} + \sum_s \rho_s \frac{(e_{v_s}(T_e) - e_{v_s})}{\tau_{e,s}}$$

$$+ \sum_s (e_{v_s} - E_s)\left(\frac{\partial \rho_s}{\partial t}\right)_f - \sum_s (e_{v_s} - G_s)\left(\frac{\partial \rho_s}{\partial t}\right)_r$$

In this equation, c_{p_v} is the frozen vibrational specific heat at constant pressure calculated from the species specific heats by $\sum_s c_{p_{v,s}} \rho_s / \rho$; and the vibrational termperature, T_v, represents the average vibrational energy of all the diatomic species. While multiple vibrational temperatures are often used, one for each vibrating species, it can be argued[5] that the vibrational-vibrational energy exchange rates are not well modeled by available methods; and, thus, results with multiple vibrational termparatures may not be meaningful. In addition, for the results with a nitrogen only gas presented in this report, there is only one dominant vibrator, N_2, the vibrational contribution from $N^+{}_2$ being small.

The translational-vibrational energy exchange model used is a modification of the non-preferential CVDV model described in Refs. 6 and 7. The terms involved with the $T_{tr} - T_v$ coupling model are the third, fifth and sixth on the right hand side of Eq. 1. The differences from the CVDV model occur, first, in the calculation of the relaxation time, τ_s. This relaxation time is that proposed by Park[8] which sums the relaxation time of Millikan and White[9], τ_s^{MW}, with a high temperature correction factor such that

$$\tau_s = \tau_s^{MW} + \frac{1}{c_s \sigma_v N_s}$$

where c_s is the average species molecular speed and σ_v is a limiting cross section calculated by[10]:

$$\sigma_s = 10^{-17}(50,000^\circ K/T_{tr})^2 \mathrm{cm}^2.$$

The second modification, also suggested by Park[10], is the inclusion of the multiplier A on the third right hand side term of Eq. 1. This multiplier attempts to correct the original Landau and Teller relaxation rate for high temperature diffusive effects and has the form

$$A = \left|\frac{T_{tr,sh} - T_v}{T_{tr,sh} - T_{v,sh}}\right|^{(3.5\, exp(-5000^\circ K/T_v)-1)}.$$

The electron-vibrational energy exchange is accounted for by the fourth right hand side term of Eq. 1 and is taken from the work of Lee[11] as curve fitted by Candler and Park[12]:

$$log(p_e \tau_e) = 7.50(log\, T_e)^2 - 57.0\, log\, T_e + 98.70$$

for $T_e < 7000^\circ K$, and

$$log(p_e \tau_e) = 2.36(log\, T_e)^2 - 17.9\, log\, T_e + 24.35$$

for $T_e \geq 7000^\circ K$.

Lee suggests a correcting factor for the electron-vibrational relaxation similar to the factor A used for translational-vibrational relaxation. As with the translation-vibrational relaxation factor,

this term is intended to increase the relaxation time or decrease the amount of coupling between the electron energy and vibrational energy. Unfortunately the form of the correction, developed for the case were T_e and T_v are initially far apart, has the opposite effect for our conditions where T_e and T_v are initially close together in value behind the shock. For this reason, the suggested correction has not been included in the present model and the calculated results may tend to show too much electron-vibrational coupling.

The electron-vibrational coupling factor must also be included in the electron temperature equation, which for this paper is the full electron/electronic energy equation described in Ref. 2. The electron/electronic energy equation is similar in form to Eq. 1 and includes the effects of conduction, convection, diffusion, chemical energy depletion, heavy particle-electron translation coupling, and now electron-vibrational coupling.

Diffusional Model

In the stagnation region of a blunt entry vehicle, large gradients in species concentration occur in the nonequilibrium region behind the shock front and in the thermal boundary layer near the wall. As a result, diffusion effects in these regions are generally important and need to be considered in the evaluation of mass and energy flux. There are currently a number of diffusional models commonly used including the multi-component models used by Moss[13] and Gnoffo et al.[14], the binary model[15] based upon the work of Fay and Kemp[16,17], and the constant Lewis number multi-component approximation of Ref. 18. The latter is the method originally incorporated into our VSL code.

While diffusional effects play an important role in the level of chemical nonequilibruim which can occur behind a shock wave, they can be seen most easily in the near wall, thermal boundary layer of most reentry flows. Although the flow in this region is at low normal velocities and the density is much greater than the other portions of the shock layer, the flow is typically not in equilibrium in this region; and in fact a significant level of dissociation is present on the surface of non-catalytic walls no matter how cool the surface may be. For catalytic walls, the associated high heating rates are due the diffusive flux of energy to the wall as a result of the large concentration gradients. In addition, due to the chemical nonequilibrium induced by diffusional effects, the simple atomic LTNE model used in the radiative analysis is also strongly affected by the amount of diffusion. As a result, a more accurate diffusional model has been developed and incorporated into the flowfield model. The development of this model follows.

If the effects of presure and thermal diffusion are neglected, the general diffusion velocity equation for a multicomponent gas is[19] for each species

$$\sum_t \frac{x_s x_t}{\mathcal{D}_{st}}(U_t - U_s) = \nabla x_s - \frac{\rho_s F_s}{p} + \frac{\rho_s}{\rho p}\sum_t \rho_t F_t. \quad (2)$$

In these equations, $\mathcal{D}_{st}$ is, to a first approximation, the binary diffusion coefficient for species s into species t, and F_s represents external forces acting upon species s. Note that while the above equations were obtained by Chapman and Cowling[19] for a single temperature gas (primarily due to the fact that the first approximation of Enskog for the Bolzmann equation assumes equilibrium between particles), a simple extension for multi-temperatures can be made if the pressure and concentrations are calculated using multi-temperature methods and the diffusion coefficients are determined using the appropriate temperatures. For the present method, T_e is used to calculate $\mathcal{D}_{st}$ if either of the colliding partners is an electron and T is used for heavy particle encounters.

If the externally applied force term is set equal to the electrostatic force due to charge separation, then $F_s = \epsilon \mathcal{E} Z_s/m_s$ and if charge separation is not large, it is approximately true that $\sum_t \rho_t F_t = 0$. Eq. 2 then becomes

$$\sum_t \frac{x_s x_t}{\mathcal{D}_{st}}(U_t - U_s) = \nabla x_s \quad (3)$$

for neutral particles and

$$\sum_t \frac{x_s x_t}{\mathcal{D}_{st}}(U_t - U_s) = \nabla x_s - \frac{N_s \epsilon \mathcal{E} Z_s}{p} \quad (4)$$

for ions and electrons. For most conditions of interest, the flowfield can be adequately described by only including singly charged positive ions in the flowfield chemistry model. In this case, to each ion diffusion equation there can be added N_s/N_e times the electron diffusion equation in order to eliminate the electrostatic force terms. The resulting ion diffusion equations are

$$\sum_t \frac{x_s x_t}{\mathcal{D}_{st}}(U_t - U_s) + \sum_t \frac{x_s x_t}{\mathcal{D}_{et}}(U_t - U_e) = \nabla x_s + \frac{N_s}{N_e}\nabla x_e. \quad (5)$$

To avoid the difficulty of specifying the strength of the electrostatic field, $\mathcal{E}$, in the electron diffusion equation, the ambipolar assumption is made that

$$\sum_{t=ions} N_t U_t = N_e U_e. \quad (6)$$

Note that this is not an assumption that the electrostatic term is small or zero, but rather that the electrostatic force for small charge separations is sufficiently large enough to cause the electrons to diffuse with an ion.

The original set of diffusional equations (Eq. 2) can easily be shown to be linear dependent; and an additional condition that the total diffusional mass flux be zero must also be used, i.e.

$$\sum_t \rho_t U_t = 0 \quad (7)$$

which replaces one of the original set. After the ambipolar assumption is used, the new set of equations (Eq. 3 for neutrals, Eq. 5 for ions, and Eq. 6 for electrons) are not strictly linear dependent, but are very poorly conditioned. Eq. 7 should still be used to replace one of the neutral or ionic equations.

For this paper, an additional simplification is used based upon the observation that since $U_s \sim U_e$ and $\mathcal{D}_{es} \gg \mathcal{D}_{st}$ for $t \neq e$, the neutral and ionic equations can be approximated by, respectively,

$$\sum_{t \neq e} \frac{x_s x_t}{\mathcal{D}_{st}} (U_t - U_s) = \nabla x_s$$

$$\sum_{t \neq e} \frac{x_s x_t}{\mathcal{D}_{st}} (U_t - U_s) = \nabla x_s + \frac{N_s}{N_e} \nabla x_e .$$

The above set is linear dependent which, with the two additional conditions of ambipolar diffusion and zero total diffusional mass flux, Eqs. 6 and 7, can be solved for all of the diffusional velocities, U_s.

Second Order Atomic LTNE Model

The flowfield solution is coupled with the radiative transport package of RADICAL[4] developed by Nicolet. The methods used by Niclolet assume that the electronic states of the radiating species are in local thermodynamic equilibrium (LTE) with each other and that their populations can be described by a Bolzmann distribution. A technique was developed previously[1,2] for correcting the RADICAL calculations to account for LTNE in both the atomic and molecular state populations.

The molecular electronic states populations are calculated using a quasi-steady approach similar to that described in Ref. 10; and, from these, LTNE population correction factors for the principle molecular radiation bands are obtained. Specifically, correction factors are determined for the N_2 Birge-Hopfield, first positive, and second positive bands, and for the N_2^+ first negative band. Ref. 2 should be consulted for more detail.

Also discussed in Ref. 2 is a first order atomic LTNE radiation correction. This model is predicated on the observation that for many monatomic gases, including argon, nitrogen, and oxygen, there exist one or more low lying ground energy states separated from the lowest excited energy state by an energy jump which is a large fraction of the ionization energy from the ground state. The model assumes that the excitation jump from ground to first excited state controls the ionization process, and that the excited states, because of their proximity in energy to the ionized state, are in equilibrium with the free electrons and ions. With this approach, the atomic nitrogen LTNE correction factor[1,2,20], which represents the ratio of the actual population in an excited state to that which would exist for a Boltzmann distribution, can be written as

$$\frac{N_{N^+} N_e Q_N \, exp(169000^\circ K/T_e)}{N_N Q_{N^+} Q_e} .$$

The above assumptions and resulting approximation are extremely simple to calculate and implement. At the other end of the spectrum are the methods of Park[8] and Kunc and Soon[21] which handle possible LTNE effects by performing detailed state population calculations under the quasi-steady assumption. Park's and Kunc's methods differ in the treatment of the free electrons and ions; Kunc et al. allow the free ions and electron populations to be determined as part of the solution, allowing LTNE to occur only as a consequence of radiative state depletion, while Park uses the ion and electron population calculated from the flowfield solution, allowing nonequilibrium chemistry to affect bound state populations. Either way, the detailed methods are computationally intensive and are not suitable for a radiative coupled solution if computational usage is a consideration.

After extensively reviewing the work on argon of Foley and Clarke[22] and Nelson[23] and the air and nitrogen work of Park[8], Kunc and Soon[21], and others, it was decided to develop a second order LTNE model for high temperature nitrogen by subdividing atomic nitrogen into two species. The first, termed N_g, for N ground, represents the nitrogen atoms in the first three low lying electronic states of nitrogen. The second, termed N^* or N excited, represents those nitrogen atoms populating the remaining upper electronic states. The relative densities of these subspecies will then be determined by appropriate reaction rates between themselves, N^+, e^-, etc and the electronic states of each are assumed to be in local thermodynamic equilibrium (LTE). It is believed that this approach has the potential to be a significant improvement over the present model in that it will allow a finite rate of ionization from excited states while retaining the fundamental two step ionization process. In addition, by determining the excited state number densities directly from the flowfield computation, the appropriate atomic LTNE factors are directly obtainable and more accurate.

The thermodynamic state of the two species, N_g and N^*, are determined by the standard methods used for monoatomic gases:

$$Q_{N_g} = \sum_{p=1}^{3} g_p e^{-E_p/kT_e}$$

$$Q_{N^*} = \sum_{p=4}^{max} g_p e^{-(E_p - E_4)/kT_e}$$

$$Q_N = Q_{N_g} + Q_{N^*} e^{-E_4/kT_e}$$

$$h_{N_g} = \frac{5}{2} \frac{kT}{m_N} + \frac{1}{m_N Q_{N_g}} \sum_{p=1}^{3} g_p E_p e^{-E_p/kT_e} + h^\circ_{N_g}$$

$$h_{N^*} = \frac{5}{2} \frac{kT}{m_N} + \frac{1}{m_N Q_{N^*}} \sum_{p=4}^{max} g_p (E_p - E_4) e^{-(E_p - E_4)/kT_e} + h^\circ_{N^*}$$

where the zero point energies are, $h^\circ_{N_g} = h^\circ_N = 3.36 \times 10^{11}$ ergs/gm and $h^\circ_{N^*} = h^\circ_{N_g} + E_4/m_N = 1.05 \times 10^{12}$ ergs/gm. The collision cross sections for both species, needed to calculate viscous transport properties, are assumed to be the same as for the original gas, N.

As mentioned earlier, new reactions must be specified to relate the two new species, N_g and N^*. These reactions are:

$$N_g + e^- = N^* + e^-$$
$$N_g + e^- = N^+ + 2e^-$$
$$N^* + e^- = N^+ + 2e^-$$

It was decided to use the method for calculating detailed excitation rates given in Ref. 21. A computer program was written which calculated the individual rates for each allowed transition process and computed effective rates for the above reaction equations assuming local thermodynamic equilibrium exists between the excited states grouped into each species. Results were obtained for a number of electron temperatures and then curve fit as shown in Fig. 1. These rates are part of the complete chemical reaction set shown in Table 2.

The radiative transport model must also be modified to account for the LTNE populations of N_g and N^* relative to each other. Under the assumption of a radiating tangent slab, the heat flux to a surface can be calculated as, assuming a non-emitting precursor:

$$-q_{r_\nu}(x) = 2\pi \int_0^{\tau_{\nu,sh}} sgn(t_\nu - \tau_\nu) S_\nu E_2(|t_\nu - \tau_\nu|) dt_\nu$$
$$- 2E_3(\tau_\nu)\pi \left(\epsilon_w B_{\nu,w} - 2\tau_w \int_0^{\tau_{\nu,sh}} E_2(t_\nu) S_\nu dt_\nu \right)$$

where τ_ν is the optical thickness determined by

$$\tau_\nu = \int_0^x K_\nu dy.$$

The absorption and source functions used in these expressions are the sum of all radiative contributs at the frequency ν.

Absorption coefficients derived from either theory or experiment are normally expressed as the product of the absorbing state number density and a radiative cross section:

$$K_{\nu_{pc}} = N_p \sigma_{pc}(\nu)$$

or by assuming a Bolzmann distribution exists between the electronic states,

$$(K_{\nu_{pc}})_{LTE} = N_N \left(\frac{g_p e^{-E_p/kT_e}}{Q_N} \sigma_{pc}(\nu) \right) = N_N \sigma'_{pc}(\nu).$$

Thus, an absorption coefficient using the actual state number density, N_p, can be obtained from one calculated assuming LTE by

$$K_{\nu_{pc}} = \frac{N_p}{(N_p)_{LTE}} (K_{\nu_{pc}})_{LTE}$$

where

$$\frac{N_p}{(N_p)_{LTE}} = \frac{N_p}{N_N} \frac{Q_N}{g_p e^{-E_p/kT_e}}$$

It is desired to have the LTNE corrections in terms of the known number density populations, N_g and N^*. If state p is one of the low lying states and since we have assumed these states are in LTE each other,

$$N_p = N_g \frac{g_p e^{-E_p/kT_e}}{Q_{N_g}}$$

and

$$\frac{N_p}{(N_p)_{LTE}} = \frac{N_{N_g}}{N_N} \frac{Q_N}{Q_{N_g}} = \frac{N_{N_g}}{(N_{N_g})_{LTE}}$$

Similarly, if p is one of the excited states,

$$N_p = N^* \frac{g_p e^{-(E_p - E_4)/kT_B}}{Q_{N^*}}$$

and

$$\frac{N_p}{(N_p)_{LTE}} = \frac{N_{N^*}}{N_N} \frac{Q_N}{Q_{N^*} e^{-E_4/kT_e}} = \frac{N_{N^*}}{(N_{N^*})_{LTE}}$$

The absorption coefficient for atomic line radiation is similar in form to that for the continuum process, but uses a radiative cross section which is a function of both the absorbing, p, and the emitting state, q.

$$K_{\nu_{pq}} = N_p \sigma_{pq}(\nu)$$

However, since the number density dependence is only with the absorbing state, the LTNE corrections described above for continuum radiation also apply to the line radiation.

The source function at thermodynamic equilibrium is equal to the black body, B_ν.

$$(S_{\nu_{pc}})_{LTE} = (S_{\nu_{pq}})_{LTE} = B_\nu = \frac{2h\nu^3}{c^2}(e^{h\nu/kT_e} - 1)$$

The source function for atomic continuum processes under LTNE conditions is given by[24,25]:

$$S_{\nu_{pc}} = \frac{(N_p)_E}{N_p} \frac{2h\nu^3}{c^2} \left(e^{h\nu/kT_e} - \frac{(N_p)_E}{N_p} \right)^{-1}$$
$$= \frac{(N_p)_E}{N_p} \frac{e^{h\nu/kT_e} - 1}{e^{h\nu/kT_e} - \frac{(N_p)_E}{N_p}} (S_{\nu_{pc}})_{LTE}$$

where the subscript E indicates a number density for state p calculated by assuming that state is in thermodynamic equilibrium with the free electrons and ions. Thus, if I is the ionization energy,

$$(N_p)_E = N_{N^+} N_e \frac{g_p e^{-(E_p - I)/kT_e}}{Q_{N^+} Q_e}$$

It can further be observed that when p is a low lying state $e^{h\nu/kT_e} \gg (N_p)_E/N_p$ and $e^{h\nu/kT_e} \gg 1$ while for the highly excited states, $(N_p)_E/N_p \simeq 1$. Thus

$$S_{\nu_{pc}} \simeq \frac{(N_p)_E}{N_p}(S_{\nu_{pc}})_{LTE}$$

As before, the LTNE correction can be written in term of the known number densities so that if p is one of the ground states,

$$\frac{(N_p)_E}{N_p} = \frac{N_{N^+}N_e}{N_{N_g}}\frac{Q_{N_g}e^{I/kT_e}}{Q_{N^+}Q_e} = \frac{(N_{N_g})_E}{N_{N_g}}$$

while if p is an excited state,

$$\frac{(N_p)_E}{N_p} = \frac{N_{N^+}N_e}{N_{N^*}}\frac{Q_{N^*}e^{(I-E_4)/kT_e}}{Q_{N^+}Q_e} = \frac{(N_{N^*})_E}{N_{N^*}}$$

The source function for the radiative transition from state q to state p under LTNE conditions is[20,21]:

$$\begin{aligned} S_{\nu_{pq}} &= \frac{N_q}{N_p}\frac{(N_p)_{LTE}}{(N_q)_{LTE}}\frac{2h\nu^3}{c^2}\left(e^{h\nu/kT_e} - \frac{N_q}{N_p}\frac{(N_p)_{LTE}}{(N_q)_{LTE}}\right)^{-1} \\ &= \frac{N_q}{N_p}\frac{(N_p)_{LTE}}{(N_q)_{LTE}}\frac{e^{h\nu/kT_e}-1}{e^{h\nu/kT_e} - \frac{N_q}{N_p}\frac{(N_p)_{LTE}}{(N_q)_{LTE}}}(S_{\nu_{pq}})_{LTE} \end{aligned}$$

If the transition is between two excited states, then, since it has been assumed that these states are in thermodynamic equilibrium, the LTNE source function becomes identical to that for LTE. If the transition is between an excited state and a ground state, it can be approximated that $e^{h\nu/kT_e} \gg 1$ and $e^{h\nu/kT_e} \gg N_q(N_p)_{LTE}/N_p(N_q)_{LTE}$ so that it is approximately true that

$$\begin{aligned} S_{\nu_{pq}} &= \frac{N_q}{N_p}\frac{(N_p)_{LTE}}{(N_q)_{LTE}}(S_{\nu_{pq}})_{LTE} \\ &= \frac{N_{N^*}}{N_{N_g}}\frac{(N_{N_g})_{LTE}}{(N_{N^*})_{LTE}}(S_{\nu_{pq}})_{LTE} \end{aligned}$$

Discussion of Results

Several sets of results have been obtained using the models presented in the previous sections. In all cases, these results are for the stagnation streamline on a vehicle having a 2.3 meter nose radius, utilize ninety-nine points between the wall and shock front, and use a nitrogen freestream. For those cases which assume that excited electronic states are in equilibrium with the free ions and electrons, the nonequilibrium chemistry is shown on Table 1. For those cases utitilizing the second order local thermodynamic nonequilibrium model for atoms, the corresponding nonequilibrium chemistry model is shown on Table 2. In addition, the wall has been assumed to be radiatively black, noncatalytic to atomic recombination, fully catalytic to ionic recombination and at a temperature of 1650°K. This wall temperature was selected to insure significant cool wall thermal effects and is representative of the maximum termperature of nonablating surfaces. However, it is recognized that for the higher speed case considered the cummulative head load associated with the mission profile dictates the use of ablative surfaces and higher wall temperatures. Finally, an approximate boundary condition representing the wall sheath effects on electrons has been utilized as discussed in Ref. 2. Since the VSL flowfield method uses shock fitting, shock slip boundary conditions have been used for all cases in order to properly conserve total energy.

To investigate the thermal, diffusion, and radiation models, two entry condition have been considered. The first, sometimes referred to as "AFE CFD Point 4", corresponds to a "max Q" point for an AFE vehicle at which the freestream conditions are 9.326 km/sec, 26.4 dynes/cm^2, and 200°K; while the second point is for the same vehicle but at 14 km/sec and 80 km altitiude. The latter is typical of a Mars return vehicle at an altitude where nonequilibrium phenomena could be significant. All of the 14 km/sec cases considered were calculated with radiative-gasdynamic coupling included. Since the AFE cases do not have significant radiative coupling, the radiation calculations have been made from the converged solutions. All radiation calculations have been made with LTNE effects accounted for using the molecular model and either the first or second order atomic models described previously.

Thermal Nonequilibrium Model

All the results presented in this section were calculated using the constant Lewis number (1.4) diffusional model from Miner and Lewis[18] and the chemical reaction set of Table 1 while radiative LTNE effects were calculated using the first order model. As a result, the results in this section are comparable to the results presented in Ref. 2 with the important distinction that the two temperature model used previously assumed $T_v = T_{tr}$ while the cases labeled as two termperature in this paper assume $T_v = T_e$.

The first results presented in Figs. 2 and 3 were obtained using a two temperature model wherein the electron/electronic and vibrational energies are assumed to be highly coupled and in equilibrium with each other[10]. This effect was acheived computationally by summing the two equations term by term and solving together. An alternate and, atleast theoretically, identical approach could have been achieved by solving the orignal equation set while forcing the electron-vibrational relaxation times, τ_e, to approach zero.

Fig. 2 shows that the AFE CFD 4 case is in chemical and thermal nonequilibrium for almost the entire shock layer and that the chemistry is dissociation dominated, the ionization level being very low. The thermal nonequilibrium is particularly interesting in the region of the wall where $T_v - T_e$ exceed the heavy particle translational temperature. In the wall region, both the ionic and atomic recombinations are dumping energy into the electron and vibrational energies respectively. It is assumed[1] that ionic recombinations occur primarily by the reverse of the electron-impact ionization reaction and that each recombination adds I to the electron translational energy while

the CVDV model[6,7] assumes that each atomic recombination adds $G_s - e_{v,s} \simeq D_s/2 - e_{v,s}$ to the vibrational energy of species s. Since $T_v - T_e$ exceeds T_{tr} in the wall thermal layer it follows that either or both of the recombination reactions is adding energy faster that the translational-vibrational and translational-electron exchange processes can remove it. The maximum value reached by the $T_v - T_e$ temperature was 8515°K at y/yshock=0.83.

Unlike the AFE CFD 4 case, the 14 km/sec case shown in Fig 3. shows a pronounced peak in the $T_v - T_e$ profile of about 17000°K at .83. Both thermal and chemical equilibrium occur for this case at abount .70 although, due to radiative cooling, the temperature continues to drop after this point along with gradual changes in the chemical composition. While the AFE CFD 4 point was dominated by dissociation, at this speed dissociation occurs very rapidly behind the shock front and ionization processes dominate most of the flow, reaching a peak degree of ionization of about 35%.

Results with the full three temperature model without electron-vibrational coupling are shown in Fig. 4 and 5. These cases represent the other extreme relative to the two temperature cases since there is no direct energy exchange mechanism between the electrons and the vibrational states. Indirectly some energy exchange still occurs through the coupling of both T_e and T_v to T_{tr}.

Comparing the three temperature results of Fig. 4 with the two temperature results of Fig. 2 it is seen that except for a greatly different T_e profile, the profiles are very similar. The vibrational temperature does peak a little sooner and higher at the shock front for the three temperature model, 9100°K at 0.91, but has the same profile over the rest of the shock layer, including the overshoot in the thermal boundary layer. Without T_e coupling, this high T_v indicates that energy production due to atomic recombinations is significant in the wall region as has been seen by other investigators[14]. As a result of electron energy depletion through electron impact ionization, the electron temperature is much lower behind the shock front for this model than before, which results in a much lower radiative heat flux. Also the lower electron temperature and its effect on the electron impact ionization rate increases the amount of chemical nonequilibrium at the shock front and in turn slightly increases the shock standoff distance.

As can be seen from the T_e profile, a shock slip condition was not enforced for the electron/electronic equation. Numerical problems with the slip boundary condition, coupled with the small magnitude of electron number density have not yet been resolved. This omission, however, does not have a significant effect on the other flow properties since the electron heat conduction is very small at the shock and also does not have a strong effect on the T_e profile itself. The electron temperature solution appears to be uncoupled from the shock boundary condition. This result is consistent with the quasi-equilibrium electron formulation previously used by the authors[1,2] in which it was assumed that chemical energy production and collisional energy transfer dominate the other terms in the electron energy equation and that T_e is primarly determined by the balance of the two.

The 14 km/sec case shown in Fig. 5, when compared with Fig. 3, shows the exact opposite trends as were noticed for the AFE CFD 4 case. The T_e profile is very similar in shape to the $T_v - T_e$ profile while T_v is greatly different. The vibrational temperature peaks much higher, 23000°K at 0.86, and equilibrates sooner with T_{tr}, due to high translational coupling. T_e peaks only slightly lower at 16900°K and 0.82 and as a result there is a slightly lower radiative flux.

In the thermal layer, the three temperature T_v initially dips below T_{tr} before rising above near the wall as in the two temperature case. Without electron coupling, diffusive effects in the thermal layer are important in the vibrational energy equation, and the flux of cool N_2 particles away from the wall lowers the vibrational energy until the atomic recombination reactions occur rapidly enough to raise T_v. This diffusive cooling effect was not seen in the AFE CFD 4 case due to the lower concentration gradients in N_2 and thus lower diffusive flux. The electron temperature in the thermal layer shows the same trends as were noted for the two temperature case.

Fig. 6 and 7 show results for the AFE CFD 4 and 14 km/sec cases, respectively, where the three temperature model is used with electron-vibrational coupling, as described previously in the theory section. As might be expected these results are in between the two extreme cases of the two temperature model and the three temperature model without $T_v - T_e$ coupling. In the AFE CFD 4 case the electron temperature has been increased toward T_v in the shock front, equilibrates with it around 0.70 and stays in equilibrium throught the rest of the shock layer except for a slight divergence immediately off the wall. The higher T_e profile results in a factor of two larger radiative flux than the uncoupled $T_v - T_e$ case, but it is still lower that the two temperature case.

For the 14 km/sec case, $T_v - T_e$ coupling lowers the vibrational temperature in the shock front region (from a peak value of 23000°K to 22200°K) while slightly raising the T_e profile and reduces the amount of diffusional cooling of T_v in the wall thermal layer. Percentage wise, the two temperature assumption has a slightly greater effect on the radiative flux for the lower speed case than the higher, 30% compared to 20%. The percentage differences would be further apart for the two cases if it were not for the fact that LTNE corrections tend to reduce the amount of radiation from the thermal nonequilibrium regions.

Diffusion Model

The results presented in this section were calculated using the chemical reaction set of Table 1 and first order LTNE radiative corrections, but for these cases the full diffusional model described above has been used. Figs. 8 and 9 show the results for the AFE CFD 4 case and 14 km/sec case, respectively. These cases were calculated using the three temperature, $T_v - T_e$ coupled thermal model and can be compared with the results in Figs. 6 and 7 to see the effect of various diffusional models.

Surprisingly, the profile changes associated with the different diffusional models are very small with the effect on the 14 km/sec case being slightly more noticable than for the AFE CFD 4 case. The results may be explained by the fact that for the AFE CFD 4 case, the flow is dominated by the species N_2 and N and thus a binary diffusion model with Le=1.4 is probably sufficient to describe most of the flow details. At 14 km/sec and in

the CVDV model[6,7] assumes that each atomic recombination adds $G_s - e_{v,s} \simeq D_s/2 - e_{v,s}$ to the vibrational energy of species s. Since $T_v - T_e$ exceeds T_{tr} in the wall thermal layer it follows that either or both of the recombination reactions is adding energy faster that the translational-vibrational and translational-electron exchange processes can remove it. The maximum value reached by the $T_v - T_e$ temperature was 8515°K at y/yshock=0.83.

Unlike the AFE CFD 4 case, the 14 km/sec case shown in Fig 3. shows a pronounced peak in the $T_v - T_e$ profile of about 17000°K at .83. Both thermal and chemical equilibrium occur for this case at abount .70 although, due to radiative cooling, the temperature continues to drop after this point along with gradual changes in the chemical composition. While the AFE CFD 4 point was dominated by dissociation, at this speed dissociation occurs very rapidly behind the shock front and ionization processes dominate most of the flow, reaching a peak degree of ionization of about 35%.

Results with the full three temperature model without electron-vibrational coupling are shown in Fig. 4 and 5. These cases represent the other extreme relative to the two temperature cases since there is no direct energy exchange mechanism between the electrons and the vibrational states. Indirectly some energy exchange still occurs through the coupling of both T_e and T_v to T_{tr}.

Comparing the three temperature results of Fig. 4 with the two temperature results of Fig. 2 it is seen that except for a greatly different T_e profile, the profiles are very similar. The vibrational temperature does peak a little sooner and higher at the shock front for the three temperature model, 9100°K at 0.91, but has the same profile over the rest of the shock layer, including the overshoot in the thermal boundary layer. Without T_e coupling, this high T_v indicates that energy production due to atomic recombinations is significant in the wall region as has been seen by other investigators[14]. As a result of electron energy depletion through electron impact ionization, the electron temperature is much lower behind the shock front for this model than before, which results in a much lower radiative heat flux. Also the lower electron temperature and its effect on the electron impact ionization rate increases the amount of chemical nonequilibrium at the shock front and in turn slightly increases the shock standoff distance.

As can be seen from the T_e profile, a shock slip condition was not enforced for the electron/electronic equation. Numerical problems with the slip boundary condition, coupled with the small magnitude of electron number density have not yet been resolved. This omission, however, does not have a significant effect on the other flow properties since the electron heat conduction is very small at the shock and also does not have a strong effect on the T_e profile itself. The electron temperature solution appears to be uncoupled from the shock boundary condition. This result is consistent with the quasi-equilibrium electron formulation previously used by the authors[1,2] in which it was assumed that chemical energy production and collisional energy transfer dominate the other terms in the electron energy equation and that T_e is primarly determined by the balance of the two.

The 14 km/sec case shown in Fig. 5, when compared with Fig. 3, shows the exact opposite trends as were noticed for the AFE CFD 4 case. The T_e profile is very similar in shape to the $T_v - T_e$ profile while T_v is greatly different. The vibrational temperature peaks much higher, 23000°K at 0.86, and equilibrates sooner with T_{tr}, due to high translational coupling. T_e peaks only slightly lower at 16900°K and 0.82 and as a result there is a slightly lower radiative flux.

In the thermal layer, the three temperature T_v initially dips below T_{tr} before rising above near the wall as in the two temperature case. Without electron coupling, diffusive effects in the thermal layer are important in the vibrational energy equation, and the flux of cool N_2 particles away from the wall lowers the vibrational energy until the atomic recombination reactions occur rapidly enough to raise T_v. This diffusive cooling effect was not seen in the AFE CFD 4 case due to the lower concentration gradients in N_2 and thus lower diffusive flux. The electron temperature in the thermal layer shows the same trends as were noted for the two temperature case.

Fig. 6 and 7 show results for the AFE CFD 4 and 14 km/sec cases, respectively, where the three temperature model is used with electron-vibrational coupling, as described previously in the theory section. As might be expected these results are in between the two extreme cases of the two temperature model and the three temperature model without $T_v - T_e$ coupling. In the AFE CFD 4 case the electron temperature has been increased toward T_v in the shock front, equilibrates with it around 0.70 and stays in equilibrium throught the rest of the shock layer except for a slight divergence immediately off the wall. The higher T_e profile results in a factor of two larger radiative flux than the uncoupled $T_v - T_e$ case, but it is still lower that the two temperature case.

For the 14 km/sec case, $T_v - T_e$ coupling lowers the vibrational temperature in the shock front region (from a peak value of 23000°K to 22200°K) while slightly raising the T_e profile and reduces the amount of diffusional cooling of T_v in the wall thermal layer. Percentage wise, the two temperature assumption has a slightly greater effect on the radiative flux for the lower speed case than the higher, 30% compared to 20%. The percentage differences would be further apart for the two cases if it were not for the fact that LTNE corrections tend to reduce the amount of radiation from the thermal nonequilibrium regions.

Diffusion Model

The results presented in this section were calculated using the chemical reaction set of Table 1 and first order LTNE radiative corrections, but for these cases the full diffusional model described above has been used. Figs. 8 and 9 show the results for the AFE CFD 4 case and 14 km/sec case, respectively. These cases were calculated using the three temperature, $T_v - T_e$ coupled thermal model and can be compared with the results in Figs. 6 and 7 to see the effect of various diffusional models.

Surprisingly, the profile changes associated with the different diffusional models are very small with the effect on the 14 km/sec case being slightly more noticable than for the AFE CFD 4 case. The results may be explained by the fact that for the AFE CFD 4 case, the flow is dominated by the species N_2 and N and thus a binary diffusion model with Le=1.4 is probably sufficient to describe most of the flow details. At 14 km/sec and in

the shock front region, the flow goes from being N_2-N dominated to N-N^+ dominated; but the collisional cross sections of N_2 and N^+ with respect to N differ by about an order of magnitude. Thus a single Lewis number in this region is not sufficient, although using a lower Lewis number to reflect the reduced diffusional effects in N-N^+ flow may have better represented the majority of the flow region. The above conclusions might not be applicable in an air mixture shock layer, however, since the additional species will generally result in regions where the flow is essentially not binary in nature.

Also, in flows where multiple ionic species coexist at the same concentrations, the new treatment of the ambipolar diffusional effects may be an important factor in the ionic species equations. A close evaluation of the species concentration profiles in Fig. 8 shows some unusual behavior at the shock front where the N^+ and N^+_2 profiles cross. However, these results need further study before firm conclusions can be stated.

Second Order Atomic LTNE Model

The results in this final section are cases which used the full diffusional model, the chemical reaction rates of Table 2, and the second order atomic LTNE model discussed in the theory section of this paper. The AFE CFD 4 results shown in Fig. 10 are very close to the previous results shown in Fig. 8. The only significant difference is in the N^+ and $N_2{}^+$ profiles at the shock front. The new rate for exitation of N is faster that the rate in Table 1 which leads to a faster total ionization rate even though the ionization from the excited states is not infinite. As a result of this faster ionization rate, there is a higher concentration of N^+ near the shock; and as a result of the charge exchange reaction and ambipolar diffusion effects, the higher N^+ concentration in turn slightly lowers the N^+_2 concentration. The calculated N^* population is very low and closely follows the T_e profile in detail as can partially be seen from the figure.

This case can also be compared to the similar case results presented in Ref. 2. The total radiation calculated in Ref. 2 is lower than the current results, due primarily to a lower T_e temperature calculated by the quasi-equilibrium electron/electronic energy equation used in Ref. 2. The radiative spectral differences between the previous case and this present case, however, should be due to the differences in the first and second order LTNE correction methods. The radiative spectral details of the radiation reaching the wall for the AFE CFD 4 case are shown in Fig. 11 in two forms; the first shows the atomic line radiation having been grouped into convenient blocks while the second shows the atomic lines in full detail. Having the lines grouped gives a better visual description of the magnitude of the relative radiative process whereas the detailed presentation bears more similarity to experimental results.

While the radiation shown in Fig. 11 is still dominated by the $N_2{}^+$(1-) molecular band in the 2-4 eV range, these new results show a much larger contribution from atomic lines in both the infrared (IR) and ultra-violet (UV) regions, especially in the IR region. In fact, the first order LTNE results from Ref. 1 showed almost no atomic radiation at all due to the large region of LTNE predicted for this case. The second order LTNE model predicts less LTNE for line radiation since the excited atomic electronic energy states are not as depleted as before.

The 14 km/sec case shown in Fig. 12 exhibits significant differences from the results in Fig. 9. The higher nitrogen excitation rate in Table 2 has shortened the nonequilibrium region at the shock front and lowered the peak T_e from 16650°K to 14560°K. Since this case is dominated by ionization chemistry, it would be expected that the results are sensitive to the ionization/excitation rates. The group and detailed wall radiation spectral plots are given as Fig. 13. Atomic radiation dominates for this case and most of it comes from the continuum UV bands. Strongly emitting IR lines are still seen and the high UV lines, above 11 eV, are highly absorbed at the lines centers.

Rather than compare these results to the earlier results which are greatly different in the chemical and thermal profiles, it was decided to redo the results of Fig. 9 using the higher excitation rate for N in place of the electron impact rate in Table 1. In this manner, first order LTNE results could be obtained with a chemical model very similar to that for the second order LTNE method. The flowfield profiles for this case are shown in Fig. 14. As expected, these profiles are very similar to those of Fig. 12 except that the peak T_e is lower, 13860°K, and equilibrium occurs slightly sooner. The earlier equilibration is to be expected since the first order LTNE assumes instantaneous equilibration of the excited states with the ions and electrons while the second order has a finite rate.

The radiative spectral plots for this case are shown in Fig. 15. In comparing these result to those in Fig. 13, three important differences are noticed. First, the IR line radiation is enhanced in the second order model over the first order model. This greater amount of emission is due to the lower level of thermodynamic nonequilibrium predicted from the second order method. The first order method predicts a largely depleted excited state population in the peak T_e region which reduces the line radiation from this region. Also, because of the reduced line radiation, absorption of the UV lines in the wall boundary layer is more significant for the first order LTNE model than for the second order model. The difference in UV line center absorption is the second noticable difference between Figs. 15 and 13. Finally, the N^+_2 (1-) molecular band is larger for the second order LTNE model. This difference appears to be due to a number of subtle changes in the two flowfilds such as different radiative cooling effects and different N^+_2 number densities caused by the charge exchange chemical reaction.

Conclusions

The use of a three temperature model including electron-vibrational coupling can lead to significant differences in the thermal profiles from those obtained with a two temperature model. The effects on chemistry are not as noticable due to the fact that the combined $T_v - T_e$ model tends to predict a temperature closest to the dominant energy for the flow conditions, i.e. closer to T_v in dissociation dominated flows and closer to T_e in ionization dominated flows. The differences in the thermal profiles for the two models results in differences of 20% to 30% in the radiative heat flux to the wall for the cases considered. These radiative differences would be more significant except that

LTNE effects tend to inhibit emission from the regions of thermal nonequilibrium.

A higher order diffusion model was developed and compared to a simple constant Lewis number multi-component diffusional model. The use of more exact diffusional models, while desirable for completeness of a solution method, was not seen to have a significant effect on results with a nitrogen gas, which tends to exhibit binary diffusive effects. Differing diffusion models may result in more noticable flowfield differences in more complex gas mixtures due to higher order diffusional effects.

The second order LTNE model developed for this paper has shown difficiencies in the first order LTNE model. While both models predict similar total heat fluxes, the spectral content of the radiation is different. Radiation reaching the wall with the second order LTNE model shows a greater IR line contribution and less UV line center absorption. The electron impact excitation calculated for the second order LTNE model is faster by an order of magnitude than the previous current rate. Using this faster rate with the first order model can closely reproduce much of the chemical behavior of the second order model.

Acknowledgement

This work was primarily supported by NASA Grant NAG-1-1003 from the Langley Research Center, with Dr. Lin C. Hartung as technical monitor. Mr. Gally is partially supported by a NASA Graduate Student Researchers Fellowship through the NASA Johnson Space Center.

REFERENCES

[1] Carlson, L. A. and Gally, T. A., "The Effect of Electron Temperature and Impact Ionization on Martian Return AOTV Flowfields," AIAA Paper 89-1729, June 1989.

[2] Carlson, L. A. and Gally, T. A., "Nonequilibrium Chemical and Radiation Coupling Phenomena in AOTV Flowfields," AIAA Paper 91-0569, January 1991.

[3] Thompson, R. A., "Comparison of Nonequilibrium Viscous Shock Layer Solutions with Windward Surface Shuttle Heating Data," AIAA Paper 87-1473, June 1987.

[4] Nicolet, W. E., "User's Manual for the Generalized Radiation Transfer Code (RAD/EQUIL or RADICAL)," NASA CR 116353, October 1969.

[5] Park, C., ***Nonequilibrium Hypersonic Aerothermodynamics***, John Wiley & Sons, New York, 1990, pp. 166-167.

[6] Treanor, C. E. and Marrone, P. V., "Effect of DIssociation on the Rate of Vibration Relaxation," *Physics of Fluids*, vol. 5, No. 9, September 1962, pp. 1022-1026.

[7] Marrone, P. V., "Inviscid, Nonequilibirum Flow behind Bow and Normal Shock Waves, Part I. - General Analysis and Numerical Examples," Cornell Aeronautical Laboratory Report No. QM-1626-a-12(I), May 1963.

[8] Park, C., "Calculation of Nonequilibrium Radiation in the Flight Regimes of Aeroassisted Orbital Transfer Vehicles," in ***Thermal Design of Aeroassisted Orbital Transfer Vehicles***, Progress in Astronautics and Aeronautics, Vol. 96, Ed. H. F. Nelson, AIAA, 1985, pp. 395-418.

[9] Millikan, R. C. and White, D. R., "Systematics of Vibrational Relaxation," *Journal of Chemical Physics*, vol. 39, No. 12, December 1963, pp. 3209-3213.

[10] Park, C., "Assessment of Two Temperature Kinetic Model for Ionizing Air," AIAA Paper No. 87-1574, June 1987.

[11] Lee, J. H., "Electron-Impact Vibrational Excitation Rates in the Flowfield of Aeroassisted Orbital Transfer Vehicles," in ***Thermophysical Aspects of Re-entry Flows***, Progress in Astronautics and Aeronautics, Vol. 103, Eds. J. N. Moss and C. D. Scott, AIAA, 1986, pp. 197-224.

[12] Candler, G. and Park, C., "The Computation of Radiation from Nonequilibrium Hypersonic Flows," AIAA 88-2678, June 1988.

[13] Moss, J. N., "Reacting Viscous Shock Layer Solutions with Multicomponent Diffusion and Mass Injection," NASA TR-R-411, June 1974.

[14] Gnoffo, P. A., Gupta, R. N., and Shinn, J. L.,, "Conservation Equations and Physical Models for Hypersonic Air Flows in THermal and Chemical Nonequilibrium," NASA TP 2867, February 1987.

[15] Carlson, L. A., "Radiative Gasdynamic Coupling and Nonequilibrium Effects Behind Reflected Shock Waves," *AIAA Journal*, vol. 9, No. 5, May 1971, pp. 858-865.

[16] Fay, J. A. and Kemp, N. H., "Theory of Stagnation Point Heat Transfer in a Partially Ionized Diatonic Gas," *AIAA Journal*, vol. 1, No. 12, December 1963, pp. 2741-2751.

[17] Camac, M. and Kemp, N. H., "A Multi-temperature Boundary Layer," Avco Research Report 184, August 1964.

[18] Miner, E. W. and Lewis, C. H., "Hypersonic Ionizing Air Viscous Shock Layer Flows over Nonanalytic Blunt Bodies," NASA CR-2550, May 1975.

[19] Chapman, S. and Cowling, T. G., ***The Mathematical Theory of Non-Uniform Gases***, Cambridge, 1964,pp. 343-349.

[20] Carlson, L. A., Bobskill, G. J., and Greendyke, R. B., "Comparison of Vibration Dissociation and Radiative Transfer Models for AOTV/AFE Flowfields," *J. of Thermophysics and Heat Transfer*, vol. 4, No. 1, January 1990, pp. 16-26.

[21] Kunc, J. A. and Soon, W. H., "Collisional Radiative Nonequilibrium in Partially Ionized Atomic Nitrogen," *Physical Review A*, vol. 40, No. 10, November 15, 1989, pp. 5822 ff.

[22] Foley, W. H. and Clarke, J. H., "Shock Waves Structered by Nonequilibrium Ionizing and Thermal Phenomena," *Physics of Fluids*, vol. 16, No. 3, March 1973, pp. 1612-1620.

[23] Nelson, H. F., "Nonequilibrium Structure of Argon Shock Waves," *Physics of Fluids*, vol. 16, No. 12, December 1973, pp. 2132-2142.

[24] Chapin, C. E., "Nonquilibrium Radiation and Ionization in Shock Waves," AA&ES Report, June 1967, Purdue, Univ., Lafayette, Ind.

[25] Clarke, J. H. and Ferrari, C., "Gas Dynamics with Nonequilibrium Radiative and Collisional Ionization," *Physics of Fluids*, vol. 8, December 1965, pp. 2121-2139.

Reaction	A	B	E
$N_2+N = 2N + N$	4.085×10^{22}	-1.5	113100
$N_2+N_2 = 2N + N_2$	4.70×10^{17}	-0.5	113100
$N_2+e^- = 2N^+ + e^-$	3.00×10^{24}	-1.6	113100
$N_2+N^+ = N_2^+ + N$	1.00×10^{12}	0.5	12200
$N + N = N_2^+ + e^-$	1.40×10^{13}	0.0	67800
$N + e^- = N^+ + 2e^-$	4.16×10^{13}	0.5	120000
$N + N = N + N^+ + e^-$	2.34×10^{11}	0.5	120000
$N + N^+ = 2N^+ + e^-$	2.34×10^{11}	0.5	120000

Rates in the form $k_f = A\,T^B \exp(-E/T)$.
$T = T_e$ in electron impact reactions.

Table 1. Reaction System for First Order LTNE Model

Reaction	A	B	E
$N_2+N = 2N_g + N$	4.085×10^{22}	-1.5	113100
$N_2+N_2 = 2N_g + N_2$	4.70×10^{17}	-0.5	113100
$N_2+N^+ = 2N_g + N^+$	1.90×10^{17}	-0.5	113100
$N_2+e^- = 2N^+ + e^-$	3.00×10^{24}	-1.6	113100
$N_2+N^+ = N_2^+ + N_g$	1.00×10^{12}	0.5	12200
$N_g+N_g = N_2^+ + e^-$	1.40×10^{13}	0.0	67800
$N_g+N = N + N^+ + e^-$	2.34×10^{11}	0.5	120000
$N_g+N^+ = 2N^+ + e^-$	2.34×10^{11}	0.5	120000
$N_g+e^- = N^+ + 2e^-$	2.50×10^{16}	0.0	169000
$N_g+e^- = N^* + e^-$	5.56×10^{16}	0.0	121000
$N^*+e^- = N^+ + 2e^-$	4.11×10^{17}	0.0	48900

Rates in the form $k_f = A\,T^B \exp(-E/T)$.
$T = T_e$ in electron impact reactions.
$N = N_g + N^*$.

Table 2. Reaction System for Second Order LTNE Model

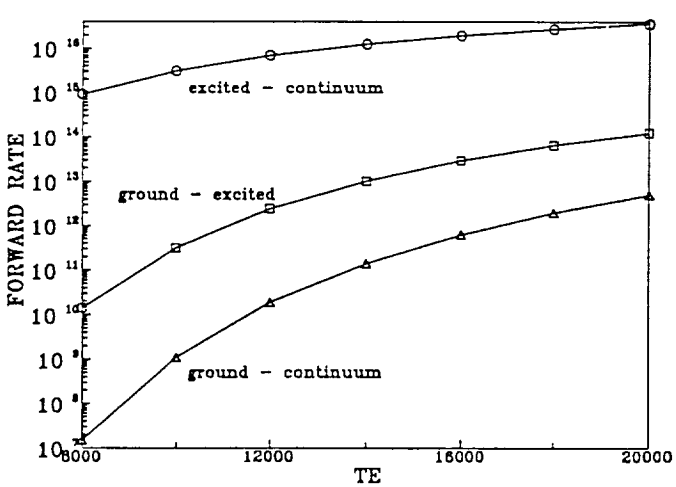

Fig. 1 Excitation and Ionization Rates for Nitrogen-Electron Collisions

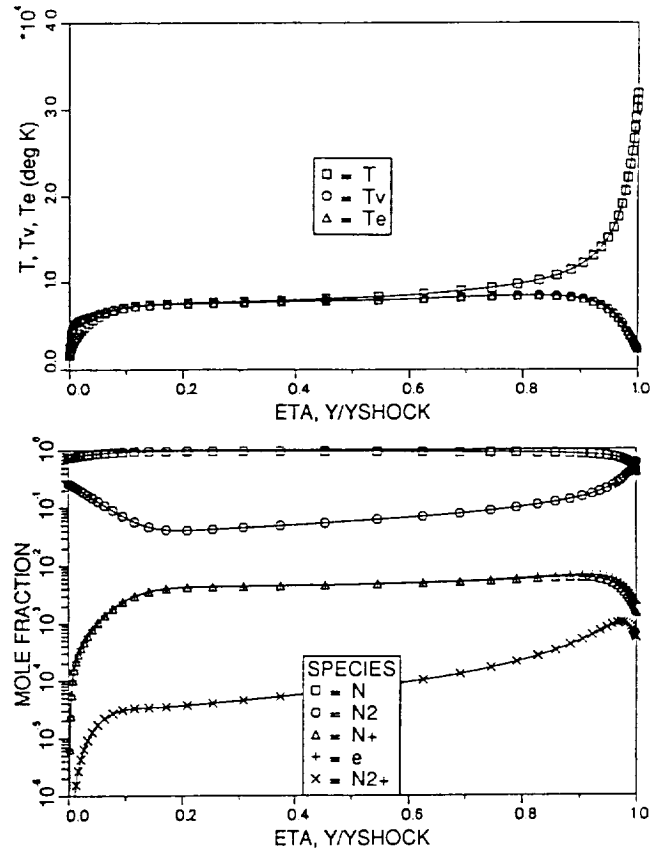

Fig. 2 Stagnation Profiles for AFE CFD Point 4 Two Temperature Model, QR=2.51 watts/cm², QC=27.6 watts/cm², YSHOCK=13.1 cm

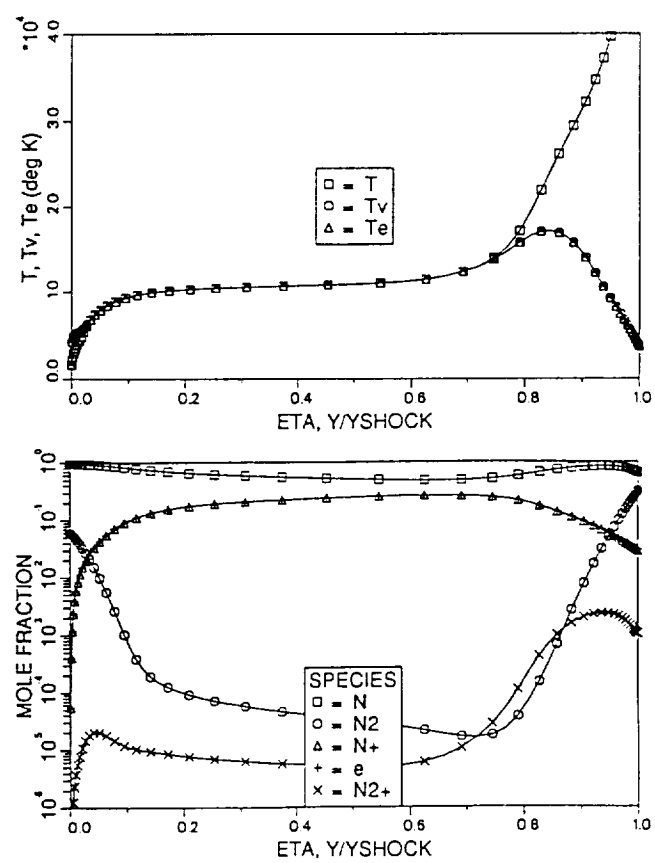

Fig. 3 Stagnation Profiles for 14 km/sec Case Two Temperature Model, QR=115.9 watts/cm², QC=66.2 watts/cm², YSHOCK=9.69 cm

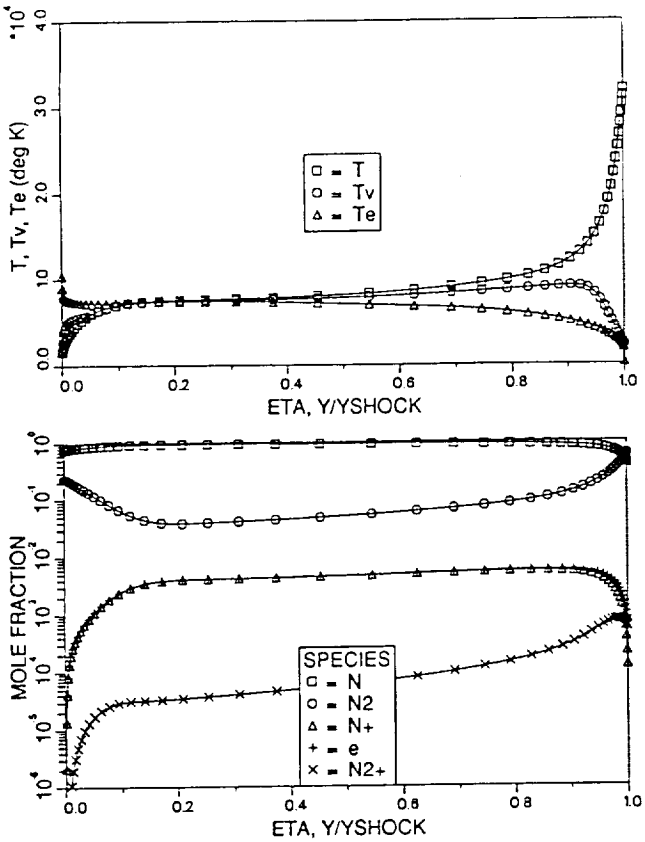

Fig. 4 Stagnation Profiles for AFE CFD Point 4
Three Temperature Model, without T_v-T_e Coupling
QR=1.02 watts/cm², QC=26.0 watts/cm²,
YSHOCK=13.1 cm

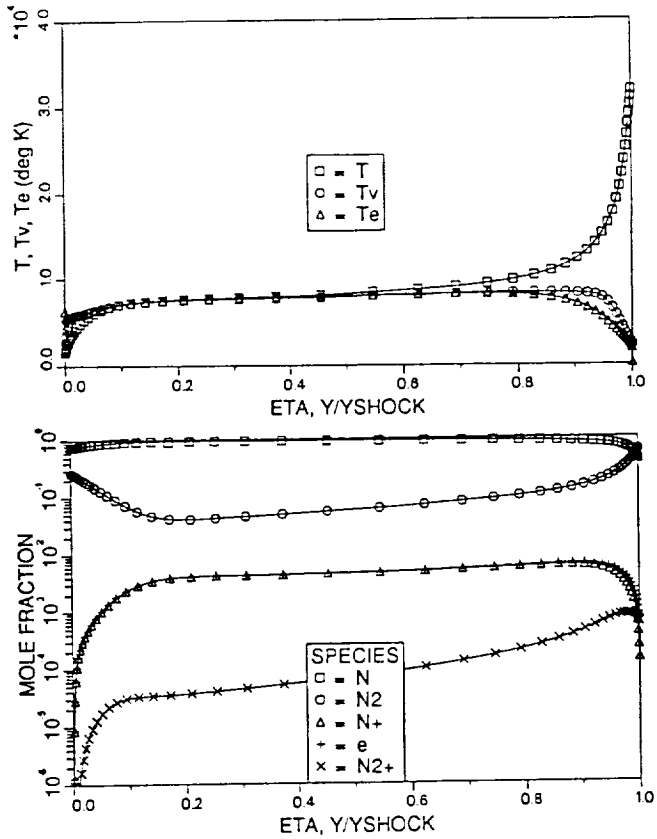

Fig. 6 Stagnation Profiles for AFE CFD Point 4
Three Temperature Model, with T_v-T_e Coupling
QR=1.93 watts/cm², QC=27.2 watts/cm²,
YSHOCK=13.1 cm

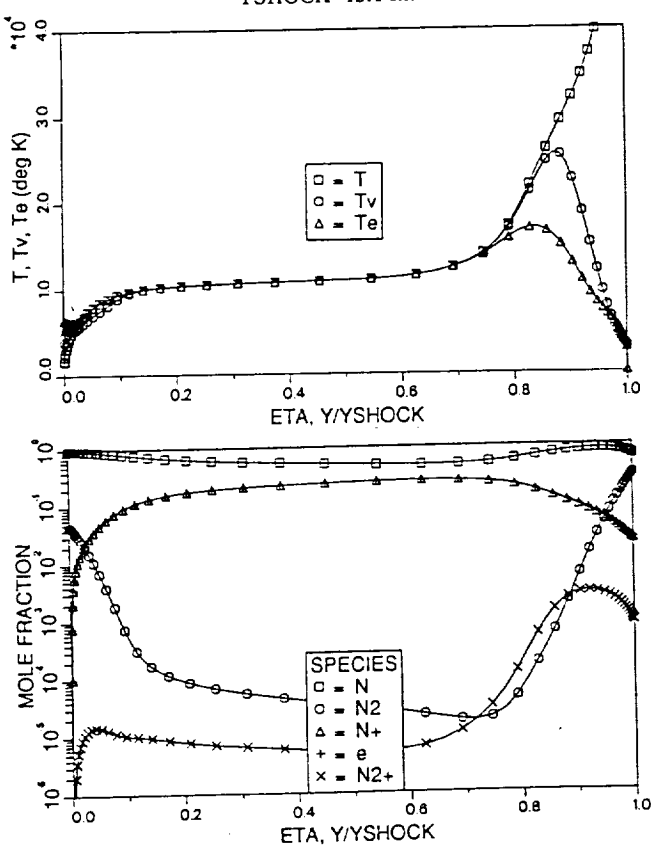

Fig. 5 Stagnation Profiles for 14 km/sec Case
Three Temperature Model, without T_v-T_e Coupling
QR=98.2 watts/cm², QC=61.2 watts/cm²,
YSHOCK=9.77 cm

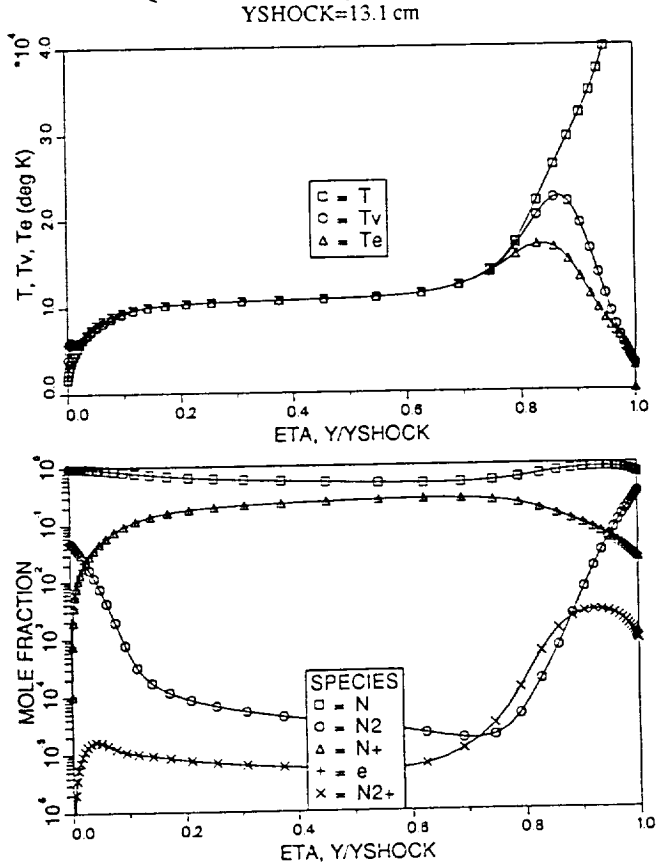

Fig. 7 Stagnation Profiles for 14 km/sec Case
Three Temperature Model, with T_v-T_e Coupling
QR=97.7 watts/cm², QC=59.9 watts/cm²,
YSHOCK=9.77 cm

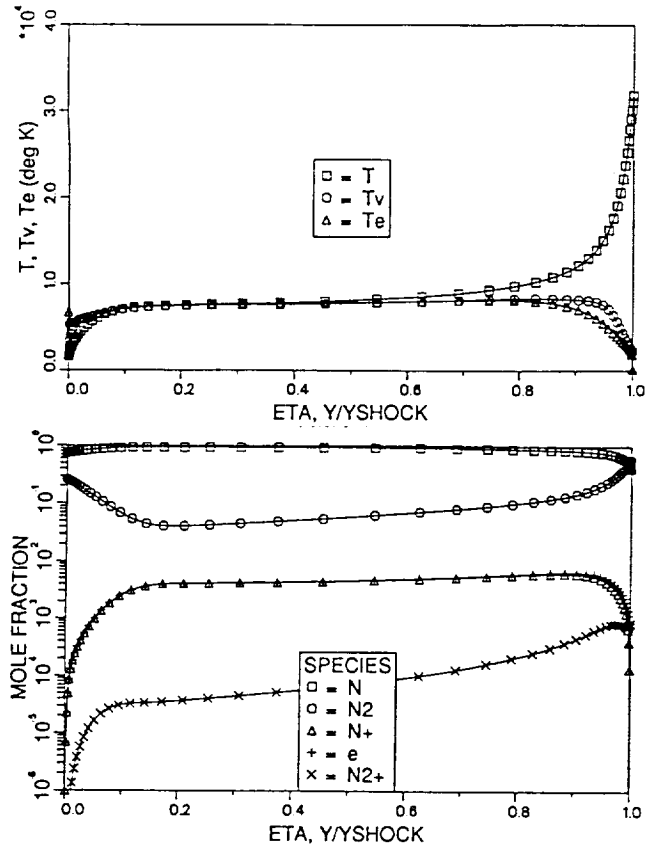

Fig. 8 Stagnation Profiles for AFE CFD Point 4
Full Multicomponent Diffusion Model, QR=1.95 watts/cm², QC=27.3 watts/cm², YSHOCK=13.1 cm

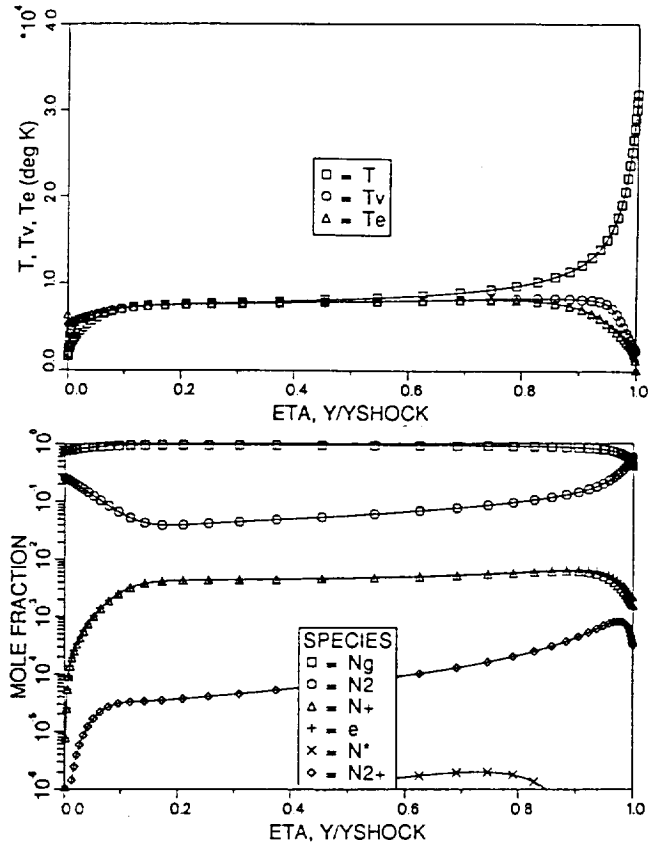

Fig. 10 Stagnation Profiles for AFE CFD Point 4
Second Order LTNE Model, QR=2.38 watts/cm², QC=27.8 watts/cm², YSHOCK=13.1 cm

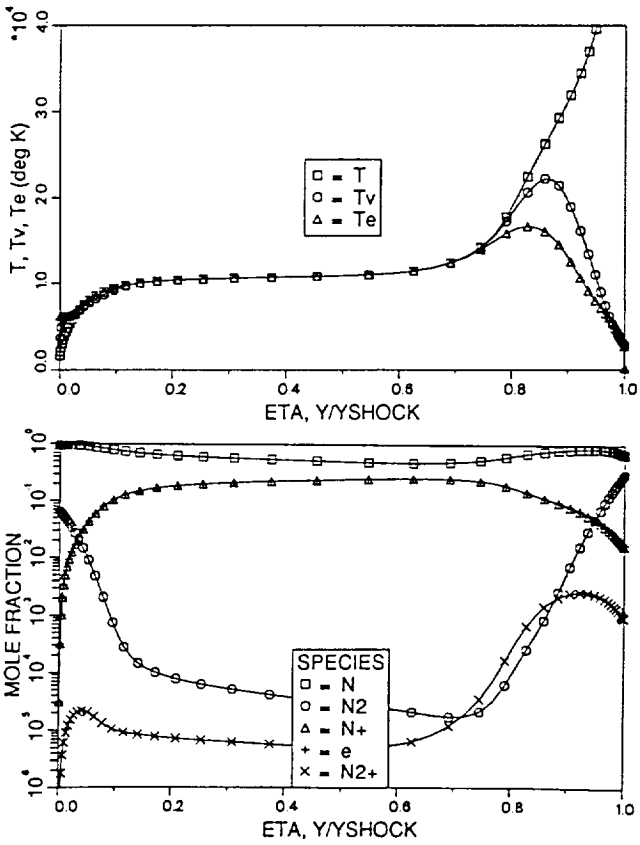

Fig. 9 Stagnation Profiles for 14 km/sec Case
Full Multicomponent Diffusion Model, QR=98.2 watts/cm², QC=53.8 watts/cm², YSHOCK=9.82 cm

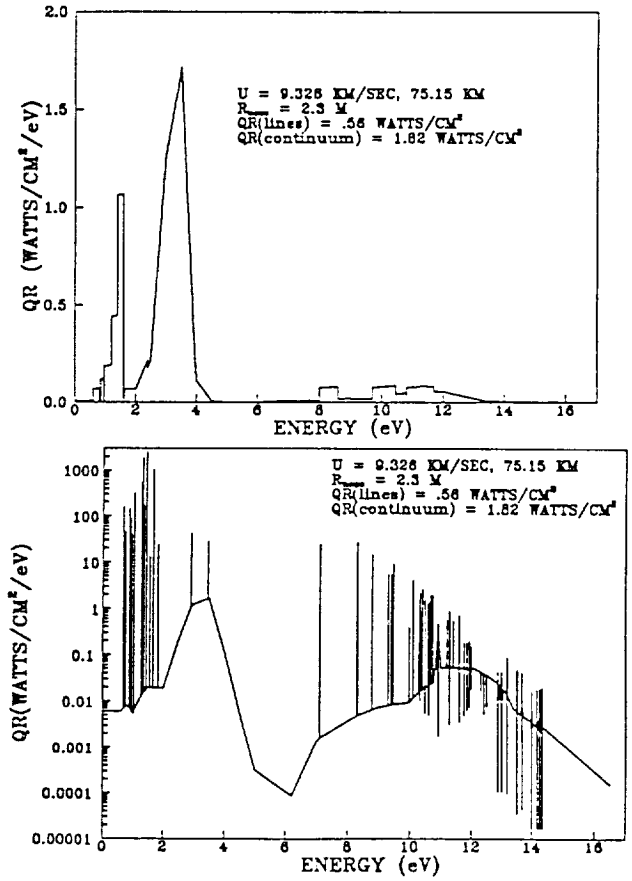

Fig. 11 Spectral Radiation Profiles for AFE CFD Point 4, Second Order LTNE Model

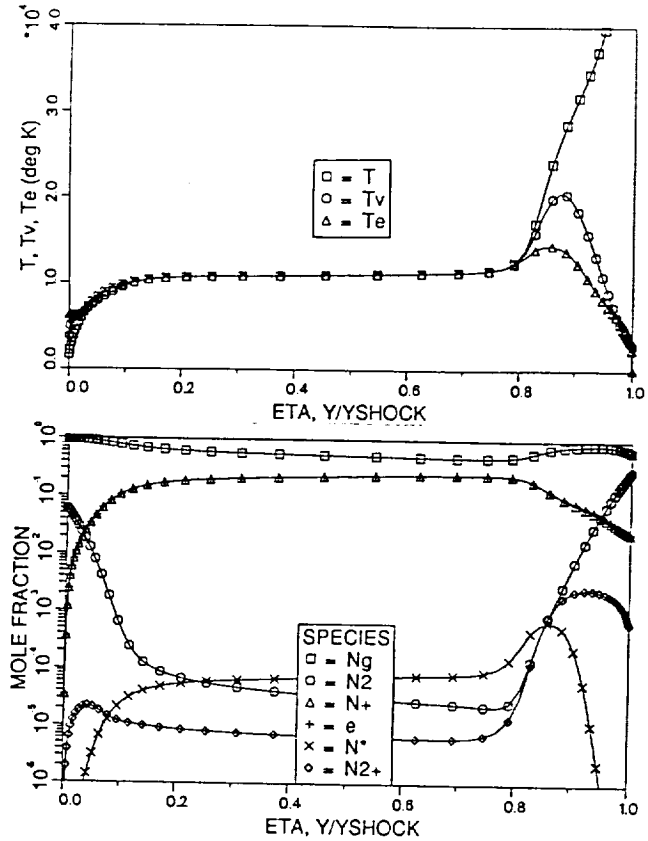

Fig. 12 Stagnation Profiles for 14 km/sec Case Second Order LTNE Model, QR=89.0 watts/cm², QC=55.1 watts/cm², YSHOCK=9.59 cm

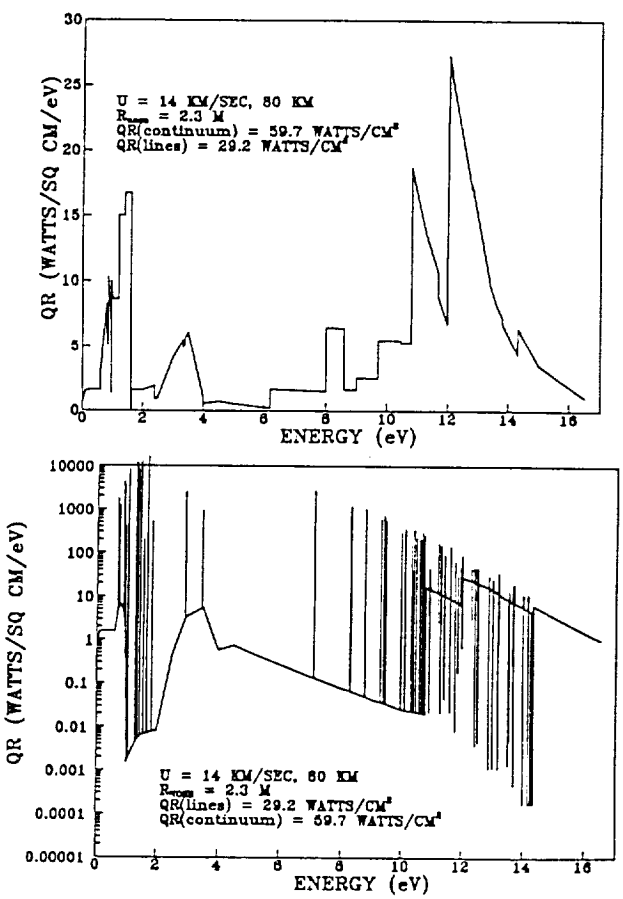

Fig. 13 Spectral Radiation Profiles for 14 km/sec Case, Second Order LTNE Model

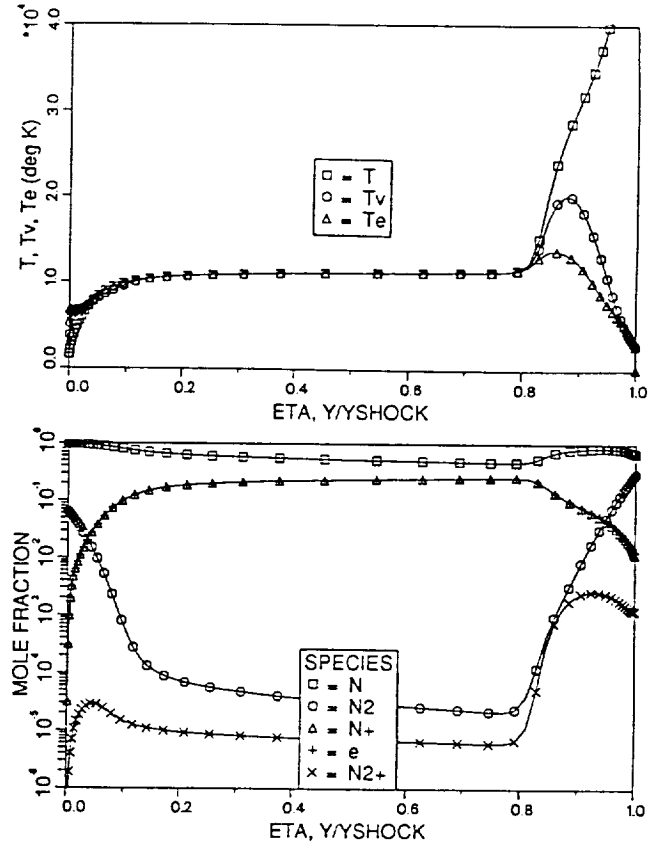

Fig. 14 Stagnation Profiles for 14 km/sec Case First Order LTNE Model with New Excitation Rate QR=82.2 watts/cm², QC=54.3 watts/cm², YSHOCK=9.58 cm

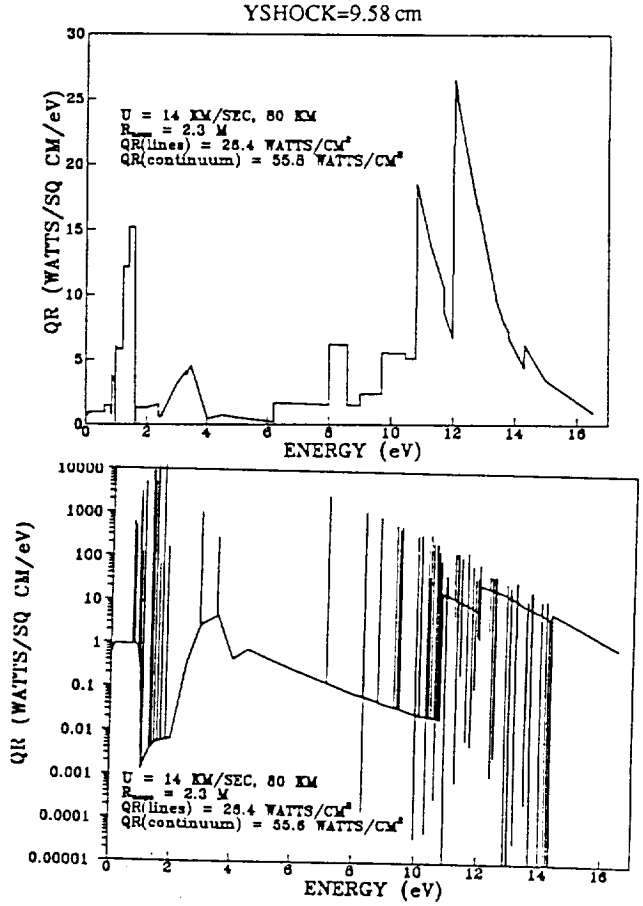

Fig. 15 Spectral Radiation Profiles for 14 km/sec Case First Order LTNE Model with New Excitation Rate

APPENDIX II

"A Comparative Study of Vibrational Relaxation Models for the Aeroassisted Orbital Transfer Vehicle Flight Regime"

Draft of M.Sc. Thesis

by

Derek S. Green

A COMPARATIVE STUDY OF VIBRATIONAL RELAXATION MODELS FOR THE AEROASSISTED ORBITAL TRANSFER VEHICLE FLIGHT REGIME

A Thesis

by

DEREK SCOTT GREEN

Submitted to the Office of Graduate Studies of
Texas A&M University
in partial fulfillment of the requirements forthe degree of

MASTER OF SCIENCE

May 1991

Major Subject: Aerospace Engineering

A COMPARATIVE STUDY OF VIBRATIONAL RELAXATION MODELS FOR THE AEROASSISTED ORBITAL TRANSFER VEHICLE FLIGHT REGIME

A Thesis

by

DEREK SCOTT GREEN

Approved as to style and content by:

Dr. Leland A. Carlson (Chairman of Committee)	Dr. Richard E. Thomas (Member)
Dr. Robert H. Page (Member)	Dr. Walter E. Haisler (Head of Department)

May 1991

ABSTRACT

A Comparative Study of Vibrational Relaxation Models for the Aeorassisted Orbital Transfer Vehicle Flight Regimes. (May 1991)

Derek Scott Green, B.S., Texas A&M University;

Chairman of Advisory Committee: Dr. Leland A. Carlson

The effects of various vibrational relaxation models at AOTV flight regimes in a pure nitrogen atmosphere have been analyzed. Three distinct vibrational relaxation models have been considered which include the well-known coupled vibration-dissociation-vibration (CVDV1) model, a modified CVDV1 model that better predicts relaxation times at high temperatures (CVDV2), and a modified CVDV2 model that accounts for the diffusive nature of vibrational relaxation (CVDV3). At a speed of 8.915 km/sec and an altitude of 77.9 km, the CVDV1 model predicted the fastest relaxation process, the CVDV2 model slowed the vibrational relaxation process near the shock, and the CVDV3 model slowed the vibrational relaxation process as temperatures approached equilibrium. At 9.326 km/sec and a higher freestream density at 75.2 km, the CVDV1 and CVDV2 models predict very similar vibrational temperature profiles due to the increased freestream density. At 12 km/sec and the high altitude density at 80 km the CVDV1 and CVDV2 models predicted trends similar to those at 8.915 km/sec; however, the modifications of the CVDV3 model had little effect on the vibrational relaxation process. At lower speeds, the vibrational-electron coupling term dominated the electron energy equation, driving the electron temperature to the vibrational temperature at all points in the flowfield.

ACKNOWLEDGEMENTS

I wish to first thank the members of my advisory committee for their participation and contribution of their valuable time. Much is owed to Dr. Carlson for his willingness to deal with my impatience and frustrations throughout this research. I feel fortunate to have been able to work with someone with such expertise and insight, and I will always value the experience. Special thanks goes to Tom Gally who was always helpful when problems arose relating to the VSL code or the computer system. His efforts have many times saved me from much wasted energy and anxiety.

TABLE OF CONTENTS

. . . . . Page

ABSTRACTCT iii

ACKNOWLEDGEMENTS iv

TABLE OF CONTENTS v

LIST OF TABLES vii

LIST OF FIGURES viii

NOMENCLATURE x

INTRODUCTION 1

VIBRATIONAL RELAXATION MODELS 5

Landau-Teller Model 5

Vibrational Relaxation Effects on Dissociation 8

Dissociation Effects on Vibrational Relaxation 9

Relaxation Time Correction 11

Diffusive Nature of Vibrational Relaxation 12

Simplification of Equations 13

VISCOUS SHOCK LAYER ASSUMPTIONS 16

Assumptions 16

Coordinate Transformation 17

Shock Boundary Condition 18

CONSERVATION EQUATIONS 19

METHOD OF SOLUTION 24

TABLE OF CONTENTS (CONTINUED)

. . . . . Page

Finite Difference Formulation 24

Linearization of Explicit Terms 25

RESULTS AND DISCUSSION 27

8.915 km/sec, 75.0 km 28

9.326 km/sec, 75.2 km 42

12.0 km/sec, 80 km 53

14 and 16 km/sec, 80 km 64

CONCLUSIONS 71

REFERENCES 73

APPENDIX I: TRANSPORT PROPERTIES 75

APPENDIX II: CHEMICAL KINETICS MODEL 76

VITA 77

LIST OF TABLES

. . . . . Page

Table 1: AOTV Trajectory Point Conditions 27

Table 2: Temperature Models Studied at 8.9, 9.3, and 12 km/sec 28

Table 3: Heat Transfer at Wall Boundary 69

Table 4: Chemical Reactions and Rate Coefficients 76

LIST OF FIGURES

. . . . . Page

Figure 1: Uncoupled QEE/T_v=T Model at U_∞=8.915 km/sec 30

Figure 2: Uncoupled QEEE/T_v=T Model at U_∞=8.915 km/sec 31

Figure 3: Coupled QEEE/CVDV1 Model at U_∞=8.915 km/sec 32

Figure 4: Coupled QEEE/CVDV2 Model at U_∞=8.915 km/sec 34

Figure 5: Coupled QEE/CVDV3 Model at U_∞=8.915 km/sec 36

Figure 6: Coupled QEEE/CVDV3 Model at U_∞=8.915 km/sec 37

Figure 7: Coupled QEEE/CVDV4 Model at U_∞=8.915 km/sec 39

Figure 8: Uncoupled QEEE/CVDV3 Model at U_∞=8.915 km/sec 40

Figure 9: Comparison of CVDV Models at U_∞=8.915 km/sec 42

Figure 10: Uncoupled QEE/T_v=T Model at U_∞=9.326 km/sec 43

Figure 11: Uncoupled QEEE/T_v=T Model at U_∞=9.326 km/sec 45

Figure 12: Coupled QEEE/CVDV1 Model at U_∞=9.326 km/sec 46

Figure 13: Coupled QEEE/CVDV2 Model at U_∞=9.326 km/sec 47

Figure 14: Coupled QEE/CVDV3 Model at U_∞=9.326 km/sec 48

Figure 15: Coupled QEEE/CVDV3 Model at U_∞=9.326 km/sec 49

Figure 16: Coupled QEEE/CVDV4 Model at U_∞=9.326 km/sec 50

Figure 17: Uncoupled QEEE/CVDV3 Model at U_∞=9.326 km/sec 51

Figure 18: Comparison of CVDV Models at U_∞=9.326 km/sec 52

LIST OF FIGURES (CONTINUED)

. . . . . Page

Figure 19: Uncoupled QEE/T_v=T Model at U_∞=12.0 km/sec 54

Figure 20: Uncoupled QEEE/T_v=T Model at U_∞=12.0 km/sec 55

Figure 21: Coupled QEEE/CVDV1 Model at U_∞=12.0 km/sec 56

Figure 22: Coupled QEEE/CVDV2 Model at U_∞=12.0 km/sec 57

Figure 23: Coupled QEE/CVDV3 Model at U_∞=12.0 km/sec 58

Figure 24: Coupled QEEE/CVDV3 Model at U_∞=12.0 km/sec 59

Figure 25: Coupled QEEE/CVDV4 Model at U_∞=12.0 km/sec 60

Figure 26: Uncoupled QEEE/CVDV3 Model at U_∞=12.0 km/sec 61

Figure 27: Comparison of CVDV Models at U_∞=12.0 km/sec 63

Figure 28: Uncoupled QEEE/T_v=T Model at U_∞=14.0 km/sec 65

Figure 29: Uncoupled QEEE/T_v=T Model at U_∞=16.0 km/sec . . . . . 66 ← Wrong

Figure 30: Coupled QEEE/CVDV3 Model at U_∞=14.0 km/sec 67

Figure 31: Coupled QEEE/CVDV3 Model at U_∞=16.0 km/sec 68

NOMENCLATURE

A - Coefficient to account for the diffusive nature of vibrational relaxation with heavy particles, defined by equation (20)

A_e - Coefficient to account for the diffusive nature of vibrational relaxation with electrons, defined by equation (22)

A_{sr} - Constant defined by equation (5) and used in equation (3)

c_s - Average molecular speed of species *s* given by equation (17)

$Cp_{v,s}$ - Vibrational component of specific heat for species *s*, defined by equation (25)

D_s - Diffusion coefficient of species *s*, defined by equation (48)

D_{sr} - Binary diffusion coefficient of species *s* with respect to species *r*, defined in defined by equation (47)

E_s - Average vibrational energy of dissociating species *s*

0_f - Denotes forward or dissociation rate

G_s - Average vibrational energy of recombining species *s*

h_e^{tr} - Enthalpy of free electrons per unit mass per unit volume

h_s^e - Electronic component of enthalpy for species *s*

h_1, h_3 - Shape factors for s,n,ϕ coordinate system, defined by equation (30)

h.p. - Heavy particles

k - Boltzmann constant

k_f - Forward reaction rate coefficient at vibrational nonequilibrium

NOMENCLATURE (CONTINUED)

$k_{f,equil.}$ - Forward reaction rate coefficient at vibrational equilibrium

m_s - Particle mass of species *s*

M_s - Molecular weight of species *s*

mol. - Molecules

N_s - Number of vibrational energy levels in harmonic oscillator, for species *s*

p - Heavy particle pressure

p_e - Electron pressure

Q_e - Rate of inelastic energy exchange for electrons

0_r - Denotes reverse or recombination rate

s,n,ϕ - Axisymetric body intrinsic coordinate system

t - Unit time

T - Average heavy particle translational temperature

T_e - Electron temperature

$T_{e,sh}$ - Electron temperature at the shock wave

$T_{m,s}$ - Temperature defined for convenience by equation (11) and used in equation (10)

T_{sh} - Heavy particle temperature at the shock wave

T_v - Average vibrational temperature

$T_{v,s}$ - Vibrational temperature of species *s*

NOMENCLATURE (CONTINUED)

$T_{v,sh}$ - Vibrational temperature at the shock

u,v,w - Velocity components in the s,n,ϕ coordinate system

u^j - Velocity components in Cartesian coordinate system

V_s - Vibrational coupling factor for dissociation of species *s*

w_s - Production rate of species *s*, mass per unit volume per unit time

x^j - Cartesian coordinate system

y_s - Moles per unit volume of species *s*

$\epsilon_{v,s}$ - Vibrational energy per unit mass of species *s* based on vibrational temperature

$\epsilon_{v,s}^{*}$ - Vibrational energy per unit mass of species *s* based on heavy particle temperature

$\epsilon_{v,s}^{**}$ - Vibrational energy per unit mass of species *s* based on electron temperature

η_v - Thermal conductivity coefficient for average vibrational energy, defined by equation (45)

$\eta_{v,s}$ - Thermal conductivity coefficient for vibrational energy of species *s*

$\theta_{v,s}$ - Characteristic vibrational energy of species *s*

θ_s - Body angle in the streamwise direction

θ_ϕ - Body angle between the radius vector and the line tangent to the body surface in the plane where ϕ=constant

κ_s,κ_ϕ - Body curvature in the streamwise and transverse direction

NOMENCLATURE (CONTINUED)

μ - Viscosity coefficient

μ_{sr} - Reduced molecular weight of colliding species used in equation (3)

ρ_s - Mass per unit volume of species s

ρ - Total mass per unit volume

σ_v - Limiting cross section used in equation (16) and defined by equation (18)

τ_e - Vibrational relaxation time for equilibration with electron translational energy

τ_s - Average vibrational relaxation time of species s for equilibration with heavy particle translational energy

τ_s^{MW} - Average vibrational relaxation time of species s for equilibration with heavy Particle translational energy given by Millikan and White in equations (3)-(6)

τ_{sr} - Vibrational relaxation time of species s for equilibration with heavy particle translational energy of species r

ζ_{es} - Rate of elastic electron energy exchange with species s

INTRODUCTION

Future space programs such as the space station, lunar missions, and Martian missions will require a vehicle to return large payloads from space to low earth orbits. This transfer will require retrobraking of the transport vehicle which can be accomplished with aerobraking in the upper earth atmosphere. The overall retrobraking process will begin with a descent to the upper earth atmosphere at high speed, aerobraking, and a return to an earth based orbit at reduced speed. Aerobraking reduces the vehicle velocity by utilizing aerodynamic drag on a heat shield that protects the transport vehicle.

During the high speed pass through the upper atmosphere of the earth, the transport vehicle will encounter a flowfield that is in thermal, chemical, and radiative nonequilibrium. Across the shock which forms over the heat shield of the transport vehicle at superorbital velocity and low atmospheric density, temperature gradients are extreme. However, since chemical and thermal equilibration proceed at a finite rate, areas of nonequilibrium exist in the post shock region. Thus, the equilibration processes must be modeled adequately to predict the flowfield about the transport vehicle.

An aeroassisted orbital transfer vehicle (AOTV) that utilizes aerobraking has been proposed to transport payloads between high orbits of the space station and lower orbits accessible to the Space Shuttle.[1] During aerobraking the AOTV would encounter

---

Format in accordance with the *AIAA Journal*

nonequilibrium as described earlier. The coupling of these phenomena affects the radiation in the flow, and the extent of radiative heating in the AOTV flowfield is of significant interest.[1,2]

The amount of radiative heating is dependent on the chemical composition and electron-electronic temperature at each point in the flowfield, and the chemical composition is governed by the reaction rates and the internal energy in the flow as well as the modes in which the energy is stored. While the internal energy can be partitioned into heavy-particle translational, rotational, vibrational, electron, and electronic energy modes, each mode should be characterized by a separate temperature. Thus, the rate and mechanisms by which the rotational, vibrational, electron, and electronic temperatures equilibrate with the heavy-particle temperature is very important and must be modeled appropriately.

For AOTV flowfield conditions, the static pressure in the shock layer is on the order of 0.01 atm.[1,3]. At this pressure rotational temperature equilibrates almost immediately behind the shock, and it can be considered equal to the heavy-particle temperature. However, electron temperature has a much different equilibration rate with the heavy particle temperature due to the significant difference in mass of heavy particles and electrons.[1] However, there is an efficient exchange of energy between the electron and electronic energy modes, and these two modes can be adequately describe with a single electron temperature. Also, vibrational temperature is slow to equilibrate with the heavy particle temperature and differs from electron temperature.

If radiative heating and the flowfield are to be accurately predicted, a suitable thermal nonequilibrium model must be incorporated so that both chemical composition

and internal energy are accurately predicted. Therefore, a three temperature model that includes heavy particle, electron, and vibrational temperatures should be used to describe an AOTV flowfield. The current work expands a pre-existing heavy particle and electron temperature model, which assumed that vibrational temperature equilibrated with heavy particle temperature immediately behind the shock wave, to a three temperature model that includes a separate vibrational temperature. Thus, the objectives of the current research are to determine at which flight conditions the assumption of vibrational equilibrium is valid, at which conditions vibrational nonequilibrium must be modeled, and the effect of vibrational nonequilibrium at these conditions.

Various nonequilibrium vibrational energy models that model the conservation of vibrational energy will be investigated, and a comparative study of the different models will be conducted. Landau and Teller originally developed an equation for vibrational equilibration, or relaxation, in an ambient gas, which accounts for the exchange of energy over time between the translational and vibrational modes. Later, however, Treanor and Marrone[4] modeled the effects of dissociation on the vibrational relaxation process based on the premise that dissociation occurs at the higher energy states more easily, thus lowering the mean vibrational energy. They also determined that dissociation is slower when there is vibrational nonequilibrium because there are fewer molecules in the more easily dissociated excited vibrational states. More recently, Park claimed that the relaxation time expression formulated by Millikan and White predicts an unrealistically small relaxation time at high temperatures.[5,6] Secondly, Park noted that the diffusive nature of vibrational relaxation at high

temperatures can be modeled by modifying the Landau-Teller equation.[5]

The effects of each of the vibration-dissociation models will be investigated at flight regimes which include vehicle velocities of 8.9-16 km/s at altitudes of 75-80 km in a nitrogen atmosphere that is easily modeled using only eight chemical reactions. The flow along the stagnation streamline will be studied and the significance of vibrational nonequilibrium will be determined so that accurate radiative and convective heating calculations can be made in the future. And thus, the objectives of the current research are to determine at which flight conditions the assumption of vibrational nonequilibrium is valid, at which conditions vibrational nonequilibrium must be modeled, and the effect of vibrational nonequilibrium at these conditions.

VIBRATIONAL RELAXATION MODELS

Landau-Teller Model

The vibrational relaxation process is governed by the conservation of vibrational energy. In a quiescent gas, an energy exchange will occur between the translational and vibrational modes, for which Landau and Teller[7] developed the expression

$$\frac{d\epsilon_{v,s}}{dt} = \frac{\epsilon^{*}_{v,s}(T) - \epsilon_{v,s}}{\tau_s} + \frac{\epsilon^{**}_{v,s}(T_e) - \epsilon_{v,s}}{\tau_e} \tag{1}$$

The subscript s in equation (1) distinguishes the molecular species, since an independent equation and corresponding vibrational temperature can be designated for each molecular species; and the rate of energy exchange between translational and vibrational modes is split into heavy particle and electron collisions on the right hand side of equation (1).

The distinction between heavy particle and electron collisions is required for two reasons. First, the rate of energy exchange between translational and vibrational modes is linearly proportional to the difference in equilibrium vibrational energy and actual vibrational energy. Since equilibrium vibrational energy is based on local translational temperature, and electron temperature may not be in equilibrium with heavy particle temperature, different equilibrium vibrational energies, $\epsilon_{v,s}^{*}(T)$ and $\epsilon_{v,s}^{**}(T_e)$, will exist for electron and heavy particle collisions. Using a simple harmonic oscillator model, local and equilibrium vibrational energy per unit mass can be expressed as

$$\epsilon_{v,s} = \frac{k}{m_s} \frac{\theta_{v,s}}{(e^{\theta_{v,s}/T_{v,s}} - 1)}$$

$$\epsilon^{*}_{v,s}(T) = \frac{k}{m_s} \frac{\theta_{v,s}}{(e^{\theta_{v,s}/T} - 1)} \tag{2}$$

$$\epsilon^{**}_{v,s}(T_e) = \frac{k}{m_s} \frac{\theta_{v,s}}{(e^{\theta_{v,s}/T_e} - 1)}$$

The second reason for discriminating between heavy particle and electron collisions is that relaxation times τ_s and τ_e are based on empirical equations which differ for heavy particles and electrons. Millikan and White[3,8] developed an empirical expression for the relaxation time τ_{sr} based on molecular species s with various collision partners r. The relaxation time is presented in the form $p\tau_{sr}$ (atm-s) as a function of translational temperature (° K) as

$$p\tau_{sr} = \exp[A_{sr}(T^{-1/3} - 0.015\mu_{sr}^{1/4}) - 18.42) \tag{3}$$

where μ_{sr} is the reduced molecular weight of the colliding species expressed as

$$\mu_{sr} = \frac{M_s M_r}{M_s + M_r} \tag{4}$$

and A_{sr} is a constant based on the reduced molecular weight and the characteristic vibrational temperature (° K) and A_{sr} has the form

$$A_{sr} = 1.16x10^{-3}\ \mu_{sr}^{1/2}\ \theta_{v,s}^{4/3} \tag{5}$$

Now, τ_s can be expressed as a weighted average of τ_{sr} based on the mole fraction of each collision partner as

$$\tau_s^{MW} = \frac{\sum_{r=h.p.} y_r}{\sum_{r=h.p.} y_s/\tau_{sr}} \tag{6}$$

The relaxation time τ_e for the electron-vibrational energy transfer was estimated by Lee[9], and Candler[10] curve fit his results using two quadratics in the logarithm (base 10) of electron temperature. The relaxation time is in the form of $p_e\tau_e$ (atm-s) and is expressed as

$$\log(p_e\tau_e) = \begin{cases} 7.50(\log T_e)^2 - 57.0\log T_e + 98.70, & T_e < 7000K \\ 2.36(\log T_e)^2 - 17.9\log T_e + 24.35, & T_e > 7000K \end{cases} \tag{7}$$

As noted, equation (1) was developed for a quiescent gas, but it can be adapted to model an inviscid flowing gas by including convective terms. Likewise, a viscous flowing gas can be modeled by adding convective, conductive, and diffusive terms to the quiescent gas equation developed by Landau and Teller.[1,11] Thus, one obtains the viscous vibrational energy conservation equation per unit volume as

$$\begin{aligned} \frac{\partial}{\partial t}(\rho_s \epsilon_{v,s}) + \frac{\partial}{\partial x^j}(\rho_s \epsilon_{v,s} u^j) &= \frac{\partial}{\partial x^j}\left(\eta_{v,s}\frac{\partial T_{v,s}}{\partial x^j}\right) \\ + \frac{\partial}{\partial x^j}\left(\rho \epsilon_{v,s} D_s \frac{\partial y_s}{\partial x^j}\right) &+ \rho_s \frac{\epsilon^*_{v,s} - \epsilon_{v,s}}{\tau_s} + \rho_s \frac{\epsilon^{**}_{v,s} - \epsilon_{v,s}}{\tau_e} \end{aligned} \tag{8}$$

The vibrational conductivity is a result of a vibrational energy gradient in the flow where there is a transport of energy due to a vibrational-vibrational transfer.[1] Also, vibrational diffusion is due to a concentration gradient and vibrational energy gradient in the flow. Since there will be a natural diffusion rate from greater concentration to lesser concentration, the diffusing molecules will also change the local average vibrational energy if there exists a vibrational energy gradient.

Vibrational Relaxation Effects on Dissociation Rates

Dissociation rates are dependent on the frequency of particle collisions with sufficient energy to break molecular bonds, and the energy required for dissociation is obtained from translational and vibrational energy modes. If vibrational temperature is less than heavy particle temperature, there will be fewer collisions with sufficient energy to effect dissociation as compared to the thermal equilibrium case. Since reaction rate curve fits to data assume thermal equilibrium, dissociation rates will be unrealistically fast because the data implies that each collision will have more energy than the actual thermal nonequilibrium relaxation process. To obtain a more realistic dissociation rate, Treanor and Marrone[12] introduced a vibrational coupling factor which should be multiplied by the forward dissociation rate. This vibrational coupling factor is defined as the ratio of the actual forward rate to the rate that would exist for local vibrational equilibrium and is expressed as

$$V_s = \frac{k_f}{k_{f_{equil.}}} \tag{9}$$

The actual expression for the coupling factor is derived assuming a harmonic oscillator and equal probability of dissociation at each vibrational level. By neglecting terms that are small for temperatures less than the characteristic dissociation temperature, the vibrational coupling factor is

$$V_s = \frac{1}{N_s} \frac{1 - e^{-\left(\frac{N_s \theta_{v,s}}{T_{v,s}}\right)}}{e^{\left(\frac{\theta_{v,s}}{T_{v,s}}\right)} - 1} \frac{e^{\left(\frac{\theta_{v,s}}{T_{v,s}}\right)} - 1}{e^{\left(\frac{\theta_{v,s}}{T}\right)} - 1} \tag{10}$$

where

$$\frac{1}{T_{m,s}} = \left(\frac{1}{T_{v,s}} - \frac{1}{T}\right) \tag{11}$$

and N_s is the number of vibrational levels for species s. While the coupling factor V_s should be multiplied by each forward rate that involves the dissociation of species s, the corresponding reverse rate should not be modified since the recombination process is not influenced by the vibrational temperature.

Dissociation Effects on Vibrational Relaxation

The conservation of vibrational energy as expressed by equation (8) does not account for the depletion of vibrational energy resulting from dissociation. In the AOTV flowfield, vibrational energy levels are assumed to be populated according to a Boltzmann distribution, that is characterized by a vibrational temperature. Dissociation, however, occurs more easily from the higher levels of the Boltzmann distribution, causing the average energy or temperature to be reduced. Treanor and Marrone[4] derived an expression to account for the effects of dissociation on vibrational relaxation as

$$\frac{d\epsilon_{v,s}}{dt} = \frac{\epsilon^*_{v,s} - \epsilon_{v,s}}{\tau_s} + \frac{(\epsilon_{v,s} - E_s)}{\rho_s}\left(\frac{d\rho_s}{dt}\right)_f - \frac{(\epsilon_{v,s} - G_s)}{\rho_s}\left(\frac{d\rho_s}{dt}\right)_r \tag{12}$$

The second term on the right side of the equation accounts for the energy lost due to dissociation, where $(d\rho_s/dt)_f$ equals the dissociation rate and E_s equals the average vibrational energy of the dissociating molecule. E_s can be expressed as[4]

$$E_s = \frac{k}{m_s}\frac{\theta_{v,s}}{e^{\theta_{v,s}/T_{m,s}} - 1} - \frac{k}{m_s}\frac{N_s\theta_{v,s}}{e^{N_s\theta_{v,s}/T_{m,s}} - 1} \tag{13}$$

The third term on the right side of equation (12) accounts for the energy gained due to recombination, where $(d\rho_s/dt)_r$ equals the recombination rate and G_s represents the average vibrational energy at which recombination occurs. G_s is equal to the limit of E_s as T_v approaches T, and can be expressed as

$$G_s = \frac{1}{2}\frac{k}{m_s}\theta_{v,s}(N-1) \tag{14}$$

The derivation of both G_s and E_s assumes a harmonic oscillator at a Boltzmann distribution.

When the effects of dissociation-vibration coupling are included in equation (8), the vibrational conservation equation for a viscous flow becomes

$$\begin{aligned}\frac{\partial}{\partial t}(\rho_s\epsilon_{v,s}) + \frac{\partial}{\partial x^j}(\rho_s\epsilon_{v,s}u^j) &= \frac{\partial}{\partial x^j}(\eta_{v,s}\frac{\partial T_{v,s}}{\partial x^j}) \\ + \frac{\partial}{\partial x^j}(\rho h_{v,s}D_s\frac{\partial y_s}{\partial x^j}) &+ \rho_s\frac{\epsilon^*_{v,s}-\epsilon_{v,s}}{\tau_s} + \rho_s\frac{\epsilon^{**}_{v,s}-\epsilon_{v,s}}{\tau_e} \\ &- E_s(\frac{d\rho_s}{dt})_f + G_s(\frac{d\rho_s}{dt})_r\end{aligned} \tag{15}$$

This equation, when included with the V_s coupling factor on the forward dissociation rates, is usually termed the Coupled Vibration-Dissociation-Vibration (CVDV) Model; the dissipative effects of dissociation on vibrational energy and the reduction of forward dissociation rates by a nonequilibrium vibrational temperature are characterized by this model. For clarity, this model will be denoted as CVDV1 in thesis since modifications to the model have been suggested by Park.

Relaxation Time Correction

The expression for τ_{sr} given by equation (3) is valid for temperatures up to about 8000° K.[1,11] Also, Park[5] claims that equation (3) effectively predicts unrealistically large cross sections for the vibrational relaxation process at higher temperatures (greater than 40,000° K), and he suggests[4,5] a modification to the Millikan and White expression

$$\tau_s = \tau_s^{MW} + \frac{1}{c_s \sigma_v y_s} \tag{16}$$

where the average molecular speed c_s is expressed as

$$c_s = \sqrt{\frac{8kT}{\pi m_s}} \tag{17}$$

Here, y_s and m_s represent the number density and particle mass of species s, and σ_v is the limiting cross section expressed as[13]

$$\sigma_v = 10^{-16} (50{,}000° K/T)^2 \quad cm^2 \tag{18}$$

Park[13] claims that the most appropriate limiting cross section for temperatures less than 19,000° K is 10^{-16} cm^2, and for a temperature range of up to 62,000° K the limiting cross section is best represented by equation (18) with the coefficient equal to 10^{-17}. Carlson[14], however, suggests that the limiting cross section might be better represented by equation (18) when the coefficient is equal to 10^{-16}. For this study, coefficient values of 10^{-16} and 10^{-17} in equation (18) will both be examined. Therefore, a second CVDV model (CVDV2) will include the Park modification to the relaxation time τ_s, equation (16), and will use a coefficient equal to 10^{-16} in the expression for the limiting cross section, equation (18). The effects of using a coefficient equal to 10^{-17} in the

expression for the limiting cross section will be studied in a CVDV model that will also include other modifications.

Diffusive Nature of Vibrational Relaxation

Another modification to the translational-vibrational coupling term introduced in equation (1) arises from the diffusive nature of vibrational relaxation at high temperatures. Park[6] states that the effect of the diffusive nature is to slow the rate of the vibrational relaxation process as compared to that predicted by Landau and Teller in equation (1). Park[13] suggests that the diffusive nature of the vibrational relaxation process can be modeled by modifying the Landau Teller term in equation (1) to

$$\frac{\partial \epsilon_v}{\partial t} = \frac{\epsilon_v^*(T) - \epsilon_v}{\tau} A + \frac{\epsilon_v^{**}(T_e) - \epsilon_v}{\tau_e} A_e \tag{19}$$

The coefficient A is a function of local vibrational temperature, vibrational temperature at the shock, and heavy particle temperature at the shock and has the form

$$A = \left| \frac{T_{sh} - T_v}{T_{sh} - T_{v,sh}} \right|^{(3.5e^{-5000^\circ K/T_s} - 1)} \tag{20}$$

The original relaxation rate presented by Landau and Teller varied linearly with the difference in equilibrium and local vibrational energies; however, the Park modification that accounts for the diffusive nature forces the relaxation rate to vary proportionally to the difference in energies raised to the sth power. From equation (20) s can be expressed as

$$s = 3.5e^{(-5000^\circ K/T_s)} \tag{21}$$

With similar logic, the coefficient A_e added to the vibrational-electron coupling term

can be expressed as

$$A_e = \left| \frac{T_{e_{sh}} - T_v}{T_{e_{sh}} - T_{v,sh}} \right|^{3.5-1} \tag{22}$$

These modifications define a third CVDV model (CVDV3) which includes the diffusive effects of vibrational relaxation and the correction of the relaxation time τ_s as shown in equation (16). Thus, CVDV3 differs from CVDV2 by only the A and A_e coefficients on the Landau-Teller terms.

The fourth CVDV model (CVDV4) includes both the modification for the diffusive effects of vibrational relaxation and the correction of the relaxation time τ_s, but the coefficient used in equation (18) is equal to 10^{-17} as opposed to the value 10^{-16} used in the CVDV2 and CVDV3 models. The general form for both the CVDV3 and CVDV4 vibrational relaxation models is

$$\begin{aligned} \frac{\partial}{\partial t}(\rho_s \epsilon_{v,s}) + \frac{\partial}{\partial x^j}(\rho_s \epsilon_{v,s} u^j) &= \frac{\partial}{\partial x^j}\left(\eta_{v,s} \frac{\partial T_{v,s}}{\partial x^j}\right) \\ + \frac{\partial}{\partial x^j}\left(\rho h_{v,s} D_s \frac{\partial y_s}{\partial x^j}\right) &+ \rho_s \frac{\epsilon^*_{v,s} - \epsilon_{v,s}}{\tau_s} A + \rho_s \frac{\epsilon^{**}_{v,s} - \epsilon_{v,s}}{\tau_e} A_e \\ &- E_s\left(\frac{d\rho_s}{dt}\right)_f + G_s\left(\frac{d\rho_s}{dt}\right)_r \end{aligned} \tag{23}$$

Equation (23) also describes the CVDV1 and CVDV2 models when A is chosen to equal one and the appropriate relaxation time is used.

Simplification of Equations

In the above equations, the conservation of vibrational energy is expressed in terms of the vibrational energy per unit mass, ϵ_v. However, it is more convenient to

express the equation in terms of the vibrational temperature T_v. This transformation can be accomplished by combining the vibrational energy equation with the species conservation equation, which has the form

$$\frac{\partial}{\partial t}\rho_s + \frac{\partial}{\partial x^j}\rho_s u^j = \frac{\partial}{\partial x_j}\left(\rho D_s \frac{\partial y_s}{\partial x^j}\right) + \dot{w}_s \tag{24}$$

Also, by incorporating the definition of specific heat at constant pressure

$$Cp_{v,s} = \frac{\partial \epsilon_{v,s}}{\partial T_{v,s}} = \frac{k}{m_s}\left(\frac{\theta_{v,s}}{T}\right)^2 \frac{e^{\theta_{v,s}/T}}{(e^{\theta_{v,s}/T}-1)^2} \tag{25}$$

the conservation of vibrational energy can be expressed in terms of T_v as

$$\begin{aligned}\rho_s u^j Cp_{v,s}\frac{\partial T_{v,s}}{\partial x^j} &= \frac{\partial}{\partial x^j}\left(\eta_{v,s}\frac{\partial T_{v,s}}{\partial x^j}\right) + \left(\rho D_s \frac{\partial y_s}{\partial x^j}\right) Cp_{v,s}\frac{\partial T_{v,s}}{\partial x^j} \\ &+ \rho_s \frac{\epsilon^*_{v,s}-\epsilon_{v,s}}{\tau_s}A + \rho_s\frac{\epsilon^{**}_{v,s}-\epsilon_{v,s}}{\tau_e}A_e + (\epsilon_{v,s}-E_s)\left(\frac{d\rho_s}{dt}\right)_f \\ &- (\epsilon_{v,s}-G_s)\left(\frac{d\rho_s}{dt}\right)_r\end{aligned} \tag{26}$$

In developing equation (26) the time derivative was neglected because a steady flow was assumed.

It has also been assumed in previous research[1,11] that a single vibrational temperature adequately describes a flow with more than one vibrational species. If a single vibrational temperature is assumed, the separate vibrational energy conservation equations can be summed to obtain a general equation for T_v as

$$\sum_{s=mol.} (\rho_s u^j Cp_{v,s}) \frac{\partial T_v}{\partial x^j} =$$

$$\frac{\partial}{\partial x^j}(\eta_v \frac{\partial T_v}{\partial x^j}) + (\rho \sum_{s=mol.} (D_s \frac{\partial \rho_s}{\partial x^j} Cp_{v,s}) \frac{\partial T_v}{\partial x^j} \tag{27}$$

$$+ \sum_{s=mol.} \rho_s \frac{(\epsilon^*_{v,s} - \epsilon_{v,s})}{\tau_s} A + \sum_{s=mol.} \rho_s \frac{(\epsilon^{**}_{v,s} - \epsilon_{v,s})}{\tau_e} A_e$$

$$+ \sum_{s=mol.} (\epsilon_{v,s} - E_s) (\frac{d\rho_s}{dt})_f - \sum_{s=mol.} (\epsilon_{v,s} - G_s) (\frac{d\rho_s}{dt})_r$$

Note that with a single vibrational temperature, the number of equations that must be solved is reduced, and the computational efficiency is improved.

VISCOUS SHOCK LAYER ASSUMPTIONS

Assumptions

While the general form of the conservation of vibrational energy is expressed by equation (27), it would be advantageous computationally to cast the equations into a form which takes into account the AOTV flight regime and configuration. Since the viscous shock-layer (VSL) equations have been found to be reliable solvers for high Mach number flows past blunt bodies[15] and because the VSL equations remain hyperbolic-parabolic in both the streamwise and crossflow directions, the VSL assumptions have been incorporated into the vibrational energy equation.

The present VSL equations were developed using the same assumptions as given by Davis[16,17]. Davis first nondimensionalized the Navier-Stokes equations with variables that are of order one in the boundary layer, and then a second set of similar equations was developed by nondimensionalizing the equations with variables that are of order one in the inviscid region. In both sets of equations, terms smaller than second order were ignored. Finally, the two sets of equations were combined into a single set of equations valid to second order from body to shock. Applying these viscous shock-layer assumptions to the vibrational energy equation implies that viscous effects such as thermal conductivity and diffusion can be ignored in the crossflow directions. The resulting viscous shock layer equation for vibrational relaxation in a Cartesian coordinate system, where x is aligned in the direction across the shock layer, can be expressed as

$$\sum_{s=mol.} (\rho_s u Cp_{v,s}) \frac{\partial T_v}{\partial x} + \sum_{s=mol.} (\rho_s v Cp_{v,s}) \frac{\partial T_v}{\partial y} + \sum_{s=mol.} (\rho_s w Cp_{v,s}) \frac{\partial T_v}{\partial z} =$$

$$\frac{\partial}{\partial x}(\eta_v \frac{\partial T_v}{\partial x}) + (\rho \sum_{s=mol.} (D_s \frac{\partial y_s}{\partial x} Cp_{v,s}) \frac{\partial T_v}{\partial x} + \sum_{s=mol.} \rho_s \frac{(\epsilon^*_{v,s} - \epsilon_{v,s})}{\tau_s} A \tag{28}$$

$$+ \sum_{s=mol.} \rho_s \frac{(\epsilon^{**}_{v,s} - \epsilon_{v,s})}{\tau_e} + \sum_{s=mol.} (\epsilon_{v,s} - E_s) (\frac{d\rho_s}{dt})_f$$

$$- \sum_{s=mol.} (\epsilon_{v,s} - G_s) (\frac{d\rho_s}{dt})_r$$

Coordinate Transformation

While the vibrational energy equation is expressed in a Cartesian coordinate system, a coordinate system that would simplify the calculation of boundary conditions at the shock and the body is desired. For this reason, an axisymetric body intrinsic coordinate system is used for the vibrational energy equation. The transformed vibrational energy equation in an s,n,ϕ body intrinsic coordinate system is

$$\frac{1}{h_1} \sum_{s=mol.} (\rho_s u Cp_{v,s}) \frac{\partial T_v}{\partial s} + \sum_{s=mol.} (\rho_s v Cp_{v,s}) \frac{\partial T_v}{\partial n} + \frac{1}{h_3} \sum_{s=mol.} (\rho_s w Cp_{v,s}) \frac{\partial T_v}{\partial \phi} =$$

$$\frac{\epsilon^2}{h_1 h_3} \frac{\partial}{\partial n} (h_1 h_3 \eta_v \frac{\partial T_v}{\partial n}) + \rho \frac{\epsilon^2}{h_1 h_3} \sum_{s=mol.} (D_s \frac{\partial y_s}{\partial n} Cp_{v,s}) \frac{\partial T_v}{\partial n}$$

$$+ \sum_{s=mol.} \rho_s \frac{(\epsilon^*_{v,s} - \epsilon_{v,s})}{\tau_s} A + \sum_{s=mol.} \rho_s \frac{(\epsilon^{**}_{v,s} - \epsilon_{v,s})}{\tau_e}$$

$$+ \sum_{s=mol.} (\epsilon_{v,s} - E_s) (\frac{d\rho_s}{dt})_f - \sum_{s=mol.} (\epsilon_{v,s} - G_s) (\frac{d\rho_s}{dt})_r \tag{29}$$

where s is aligned in the streamwise direction. The shape factors h_1 and h_3 for the body intrinsic coordinate system can be expressed as

$$h_1 = 1 + \kappa_s n \qquad\qquad h_3 = r\frac{(1+\kappa_\phi n\cos\theta_s)}{\cos\theta_\phi} \tag{30}$$

The viscous shock layer equation has been nondimensionalized by the standard relations for which the primed variables represent dimensional values as

$$\begin{aligned}
s &= s'/R_n & \rho &= \rho'/\rho_\infty \\
n &= n'/R_n & p &= p'/\rho_\infty U_\infty^2 \\
u &= u'/u_\infty & \epsilon_{v,s} &= \epsilon'_{v,s}/U_\infty^2 \\
v &= v'/U_\infty & w &= w'/U_\infty \\
\tau &= \tau' R_n/U_\infty & T &= T'Cp/U_\infty^2 \\
T_v &= T'_v Cp/U_\infty^2 & T_e &= T'_e Cp/U_\infty^2 \\
\kappa_s &= \kappa'_s/R_n & \kappa_\phi &= \kappa'_\phi/R_n \\
r &= r'/R_n & \mu &= \mu'/\mu_{ref}
\end{aligned} \tag{31}$$

where

$$\mu_{ref} = \mu_{shock} U_\infty^2/Cp_\infty \qquad\qquad \epsilon^2 = \mu_{ref}/\rho_\infty U_\infty R_n \tag{32}$$

Shock Boundary Conditions

The vibrational temperature at the shock is calculated using a simplified form of equation (29) which accounts for shock slip. Because the shock-wave thickness is small, it is assumed that only a few molecular collisions occur in this region; and, thus, all collisional terms can be ignored. The collisional terms neglected as a result are the Landau-Teller terms and all species production terms, which leaves only the convection, diffusion, and conduction terms. This simplified equation can then be integrated across the shock-wave from freestream temperature to Tv_{shock}, yielding a slip boundary condition expression for Tv_{shock} in terms of $\partial Tv_{shock}/\partial n$.

CONSERVATION EQUATIONS

While the vibrational relaxation process is of primary interest to this research, the results cannot be adequately interpreted without knowledge of the complete flow model. Therefore, the equations for species, n-momentum, s-momentum, ϕ-momentum, electron energy, and full energy conservation will be presented. Like the vibrational energy equation, all equations are written in an axisymetric body centered coordinate system, and each equation is bound by VSL simplifying assumptions. The governing equations which have been nondimensionalized using equations (31) and (32) can be expressed as follows.[18]

Species Conservation:

$$\frac{\partial h_3 \rho_s u}{\partial s} + \frac{\partial h_1 h_3 \rho_s v}{\partial n} + \frac{\partial h_1 \rho_s w}{\partial \phi} = \epsilon^2 \frac{\rho}{h_1 h_3} \frac{\partial}{\partial n} \left(h_1 h_3 D_s \frac{\partial y_s}{\partial n} \right) + \dot{w}_s \tag{33}$$

Because the flow is in chemical nonequilibrium, equations governing species concentration must be solved to determine the mixture composition. Equation (33) accounts for the mass flux of species s due to convection and diffusion, as well as the production of species s from chemical reactions. A mass averaged binary diffusion coefficient is used to calculate diffusion velocity, and species production rates are governed by the collisional reaction rate system in Appendix II. The shape factors h_1 and h_3 are given by Equation (30).

s-Momentum Conservation:

$$\rho\left(\frac{u}{h_1}\frac{\partial u}{\partial s}+v\frac{\partial u}{\partial n}+\frac{w}{h_3}\frac{\partial u}{\partial \phi}+\frac{uv}{h_1}\frac{\partial h_1}{\partial n}+\frac{uw}{h_1 h_3}\frac{\partial h_1}{\partial \phi}-\frac{w^2}{h_1 h_3}\frac{\partial h_3}{\partial s}\right) = -\frac{1}{h_1}\frac{\partial p}{\partial s}$$

$$+\ \epsilon^2\frac{\partial}{\partial n}\left[h_1\frac{\partial}{\partial n}\left(\frac{u}{h_1}\right)\mu\right] + \epsilon^2\left(\frac{2}{h_1}\frac{\partial h_1}{\partial n}+\frac{1}{h_3}\frac{\partial h_3}{\partial n}\right)h_1\mu\frac{\partial}{\partial n}\left(\frac{u}{h_1}\right) \tag{34}$$

n-Momentum Conservation:

$$\rho\left(\frac{u}{h_1}\frac{\partial v}{\partial s}+v\frac{\partial v}{\partial n}+\frac{w}{h_3}\frac{\partial v}{\partial \phi}-\frac{u^2}{h_1}\frac{\partial h_1}{\partial n}-\frac{w^2}{h_3}\frac{\partial h_3}{\partial n}\right) = -\frac{\partial p}{\partial n} \tag{35}$$

ϕ-Momentum Conservation:

$$\rho\left(\frac{u}{h_1}\frac{\partial w}{\partial s}+v\frac{\partial w}{\partial n}+\frac{w}{h_3}\frac{\partial w}{\partial \phi}+\frac{uw}{h_1 h_3}\frac{\partial h_3}{\partial s}+\frac{vw}{h_3}\frac{\partial h_3}{\partial n}-\frac{u^2}{h_1 h_3}\frac{\partial h_1}{\partial \phi}\right) = -\frac{1}{h_3}\frac{\partial p}{\partial \phi}$$

$$\epsilon^2\frac{\partial}{\partial n}\left[\mu h_3\frac{\partial}{\partial n}\left(\frac{w}{h_3}\right)\right] + \epsilon^2\left(\frac{1}{h_1}\frac{\partial h_1}{\partial n}+\frac{2}{h_3}\frac{\partial h_3}{\partial n}\right)h_3\mu\frac{\partial}{\partial n}\left(\frac{w}{h_3}\right) \tag{36}$$

Equations (34-36) model the conservation of momentum in the three coordinate directions and account for the convection of momentum, viscous forces in the *n*-direction, and pressure forces.

Total Energy Conservation:

$$\rho Cp_{t-r}\left(\frac{u}{h_1}\frac{\partial T}{\partial s}+v\frac{\partial T}{\partial n}+\frac{w}{h_3}\frac{\partial T}{\partial \phi}\right) + \rho Cp_v\left(\frac{u}{h_1}\frac{\partial T_v}{\partial s}+v\frac{\partial T_v}{\partial n}+\frac{w}{h_3}\frac{\partial T_v}{\partial \phi}\right)$$

$$+ \rho Cp_e\left(\frac{u}{h_1}\frac{\partial T_e}{\partial s}+v\frac{\partial T_e}{\partial n}+\frac{w}{h_3}\frac{\partial T_e}{\partial \phi}\right) - \left(\frac{u}{h_1}\frac{\partial p}{\partial s}+v\frac{\partial p}{\partial n}+\frac{w}{h_3}\frac{\partial T}{\partial \phi}\right) =$$

$$\frac{e^2}{h_1 h_3}\frac{\partial}{\partial n}\left[h_1 h_3\left(\eta_{t-r}\frac{\partial T}{\partial n}+\eta_v\frac{\partial T_v}{\partial n}+\eta_e\frac{\partial T_e}{\partial n}\right)\right] - \sum_{s=all} h_s \dot{w}_s - Q_{rad}$$

$$+ \frac{e^2}{h_1 h_3}\left[\rho\sum_{s=all}\left(D_s\frac{\partial y_s}{\partial n}Cp_{t-r,s}\right)\frac{\partial T}{\partial n} + \rho\sum_{s=mol.}\left(D_s\frac{\partial y_s}{\partial n}Cp_{v,s}\right)\frac{\partial T_v}{\partial n}\right.$$

$$+ \rho\left(D_s Cp_e\frac{\partial y_e}{\partial n}\right)\frac{\partial T_e}{\partial n} - \mu u\frac{\partial h_1}{\partial n}\frac{\partial}{\partial_n}\left(\frac{u}{h_1}\right)$$

$$\left. + h_1\mu\frac{\partial u}{\partial n}\frac{\partial}{\partial n}\left(\frac{u}{h_1}\right) + \frac{\partial w}{\partial n}h_3\frac{\partial}{\partial n}\left(\frac{w}{h_3}\right)\mu - w\frac{\partial h_3}{\partial n}\frac{\partial}{\partial n}\left(\frac{w}{h_3}\right)\mu\right] \tag{37}$$

Equation (37) represents the conservation of total energy and includes the effects of convective heat transfer, thermal conduction of internal energy, diffusion of internal energy, loss of internal energy by radiation, energy change due to species production and depletion, viscous forces in the *n*-direction, and pressure forces. Because the total energy equation is expressed in terms of temperature, the three temperature thermal model complicates the convective, conductive, and diffusive terms, since these phenomena are dependent on the local spatial temperature gradient. Since the internal energy modes are described by three different temperatures (T, T_v, T_e), thermal convection, conduction, and diffusion will be dependent on three different spatial temperature gradients as shown by Equation (37).

In the present study, two different electron energy models given by Carlson and Gally[19] are used and studied. The first is

Quasi-equilibrium Electron Energy Conservation:

$$\dot{w}_e h_e^{tr} + \dot{w}_e \frac{u^2}{2} = \sum_{s=all} \xi_{es} + Q_e - \sum_{s=mol.} \rho_s \frac{\epsilon_{v,s}^{**} - \epsilon_{v,s}}{\tau_e} \tag{38}$$

The quasi-equilibrium electron energy model (QEE) is a free electron model for which all derivatives in the free electron energy equation are neglected. The QEE model accounts for elastic and inelastic collisional effects as well as vibrational-electron coupling. The second electron energy model is

Quasi-equilibrium Electron-electronic Energy Conservation:

$$\dot{w}_e h_e^{tr} + \sum_{s=all} \dot{w}_s h_s^e - \dot{w}_e \frac{u^2}{2} = \sum_{s=all} \xi_{es} + Q_e - \sum_{s=mol.} \rho_s \frac{\epsilon_{v,s}^{**} - \epsilon_{v,s}}{\tau_e} \tag{39}$$

The quasi-equilibrium electron-electronic energy model (QEEE), while similar to the QEE model, also accounts for the energy stored in electronic states of each species, assuming that the energy of such states is characterized by the electron-electronic temperature, T_e.

For completeness, the vibrational energy equation that was developed earlier is presented again.

Vibrational Energy Conservation:

$$\frac{1}{h_1}\sum_{s=mol.}(\rho_s u Cp_{v,s})\frac{\partial T_v}{\partial s}+\sum_{s=mol.}(\rho_s v Cp_{v,s})\frac{\partial T_v}{\partial n}+\frac{1}{h_3}\sum_{s=mol.}(\rho_s w Cp_{v,s})\frac{\partial T_v}{\partial \phi} =$$

$$\frac{\epsilon^2}{h_1 h_3}\frac{\partial}{\partial n}(h_1 h_3 \eta_v \frac{\partial T_v}{\partial n}) + \rho\frac{\epsilon^2}{h_1 h_3}\sum_{s=mol.}(D_s\frac{\partial y_s}{\partial n}Cp_{v,s})\frac{\partial T_v}{\partial n}$$

$$+\sum_{s=mol.}\rho_s\frac{(\epsilon^*_{v,s}-\epsilon_{v,s})}{\tau_s}A + \sum_{s=mol.}\rho_s\frac{(\epsilon^{**}_{v,s}-\epsilon_{v,s})}{\tau_e}$$

$$+\sum_{s=mol.}(\epsilon_{v,s}-E_s)(\frac{d\rho_s}{dt})_f - \sum_{s=mol.}(\epsilon_{v,s}-G_s)(\frac{d\rho_s}{dt})_r \tag{29}$$

The conditions at the shock front are initially calculated by using the standard Rankine-Hugonoit relations. Once the initial shock conditions are determined, shock slip is included by integrating the conservation equations across the shock wave and neglecting all collisional terms. Effectively, shock slip allows for diffusion and thermal conduction at the downstream side of the shock-wave. However, collisional effects or chemical reactions are neglected because the shock-wave thickness is assumed sufficiently small that only a few collisions occur within it.

METHOD OF SOLUTION

Finite Difference Formulation

A finite-difference method like the one used by Frieders and Lewis[18,20] is used to solve the vibrational energy equation. In an axisymetric body-centered coordinate system the vibrational energy equation can be expressed in the standard form

$$A_0 \frac{\partial^2 T_v}{\partial n^2} + A_1 \frac{\partial T_v}{\partial n} + A_2 T_v + A_3 + A_4 \frac{\partial T_v}{\partial s} + A_5 \frac{\partial T_v}{\partial \phi} = 0 \qquad (40)$$

For the stagnation streamline, crossflow derivatives are neglected and the standard equation is expressed as

$$A_0 \frac{\partial^2 T_v}{\partial n^2} + A_1 \frac{\partial T_v}{\partial n} + A_2 T_v + A_3 = 0 \qquad (41)$$

where the finite-difference expressions for derivatives at grid point j are evaluated using a first order Taylor series expansion as

$$\frac{\partial^2 Tv}{\partial n^2} = \frac{2\,[Tv_{j+1} - (1+k)\,Tv_j + kTv_{j-1}]}{(n_{j+1}-n_j)^2 + k(n_j-n_{j-1})^2}$$

$$\frac{\partial T_v}{\partial n} = \frac{Tv_{j+1} - (1-k)^2 Tv_j - k^2 Tv_{j-1}}{(n_{j+1}-n_j) + k^2(n_j-n_{j-1})} \qquad (42)$$

$$k = \frac{n_{j+1}-n_j}{n_j-n_{j-1}}$$

Substituting equations (42) into equation (41) yields an algebraic expression for $T_{v,j-1}$, $T_{v,j}$, and $T_{v,j+1}$ that can be written for each grid point j. The resulting set of coupled

algebraic equations can then be solved simultaneously for $T_{v,j}$ at each grid point along the stagnation streamline. In the cascade order of solution[18] the vibrational energy equation is solved after the full energy and electron energy equations. The entire solution scheme involves an iterative process to account for the strong coupling among the governing equations.

Linearization of Explicit Terms

Because several of the explicit terms on the right hand side of the vibrational energy equation are a function of T_v, these terms will lag during the iterative process, which adds instability to the solution scheme. However, the process can be stabilized by the linearization of the explicit terms dependent on T_v by expressing the terms at time step $n+1$ as a Taylor series expansion about time step n; ie.

$$J^{n+1} = J^{n} + \frac{\partial J}{\partial T_v}(T_v^{n+1} - T_v^{n}) \tag{43}$$

where J represents any explicit term that is a function of T_v. The linearization of these terms effectively adds an implicit counterpart to the vibrational energy equation that increases the stability of the iterative solution procedure. Thus, it was necessary to linearize the Landau-Teller terms as

$$\begin{aligned}
\left(\rho_s \frac{\epsilon^{*}_{v,s} - \epsilon_{v,s}}{\tau_s} A\right)^{n+1} &= \left(\rho_s \frac{\epsilon^{*}_{v,s} - \epsilon_{v,s}}{\tau_s} A\right)^{n} - \rho_s \frac{Cp_{v,s}}{\tau_s}(T_v^{n+1} - T_v^{n}) \\
\left(\rho_s \frac{\epsilon^{**}_{v,s} - \epsilon_{v,s}}{\tau_e} A_e\right)^{n+1} &= \left(\rho_s \frac{\epsilon^{**}_{v,s} - \epsilon_{v,s}}{\tau_e} A_e\right)^{n} - \rho_s \frac{Cp_{s,v}}{\tau_e}(T_v^{n+1} - T_v^{n})
\end{aligned} \tag{44}$$

and the coupled dissociation-vibration terms as

$$[(e_{v,s}-E_s)(\frac{d\rho_s}{dt})_f]^{n+1} = [(e_{v,s}-E_s)(\frac{d\rho_s}{dt})_f]^n + (Cp_{v,s}-\frac{\partial E_s}{\partial T_v})(\frac{d\rho_s}{dt})_f(T_v^{n+1}-T_v^n)$$

$$[(e_{v,s}-G_s)(\frac{d\rho_s}{dt})_r]^{n+1} = [(e_{v,s}-G_s)(\frac{d\rho_s}{dt})_r]^n + (Cp_{v,s}-\frac{\partial G_s}{\partial T_v})(\frac{d\rho_s}{dt})_r(T_v^{n+1}-T_v^n) \tag{45}$$

For stability in the solution scheme of the electron energy equation, a similar linearization of the vibration-electron coupling term was required. The term was incorporated into the electron energy equation as

$$\sum_{s=mol.}(\rho_s\frac{\epsilon_{v,s}^{**}-\epsilon_{v,s}}{\tau_e}A_e)^{n+1} = \sum_{s=mol.}(\rho_s\frac{\epsilon_{v,s}^{**}-\epsilon_{v,s}}{\tau_e}A_e)^n + \sum_{s=mol.}(\rho_s\frac{\partial\epsilon_{v,s}^{**}}{\partial T_e}A_e)(T_e^{n+1}-T_e^n) \tag{46}$$

RESULTS AND DISCUSSION

Several different trajectory point conditions (Table 1) for the AOTV flowfield have been considered, and stagnation streamline solutions to the flowfield at these trajectory points have been computed assuming a nitrogen atmosphere. Current results present flow characteristics such as temperature and mole fraction along the stagnation streamline, utilizing a ninety-nine point computational grid between the wall and shock front. For all cases the AOTV nose radius is assumed to be 2.3 meters, and a cold wall boundary condition of 1,650° K is imposed on heavy particle, electron, and vibrational temperatures. For species boundary conditions, a partially catalytic wall is assumed where ion concentrations are zero and neutral species concentration gradients are zero at the wall. In the freestream, a pure diatomic nitrogen atmosphere is assumed.

U_∞ km/sec	ρ_∞ kg/m^3	T_∞ K	Altitude km
8.915	2.683×10^{-11}	197.13	77.9
9.326	4.292×10^{-11}	199.44	75.2
12.0	1.927×10^{-11}	180.65	80.0
14.0	1.927×10^{-11}	180.65	80.0
16.0	1.927×10^{-11}	180.65	80.0

Table 1: AOTV Trajectory Point Conditions

In a comparative analysis of the vibrational relaxation process, eight different temperature models (Table 2) have been studied at flight velocities of 8.915, 9.326, and 12 km/sec. Two-temperature models that include either the QEE or QEEE electron temperature model have been compared to three temperature models that include the CVDV model with and without Park corrections to the translational-vibrational coupling term. Also, the effects of the vibration-electron coupling term have been studied at 8.915, 9.326, and 12 km/sec.

Case #	T_e Model	T_v Model	T_e-T_v Coupling
1	QEE	T_v=T	uncoupled
2	QEEE	T_v=T	uncoupled
3	QEEE	CVDV1	coupled
4	QEEE	CVDV2	coupled
5	QEE	CVDV3	coupled
6	QEEE	CVDV3	coupled
7	QEEE	CVDV4	coupled
8	QEEE	CVDV3	uncoupled

Table 2: Temperature Models Studied at 8.9, 9.3, and 12 km/sec

Finally, at velocities of 14 and 16 km/sec the complete three temperature model (Case 6) is compared to the complete two temperature model (Case 2).

8.915 km/sec, 75 km

Figures 1-8 present the temperature and species distributions for cases 1 through 8 respectively along the stagnation streamline at a freestream velocity of 8.915 km/sec

and an altitude of 75 km. Distance along the stream line is given by ETA, where ETA is the local distance from the body nondimensionalized by the shock stand-off distance, with the wall boundary at ETA=0 and the shock boundary at ETA=1.

Figures 1 and 2 are results of two-temperature models and will serve as comparisons to the three-temperature models studied in the current research. Temperature and species plots for the QEEE/CVDV1 model are shown in Figure 3. Here, vibrational and electron temperatures are so strongly coupled that the electron temperature and vibrational temperature are driven to the same value, and it is concluded that vibration-electron coupling is the dominant term in the QEEE model. Directly after the shock, the large gradient in vibrational temperature is caused by the translational-vibrational coupling term in the CVDV1 model. Also, soon after the shock, rapid dissociation significantly depletes translational energy causing a sharp drop in the heavy particle temperature. Because translational-vibrational coupling in the CVDV1 model is nearly linearly proportional to the difference in T and T_v, the magnitude of the $T-T_v$ coupling term decreases as the two temperatures converge and dissociation-vibration effects become more significant. The effects of dissociation on T_v are apparent at the peak of the T_v profile (ETA=0.94) where T_v begins to drop rather than continuing to increase towards T. Dissociation tends to lower the average vibrational energy since dissociation will occur more easily at the higher vibrational energy states.

The vibrational temperature at the shock front is based on a shock slip condition for which the initial vibrational temperature ahead of the shock is equal to T_∞, but the diffusion and conduction of vibrational energy towards the shock wave increase the

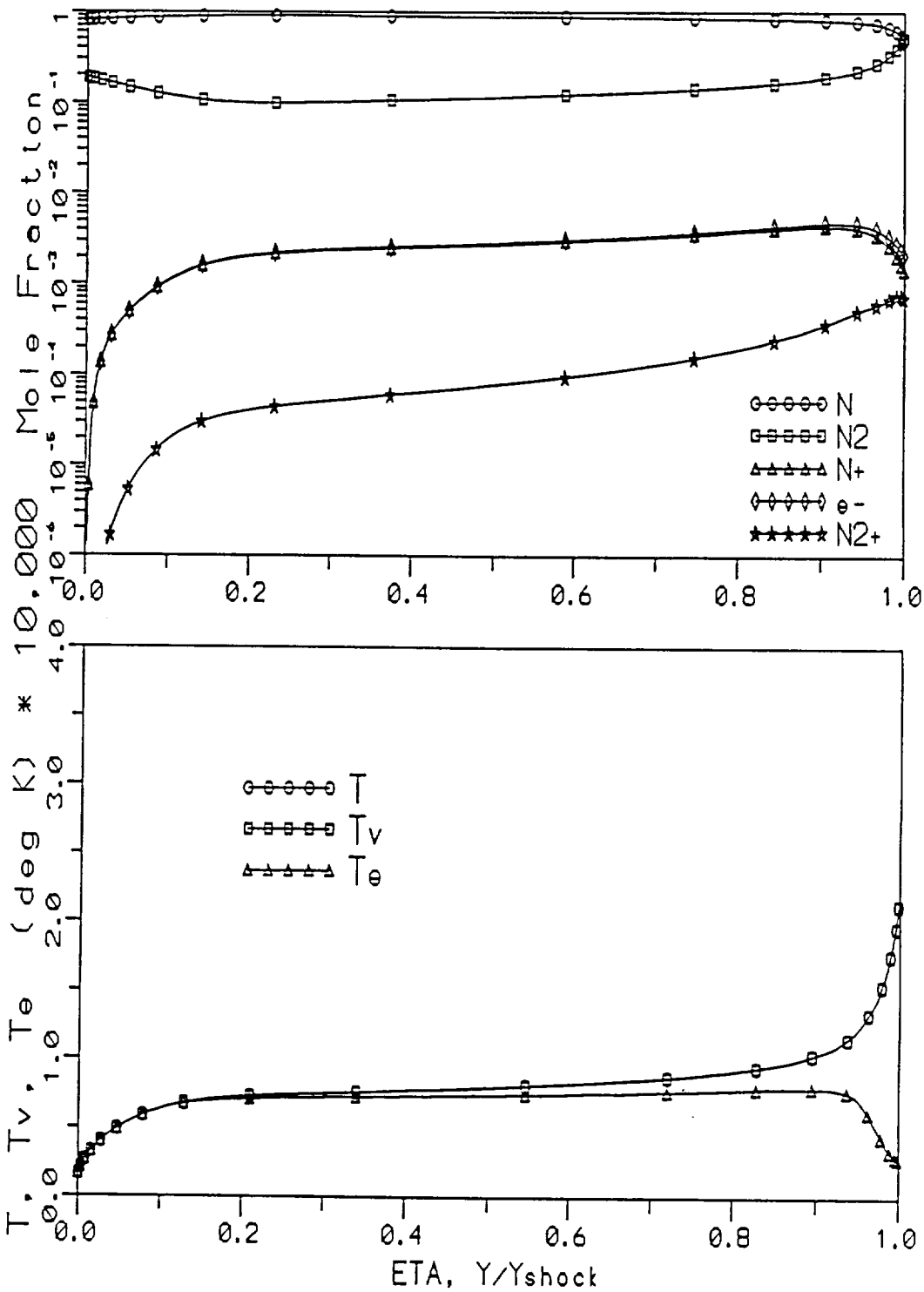

Figure 1: Uncoupled QEE/T_v=T Model at V_∞=8.915 km/sec
Yshock=12.28 cm

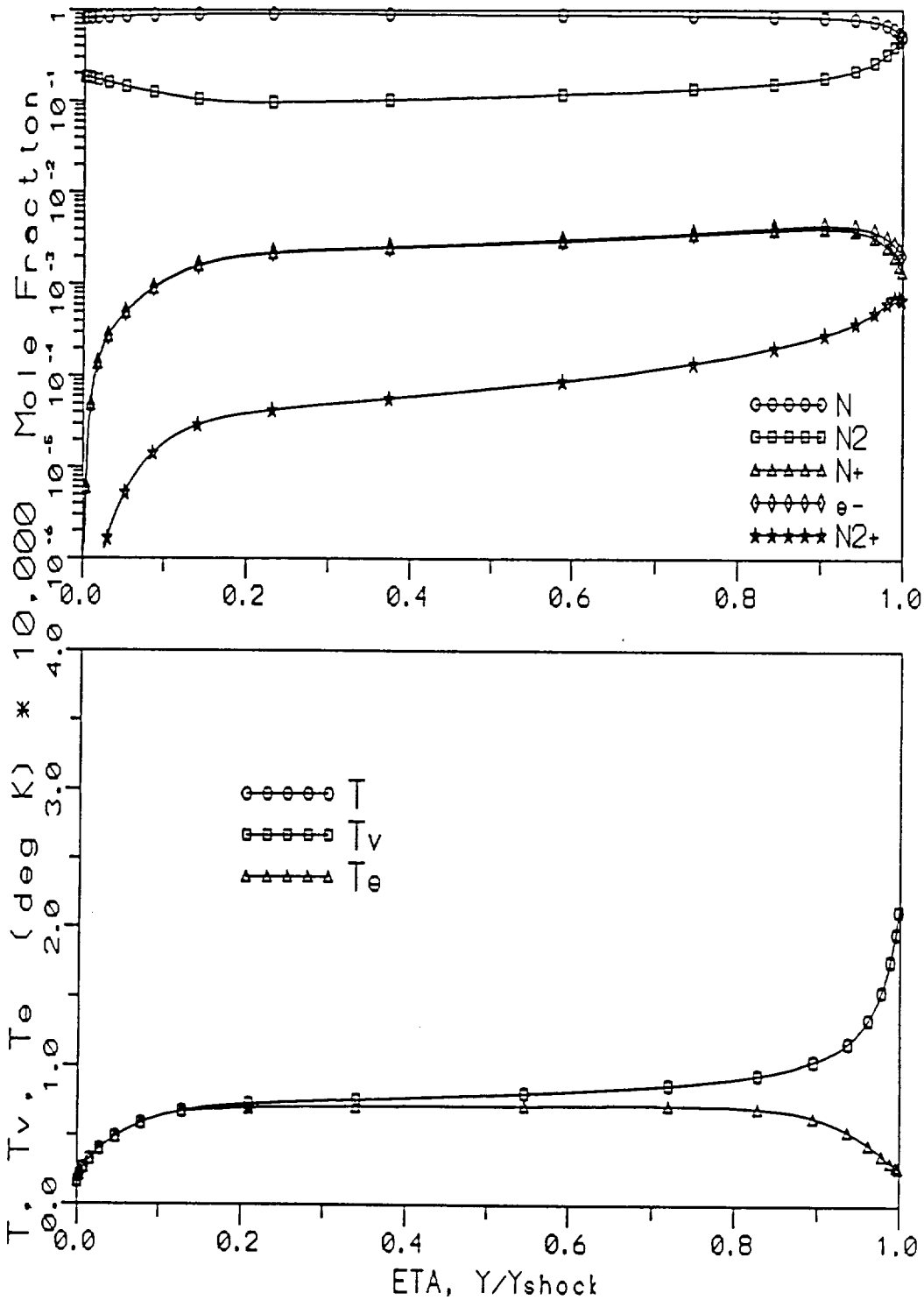

Figure 2: Uncoupled QEEE/T_v=T at U_∞=8.915 km/sec
Yshock=12.33 cm

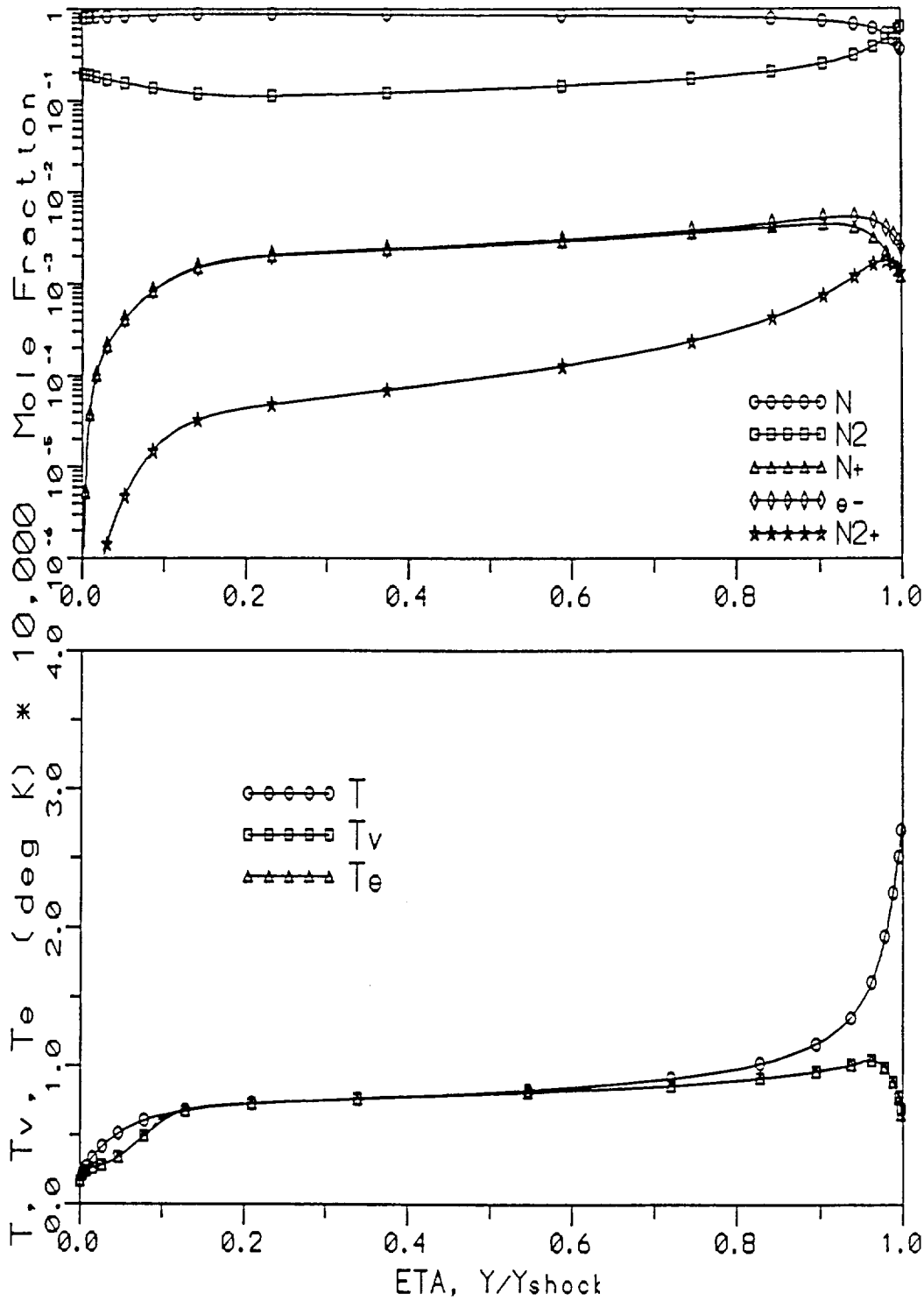

Figure 3: Coupled QEEE/CVDV1 Model at U_∞=8.915 km/sec
Yshock=12.81 cm

vibrational energy immediately behind the shock. At the wall T_v decreases to satisfy the wall boundary condition on temperature. However, T_v is less than T near the wall due to the diffusion of vibrational energy away from the wall. Because a cold wall boundary condition exists, the equilibrium temperature near the wall decreases, causing a recombination of nitrogen atoms near the wall, which increases the N_2 concentration at the wall and results in the diffusion of N_2 molecules away from the wall. The N_2 molecules diffusing away from the wall transport a lower average vibrational energy to the region adjacent to the wall, thus lowering the vibrational temperature adjacent to the wall. This diffusion of energy away from the wall, however, does not significantly affect the heavy particle temperature because much of the internal energy that is characterized by the translational temperature is contained in monatomic nitrogen. Since there is not a significant N concentration gradient at the wall, the diffusion of N away from the wall is minimal, and there will be little diffusional effects on T near the wall. Thus, as stated earlier, the phenomenon of T_v dropping below T near the wall is a result of cold N_2 diffusing away from the wall and lowering the average vibrational energy or temperature.

The CVDV1 model also includes the retarding effects of vibrational nonequilibrium on dissociation rates. By examining N and N_2 concentrations in Figures 2 and 3 it is clear that the depletion rate of N_2 and consequently the production rate of N have been reduced in the CVDV1 model. This phenomenon is to be expected since a lower vibrational energy reduces the number of molecular collisions with sufficient energy to induce dissociation.

The temperature and species results for the CVDV2 model are presented in

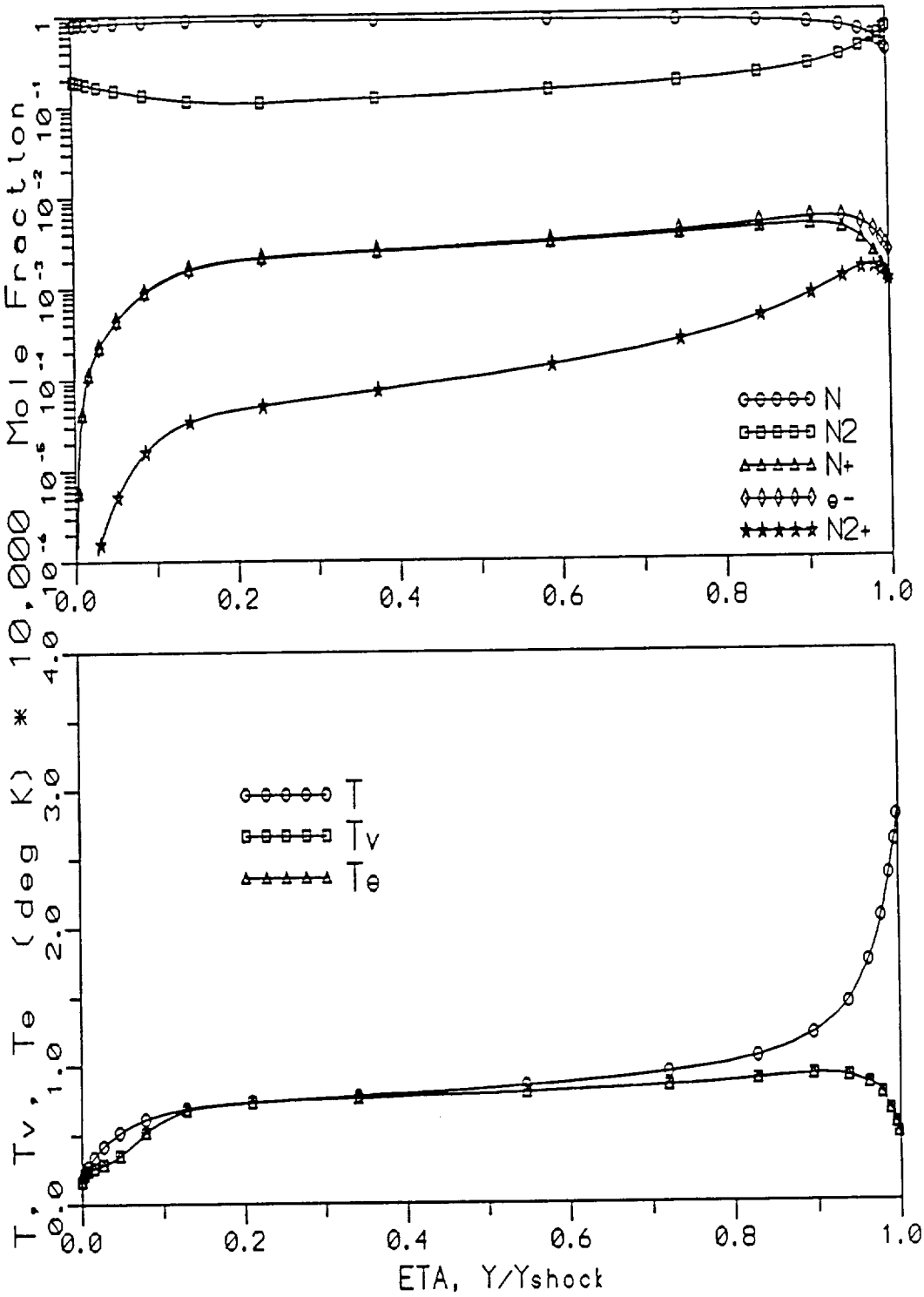

Figure 4: Coupled QEEE/CVDV2 Model at U_∞=8.915 km/sec
Yshock=13.16 cm

Figure 4. The CVDV2 model is distinguished from the CVDV1 model by the modification to the semi-empirical expression for the relaxation time that accounts for the overprediction of collision cross sections at high temperatures. By comparing Figures 3 and 4, it is obvious that the Park modification to the relaxation time has slowed the vibrational relaxation process. The T_v gradient at the shock is less steep when compared to the CVDV1 model and the T-T_v equilibration time, as indicated by the peak in T_v, is much longer. For the CVDV2 model, thermal equilibration occurs at ETA=0.3 while thermal equilibration occurs much earlier (ETA=0.5) for the CVDV1 model.

Figures 5 and 6 describe the temperature and species solutions for the coupled QEE/CVDV3 and coupled QEEE/CVDV3 models. Because the dominant term in both the QEE and QEEE energy equations is the T_v-T_e coupling term, the results from these two cases are very similar. The CVDV3 vibrational energy model attempts to correct for the diffusive nature of the vibrational relaxation process by altering the linear nature of the T-T_v coupling term. When comparing Figures 5 and 6, it is concluded that the CVDV3 model only affects the T_v profile near the shock, unlike the CVDV2 model that slowed the overall relaxation process. With CVDV3, T_v only appears to be affected near the shock front and factor incorporated into the CVDV3 model becomes negligible soon after the heavy particle temperature drops. In general, modifying the T-T_v coupling term to better model the diffusive nature will effectively decreases the T_v temperature directly behind the shock.

The effects of altering the minimum cross section coefficient employed in the relaxation time calculation can be seen by comparing Figures 6 and 7. The results of

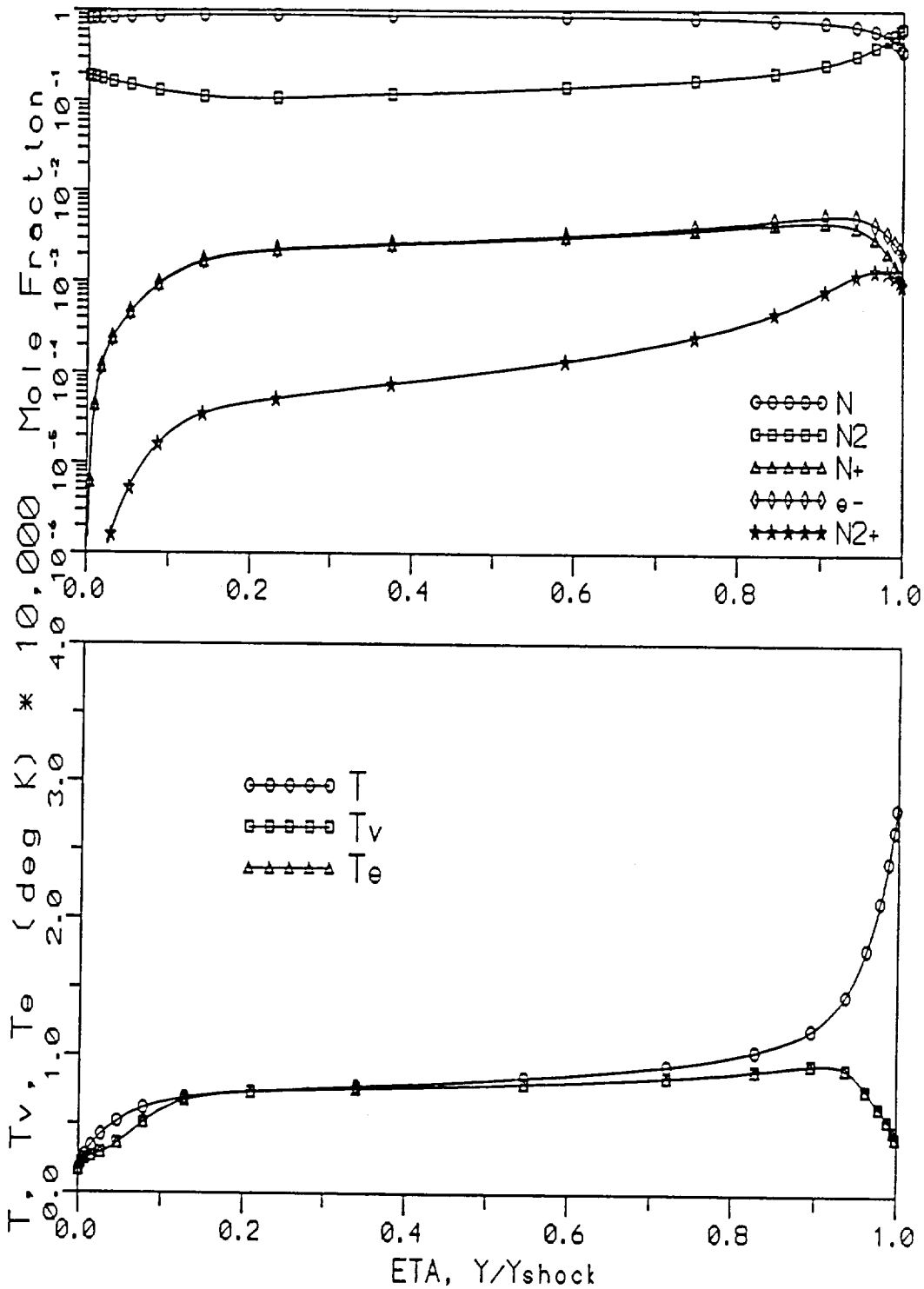

Figure 5: Couple QEE/CVDV3 Model at U_∞=8.915 km/sec
Yshock=13.20 cm

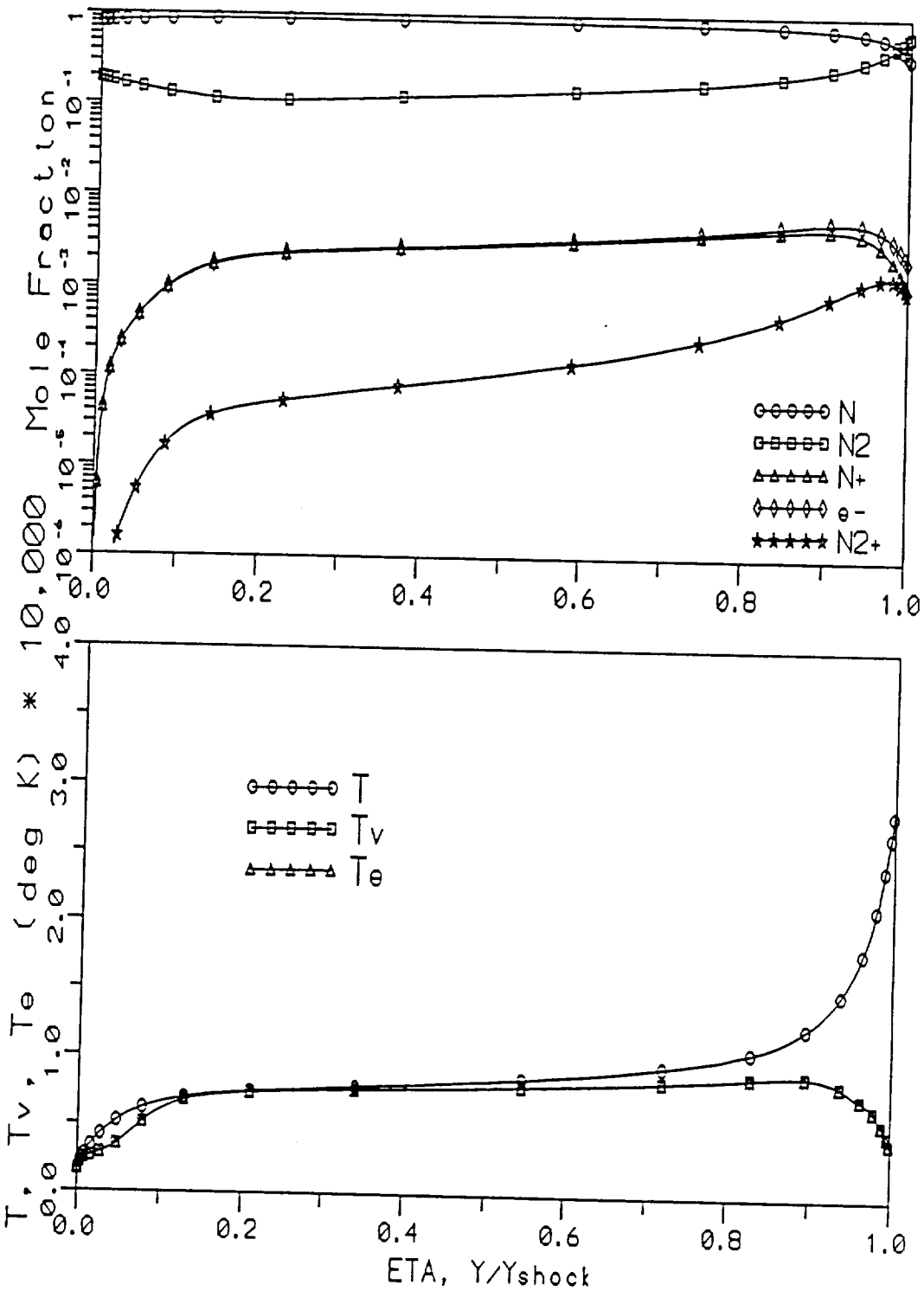

Figure 6: Coupled QEEE/CVDV3 Model at U_∞=8.915 km/sec
Yshock=13.29 cm

the CVDV4 model presented in Figure 7 suggest that the smaller minimum cross section coefficient leads to a longer relaxation process as a result of the relaxation time being increased by the decrease in the minimum cross section coefficient. It is interesting to note that the CVDV2 and CVDV4 models affect the length of the vibrational relaxation process even though the modifications in these models only significantly alter the relaxation time calculations at high temperatures. On the other hand, the CVDV3 model for the diffusive nature of the vibrational relaxation process does not change the length of the overall relaxation process, yet the modification in the model directly affects calculations at all points not in thermal equilibrium.

The effects of coupling between the vibrational and electron energy can be studied by uncoupling the two equations and comparing the answers with coupled results. This uncoupling can be accomplished by eliminating the Landau-Teller term that models the vibrational-electron energy transfer. Thus, the results of an uncoupled QEEE/CVDV3 model presented in Figure 8 which, when compared to the coupled results of Figure 6, show that there is a strong coupling between electron and vibrational energy that should not be ignored. It should be noted that while coupling the vibrational and electron energy equations significantly raises the T_e profile, the T_v profile at these conditions, is only lowered slightly by vibrational-electron energy transfer.

A comparison of T_v profiles for the different vibrational relaxation models is shown on Figure 9. Because the vibrational temperature at the shock front is dependent on the diffusion and conduction of vibrational energy, there are significant temperature differences at the shock for each vibrational relaxation model. Effectively, a larger

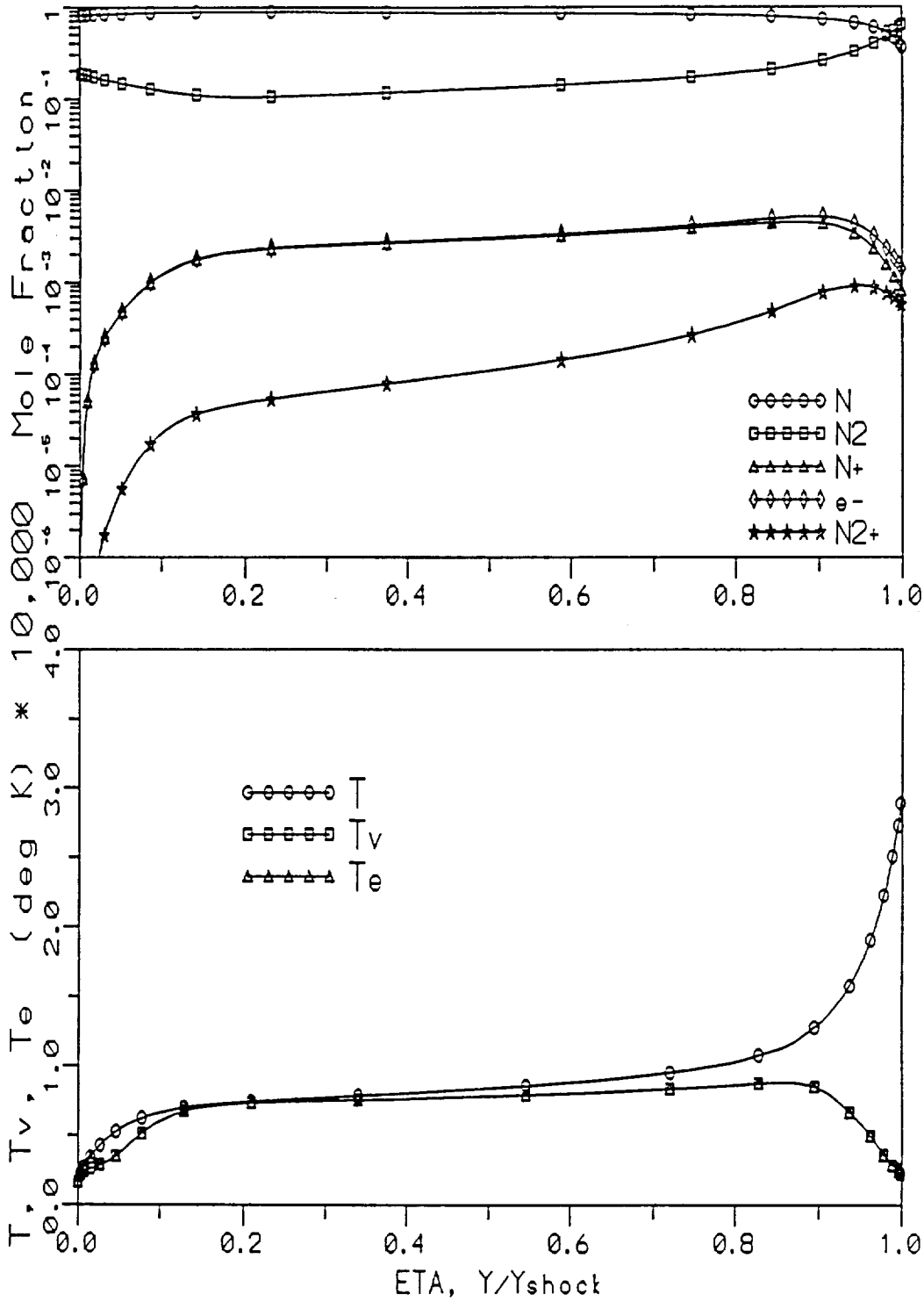

Figure 7: Coupled QEEE/CVDV4 Model at U_∞=8.915 km/sec
Yshock=13.55 cm

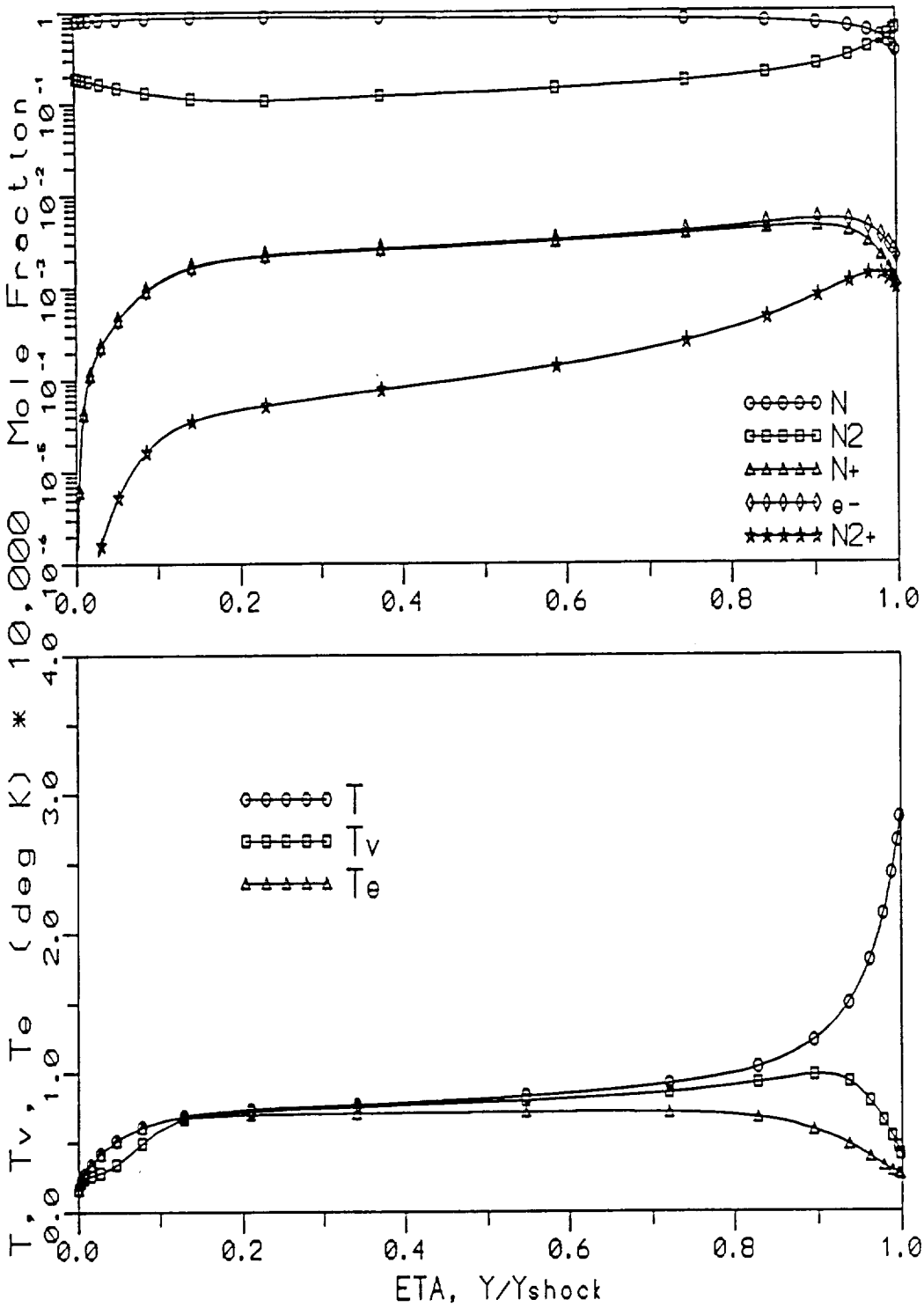

Figure 8: Uncoupled QEEE/CVDV3 Model at U_∞=8.915 km/sec
Yshock=13.27 cm

temperature gradient at the shock causes a higher shock temperature since conduction of vibrational energy is greater for large temperature gradients. As expected, the fastest translational equilibration as indicated by the location of the peak, is seen in the CVDV1 model. The effect of the CVDV2 model is to slow the relaxation process by limiting the relaxation time at higher temperatures, which is confirmed when comparing the CVDV1 and CVDV2 T_v profiles. For each of the CVDV3 models shown in Figure 9, it is clear that the initial temperature gradient at the shock has been decreased as compared to the CVDV1 and CVDV2 models. This trend is expected since the coefficient used in the CVDV3 model will always be less than unity near the shock front, resulting in a decrease in magnitude of the T-T_v coupling term.

When examining the coupled and uncoupled CVDV3 models, it is concluded that not only is the T_v-T_e term significant in the vibrational relaxation process, but also the choice of either the QEE or QEEE models is important to the relaxation process. Since electron temperature is lower than vibrational temperature T_v-T_e coupling lowers the vibrational temperature. Thus, as shown in Figure 9, the uncoupled CVDV3 model has the highest values for T_v, the coupled QEE/CVDV3 model has slightly lower T_v values, and the coupled QEEE/CVDV3 model has the lowest T_v values of the three CVDV3 models since the QEEE electron energy model predicts slightly lower electron temperatures than the QEE model. Also, when comparing the CVDV4 model to the CVDV3 models, a longer relaxation time is calculated in the CVDV4 model causing the slower relaxation process.

Finally, it should be noted that the differences in each of the four CVDV models have very little effect on the species concentration profiles. The coupling factor that

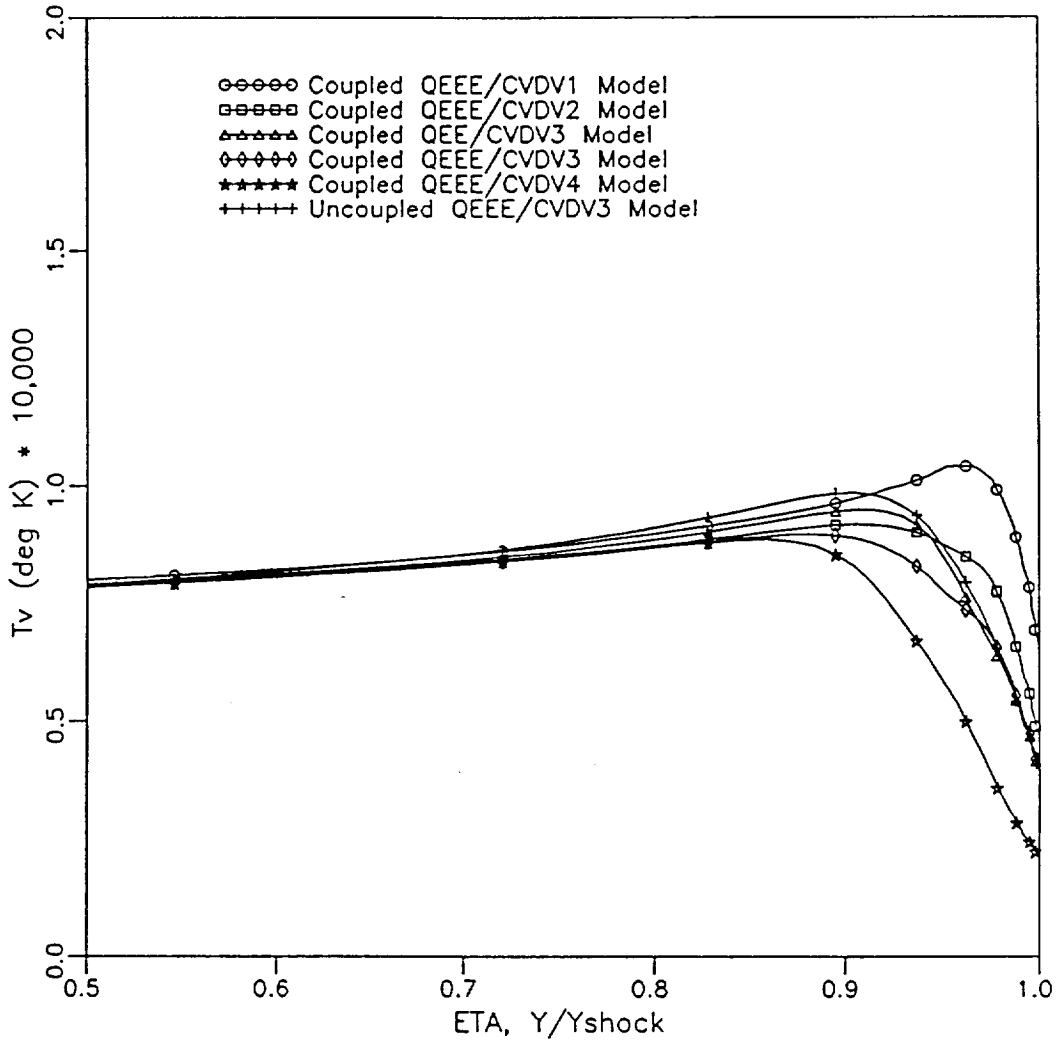

Figure 9: Comparison of CVDV Models at U_∞=8.915 km/sec

governs vibrational effects on dissociation has the identical form in each model, and the relatively minor changes in T_v for each model do not significantly affect the coupling term or the dissociation rates.

9.326 km/sec, 75.2 km

Temperature and species results from computer runs for each of the temperature models in Table 1 at the freestream velocity of 9.326 km/sec are given in Figures 10-

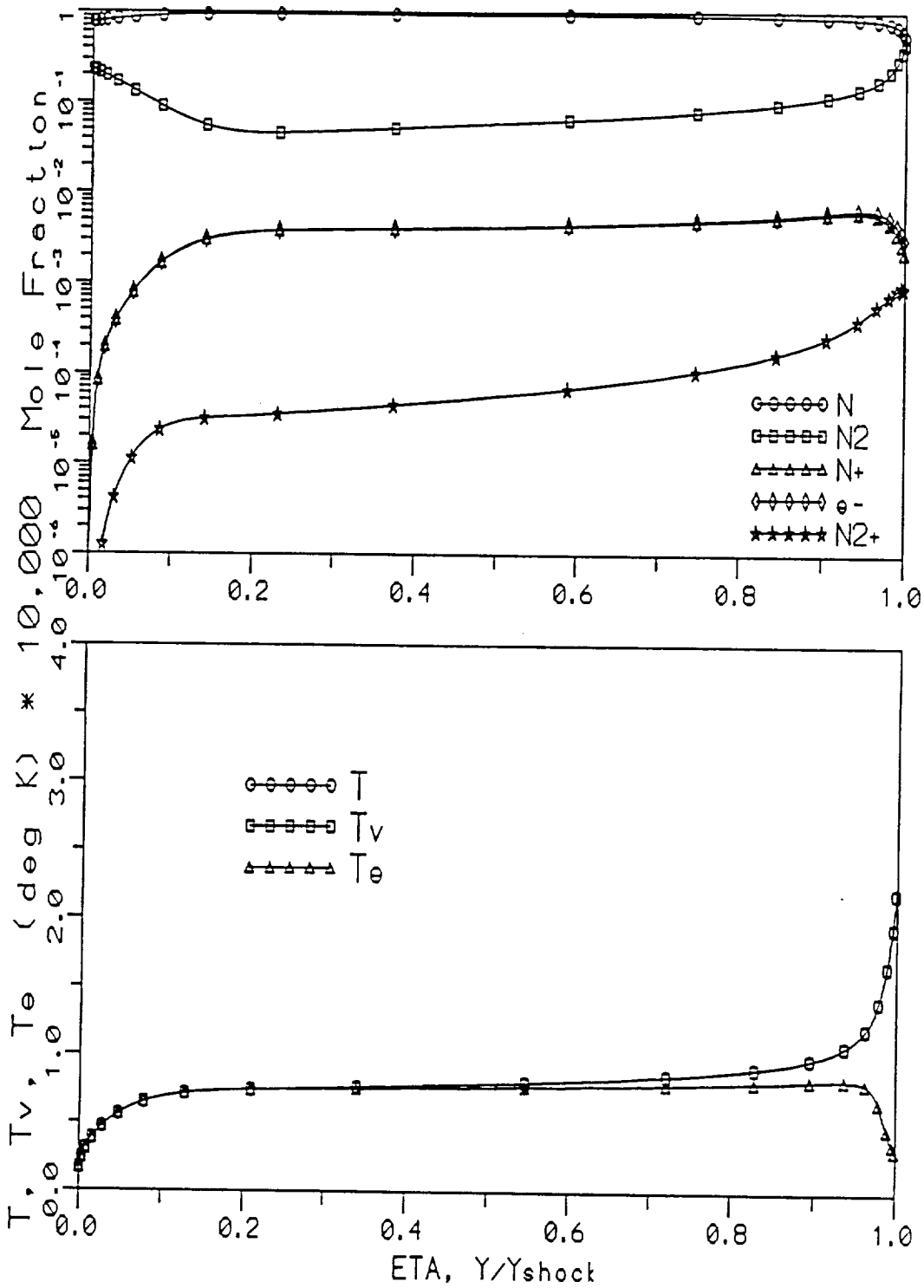

Figure 10: Uncoupled QEE/T_v=T Model at U_∞=9.326 km/sec
Yshock=11.71 cm

17. The two temperature model results shown in Figures 10 and 11 have a slightly higher equilibrium temperature and a greater degree of dissociation compared to the two temperature results at 8.915 km/sec. For the CVDV1 model results shown in Figure 12, dissociation rates are slowed down due to vibration-dissociation effects; however, effects of the vibration-dissociation coupling appear to be less significant at 9.326 km/sec than at 8.915 km/sec. Similar trends are seen in each of the CVDV models when compared to comparable results at 8.915 km/sec.

To better analyze the differences in each of the temperature models at the higher speed of 9.326 km/sec, the T_v profiles are plotted together in Figure 18, which shows that the relaxation process predicted by each model is significantly faster than the results given in Figure 9. This difference in relaxation time is attributed to the significant differences in freestream density in that the higher freestream density at 75.2 km leads to a faster relaxation process. Also, because the results are plotted along ETA (Y/Yshock), different shock stand off distances will affect the relative dimensions of each plot.

When comparing the results of the CVDV1 and CVDV2 models in Figure 18, almost identical T_v profiles are calculated, with CVDV2 being slightly lower in the post-shock region. Since there is a significant difference in the T_v profiles for CVDV1 and CVDV2 models at 8.915 km/sec, it is surprising to see almost identical T_v profiles for CVDV1 and CVDV2 models at 9.326 km/sec. This difference can be explained by analyzing the CVDV2 model which adds a term to the relaxation time calculation. The added term is based on the inverse of the number density of the molecular species being

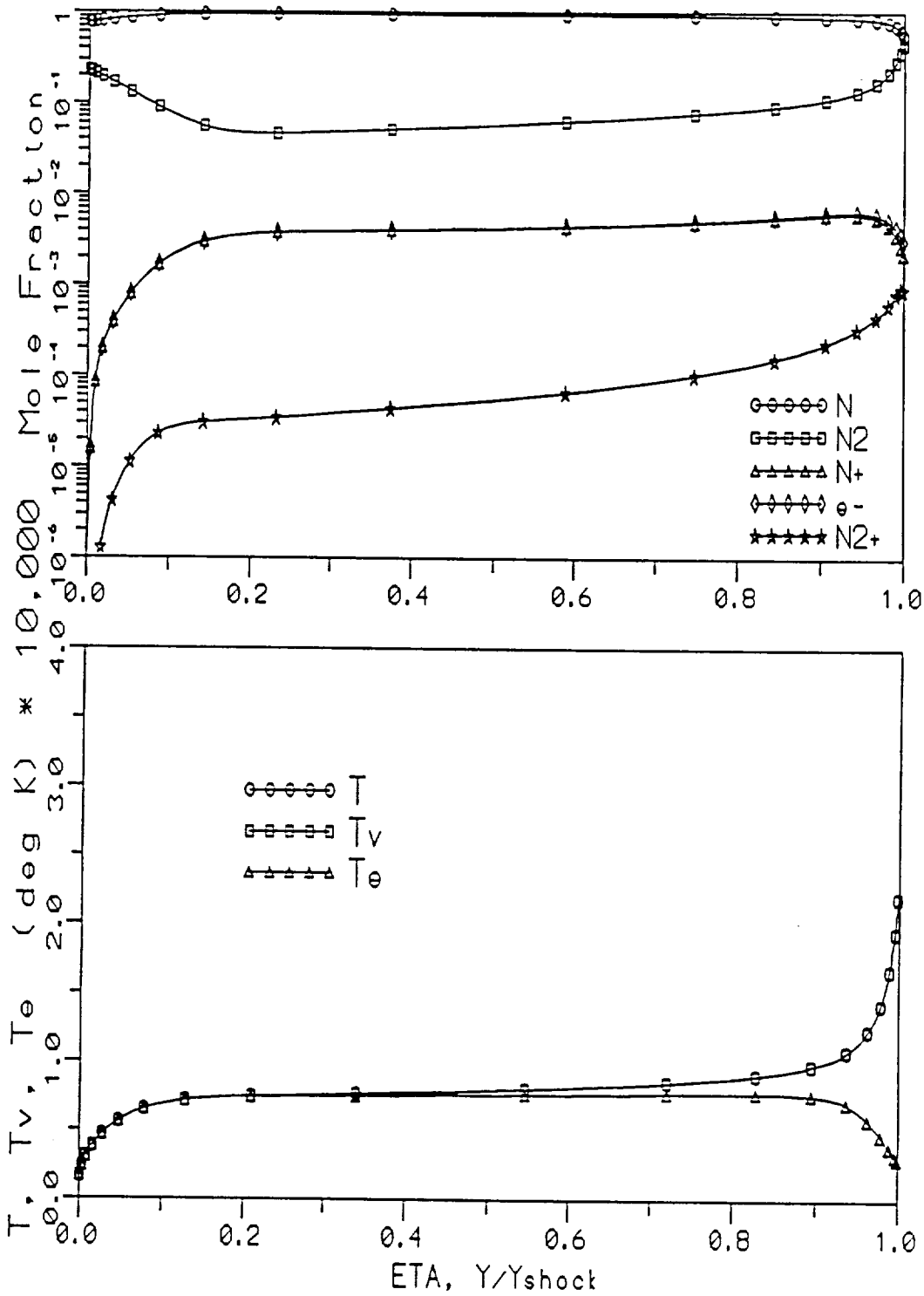

Figure 11: Uncoupled QEEE/T_v=T Model at U_∞=9.326 km/sec
Yshock=11.73 cm

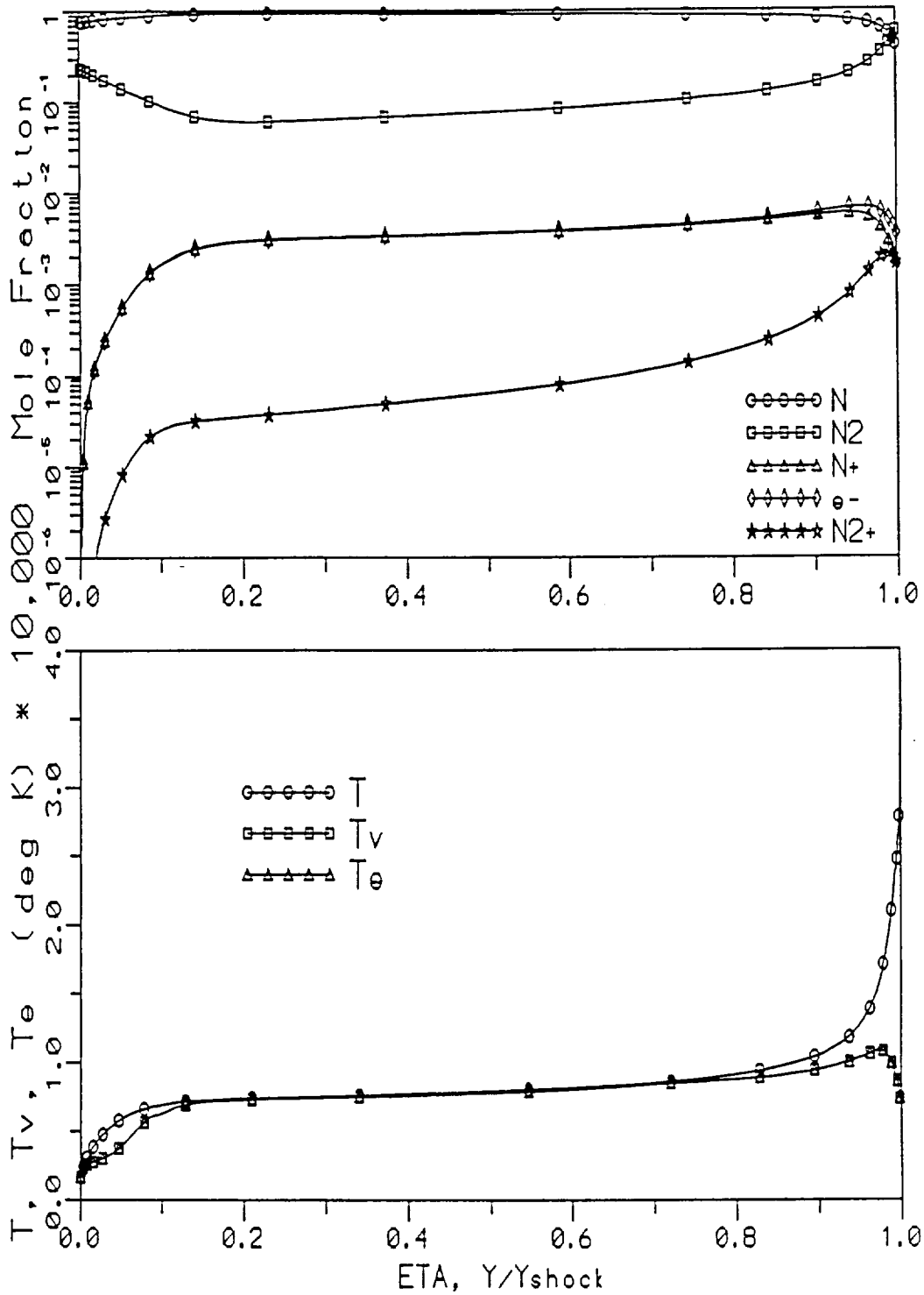

Figure 12: Coupled QEEE/CVDV1 Model at U_∞=9.326 km/sec
Yshock=11.98 cm

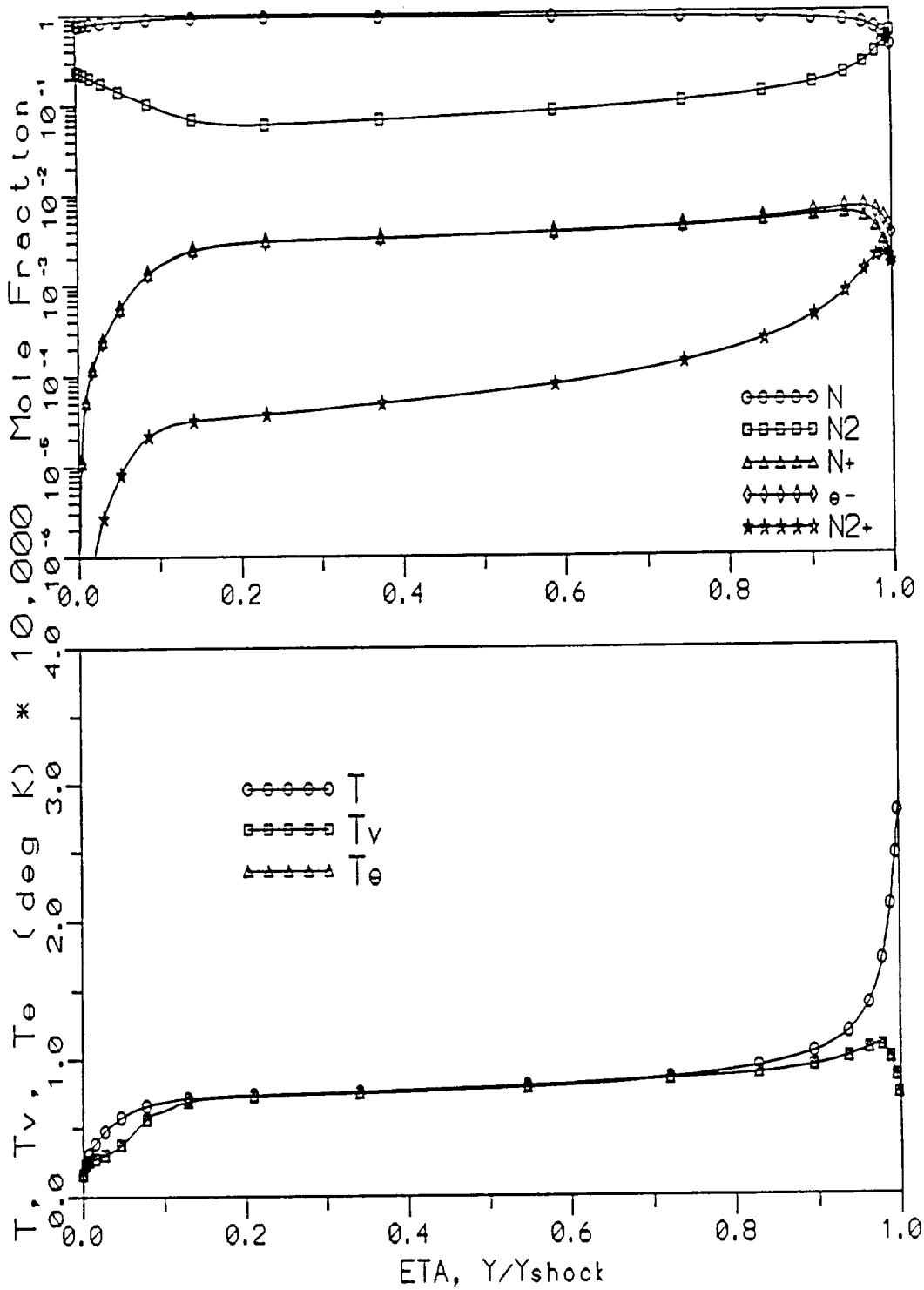

Figure 13: Coupled QEEE/CVDV2 Model at U_∞=9.326 km/sec
Yshock=12.01 cm

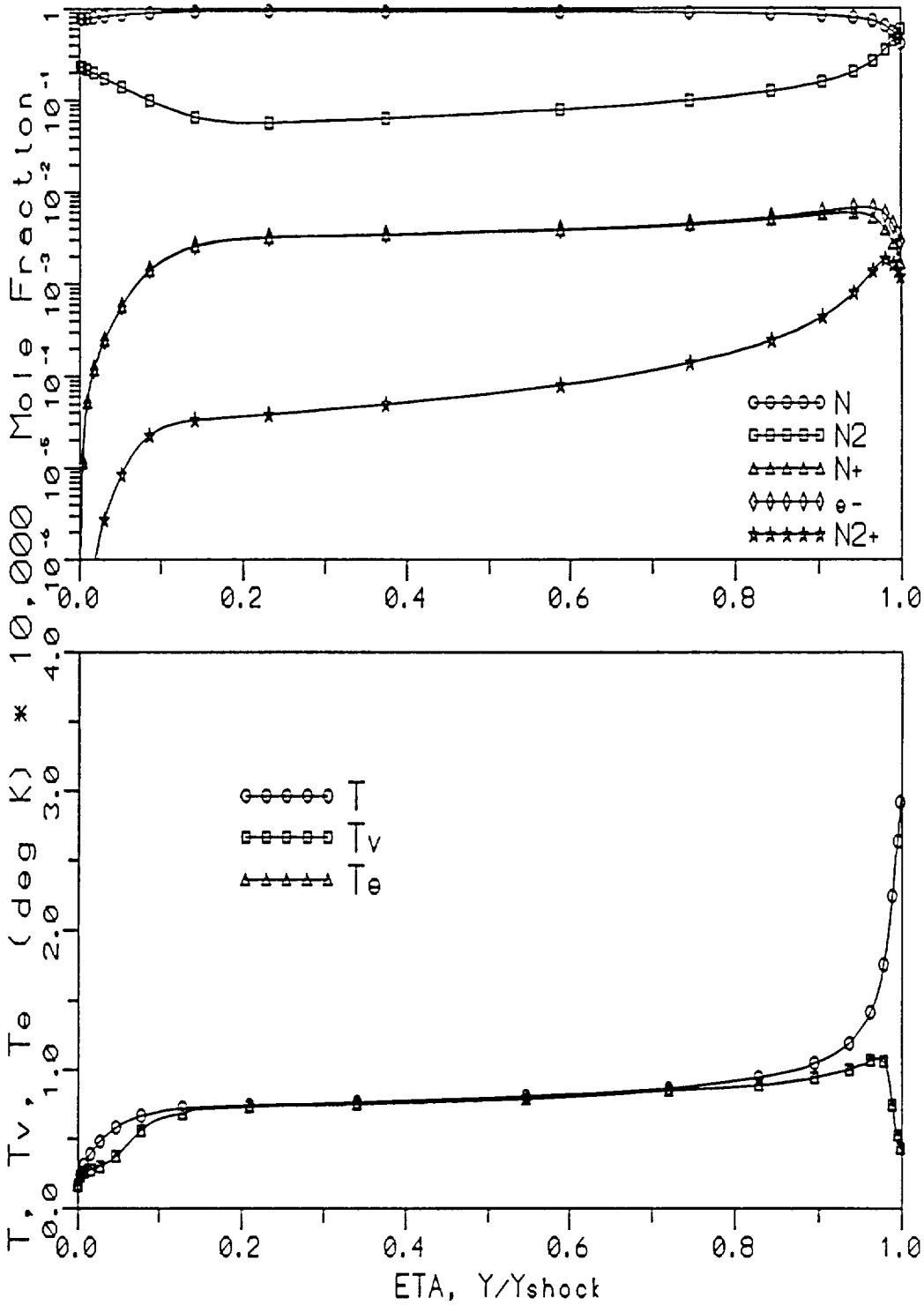

Figure 14: Coupled QEE/CVDV3 Model at U_∞=9.326 km/sec
Yshock=12.17 cm

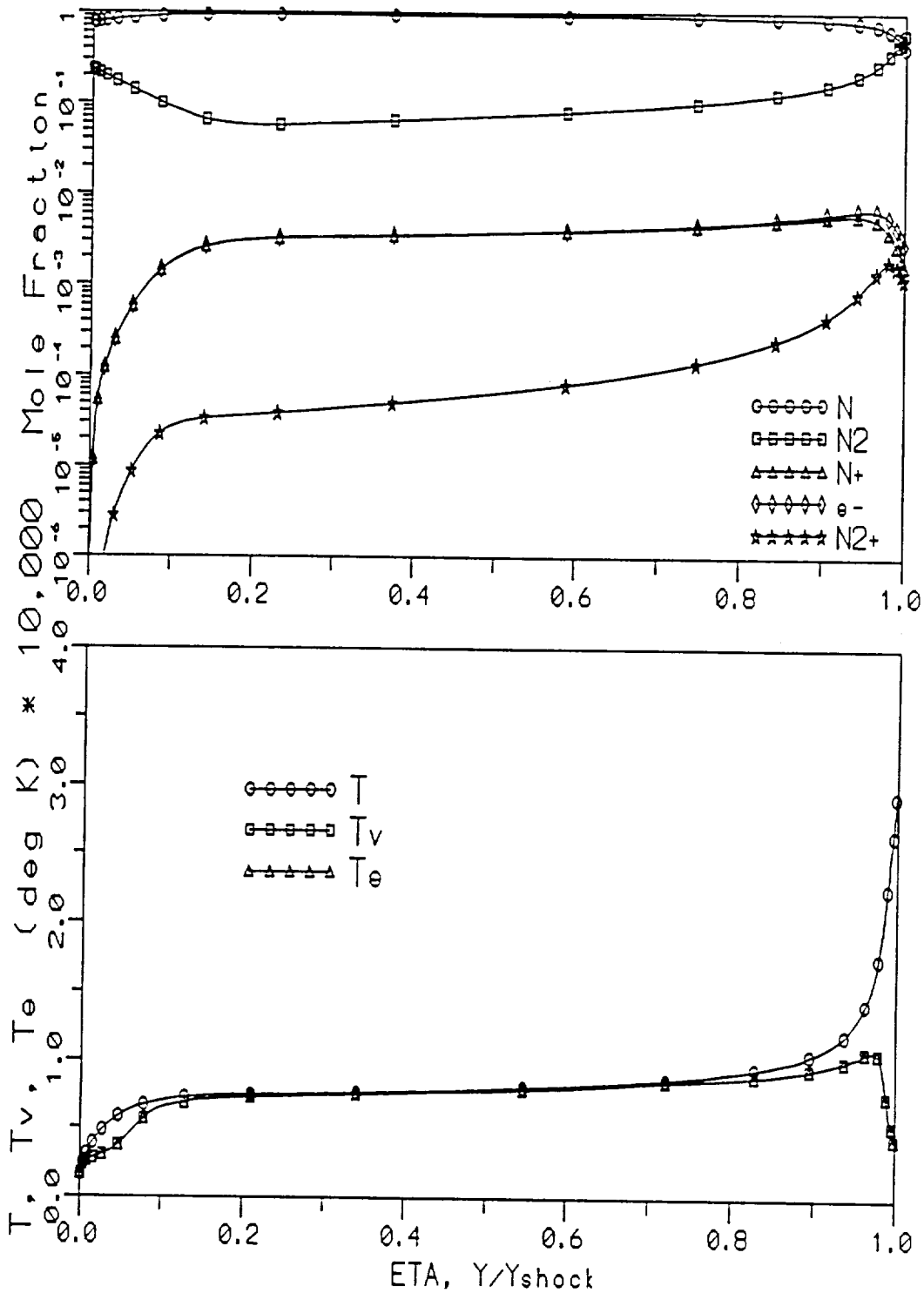

Figure 15: Coupled QEEE/CVDV3 Model at U_∞=9.326 km/sec
Yshock=12.19 cm

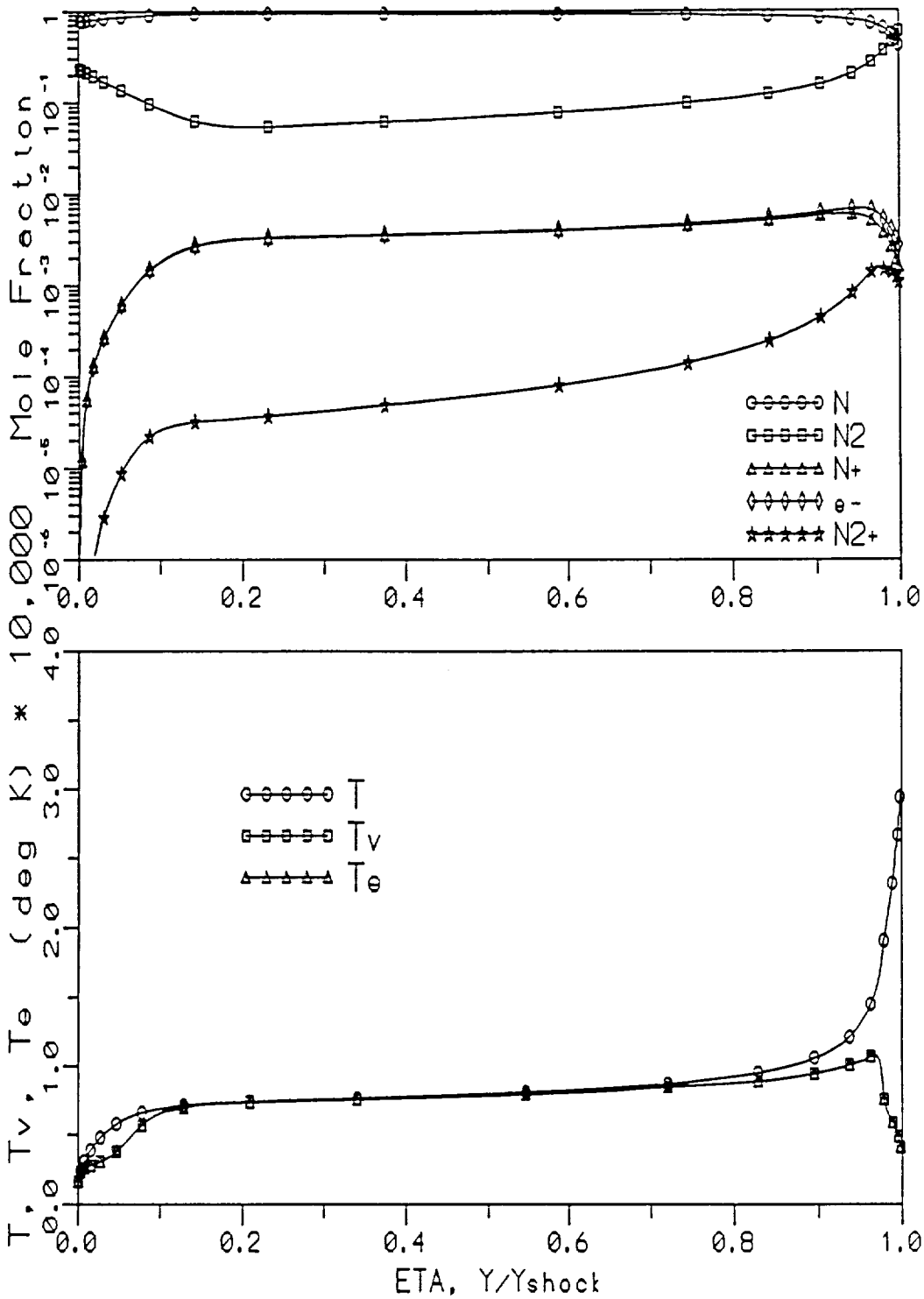

Figure 16: Coupled QEEE/CVDV4 Model at U_∞=9.326 km/sec
Yshock=12.24 cm

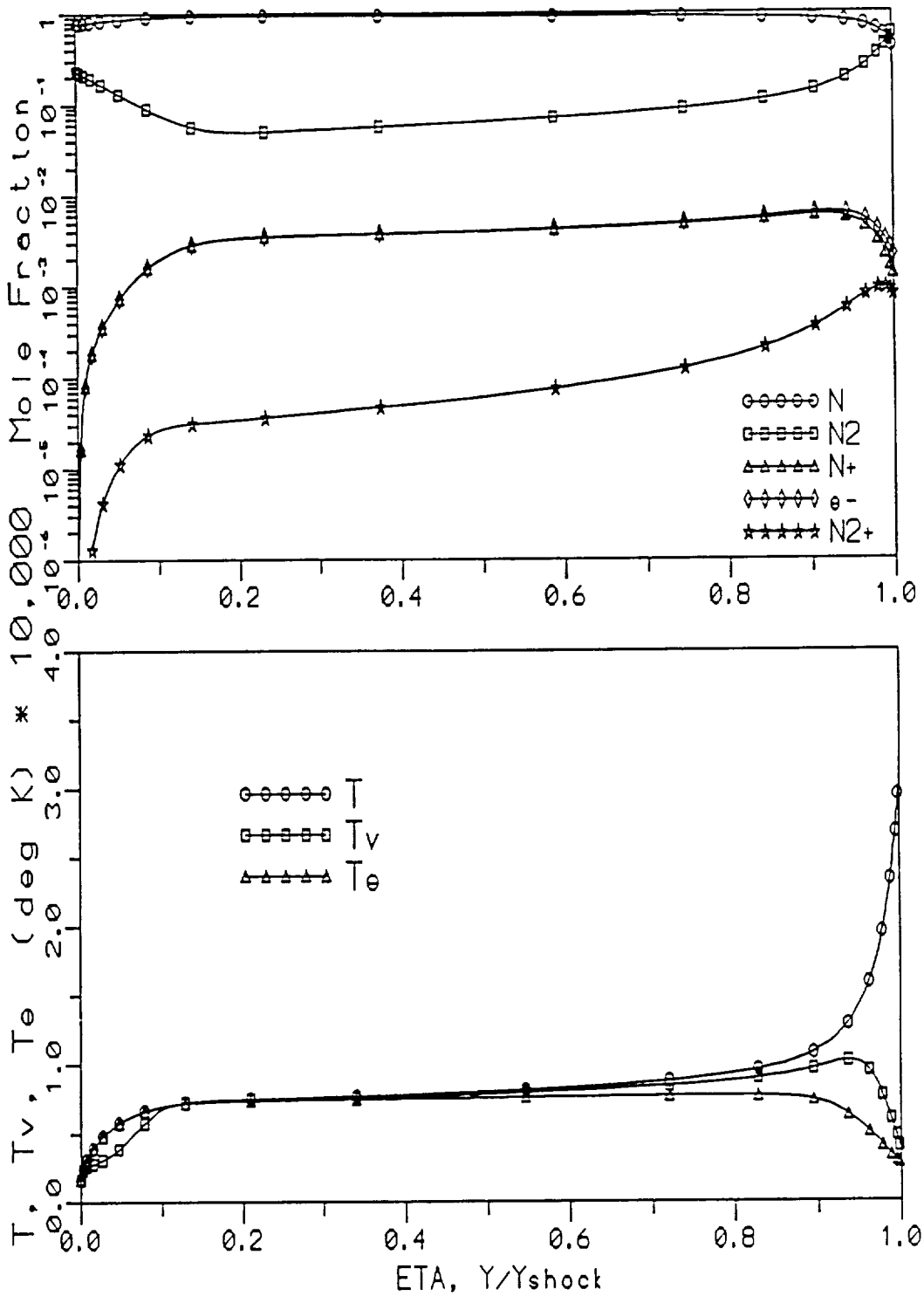

Figure 17: Uncoupled QEEE/CVDV3 Model at U_∞=9.326 km/sec
Yshock=12.44 cm

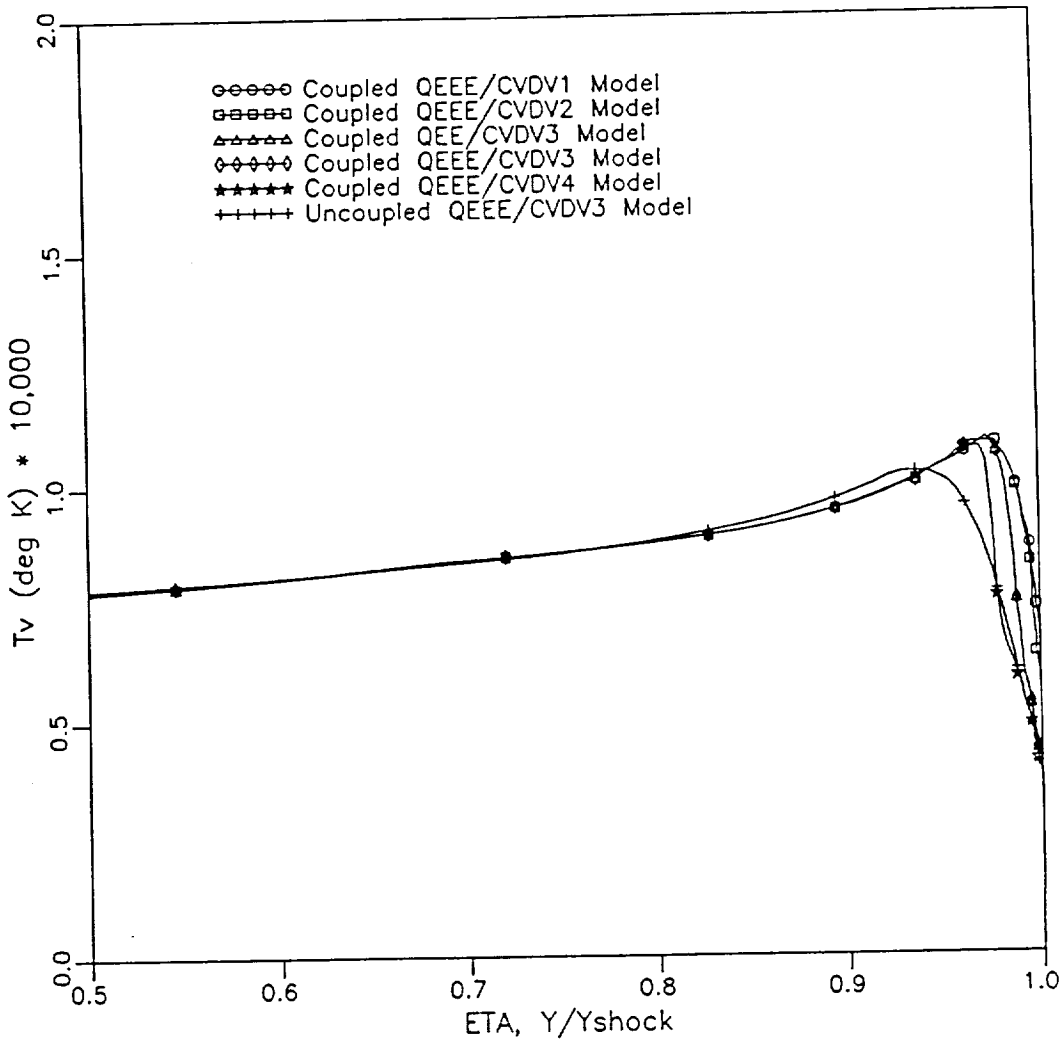

Figure 18: Comparison of CVDV Models at U_∞=9.326 km/sec

considered. Due to a lower altitude and thus a higher freestream density corresponding to the 9.326 km/sec case, the term added to the relaxation time becomes proportionally smaller because of the increased number density of the molecular species. Thus, the significance of the term added to the relaxation time in the CVDV2 model diminishes at higher freestream densities, as shown in Figure 18.

As seen earlier at 8.915 km/sec, the CVDV3 model predicts a slower relaxation

process than the CVDV1 or CVDV2 models. However, at 9.326 km/sec the choice of electron temperature model does not noticeably alter the T_v profile, which can be attributed to the fact that at 9.326 km/sec the QEE and QEEE electron energy models predict more similar T_e profiles than at 8.915 km/sec. Although, when comparing the uncoupled CVDV3 results with the coupled CVDV3 results, it is concluded the effects of the T_v-T_e coupling term are still important.

Finally, when studying the coupled QEEE/CVDV4 model, one would not expect the results to differ significantly from the coupled QEEE/CVDV3 model since the higher freestream density makes the Park modification to the relaxation time less significant. While to an extent this expectation is true, once dissociation occurs the molecular number density becomes lower and the extra term does become significant. This delayed phenomenon is shown in Figure 18 where the T_v profile predicted by the coupled QEEE/CVDV4 model deviates initially from the T_v profile predicted by the coupled QEEE/CVDV3 model.

12 km/sec, 80 km

AOTV flowfields at velocities of 12 km/sec and altitudes of 80 km are characterized by a greater degree of dissociation and, consequently, effects of vibrational nonequilibrium will be less substantial. Presented in Figures 19-26 are temperature and species profiles along the stagnation streamline predicted by the various temperature models given in Table 2. Again, results of the QEE and QEEE two temperature models are presented in Figures 19 and 20 for comparison to the results of various three temperature models. Similar to results at slower speeds, the species concentrations predicted by the coupled QEEE/CVDV1 model presented in Figure 21

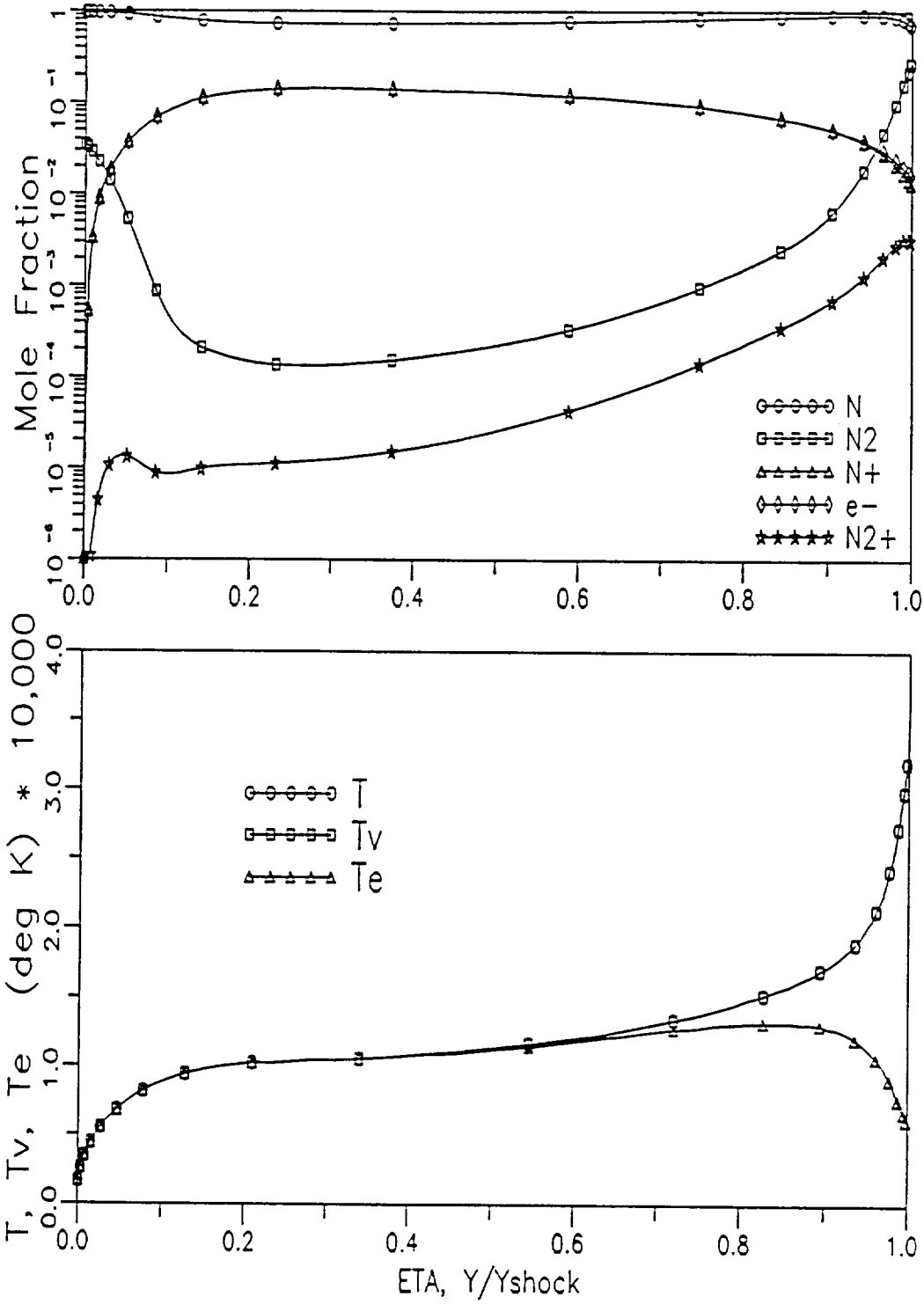

Figure 19: Uncoupled QEE/T_v=T Model at U_∞=12 km/sec
Yshock=11.39 cm

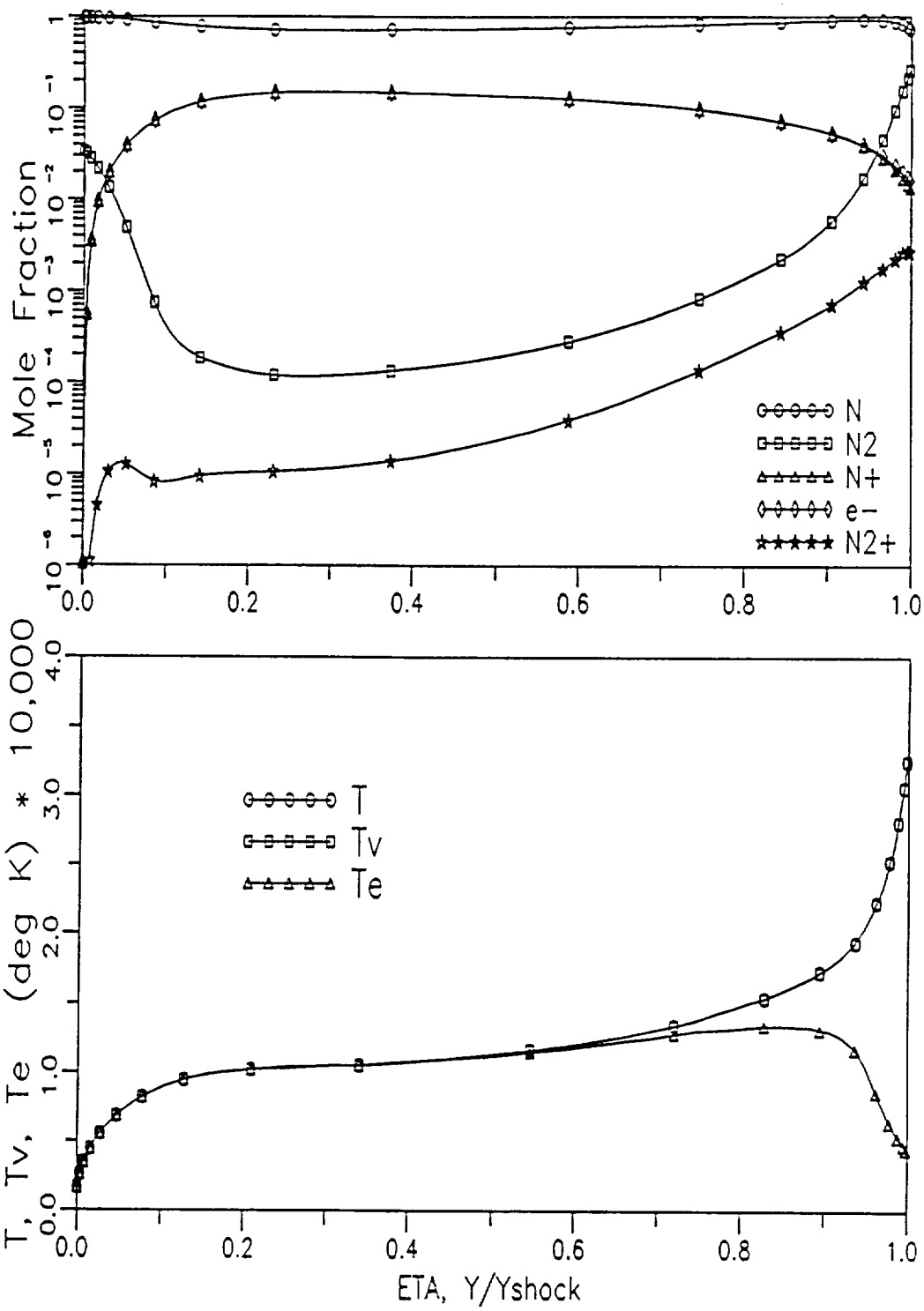

Figure 20: Uncoupled QEEE/T_v=T Model at U_∞=12 km/sec
Yshock=11.48 cm

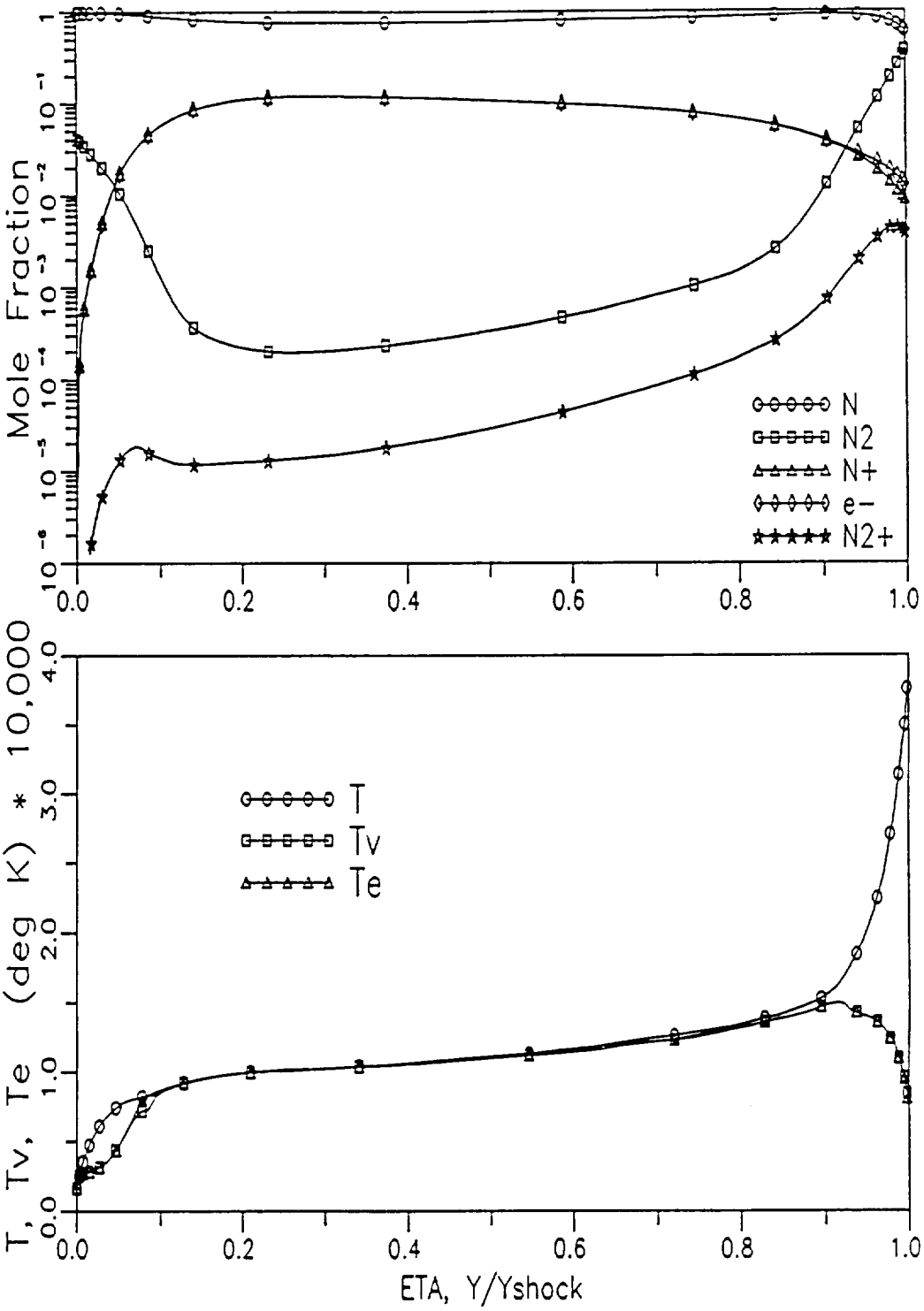

Figure 21: Coupled QEEE/CVDV1 Model at $U_\infty = 12$ km/sec
Yshock=11.29 cm

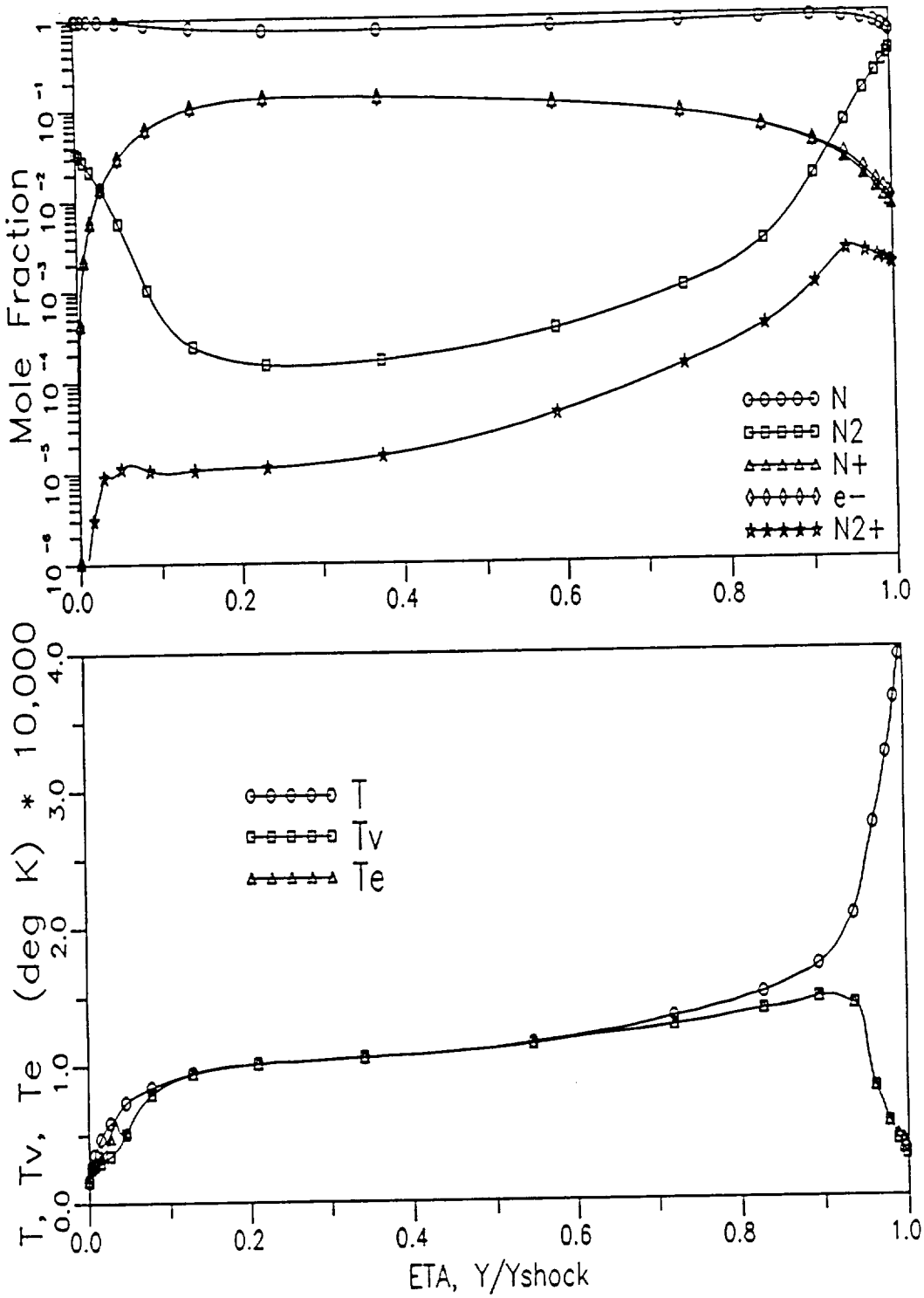

Figure 22: Coupled QEEE/CVDV2 Model at $U_\infty = 12$ km/sec
Yshock=11.78 cm

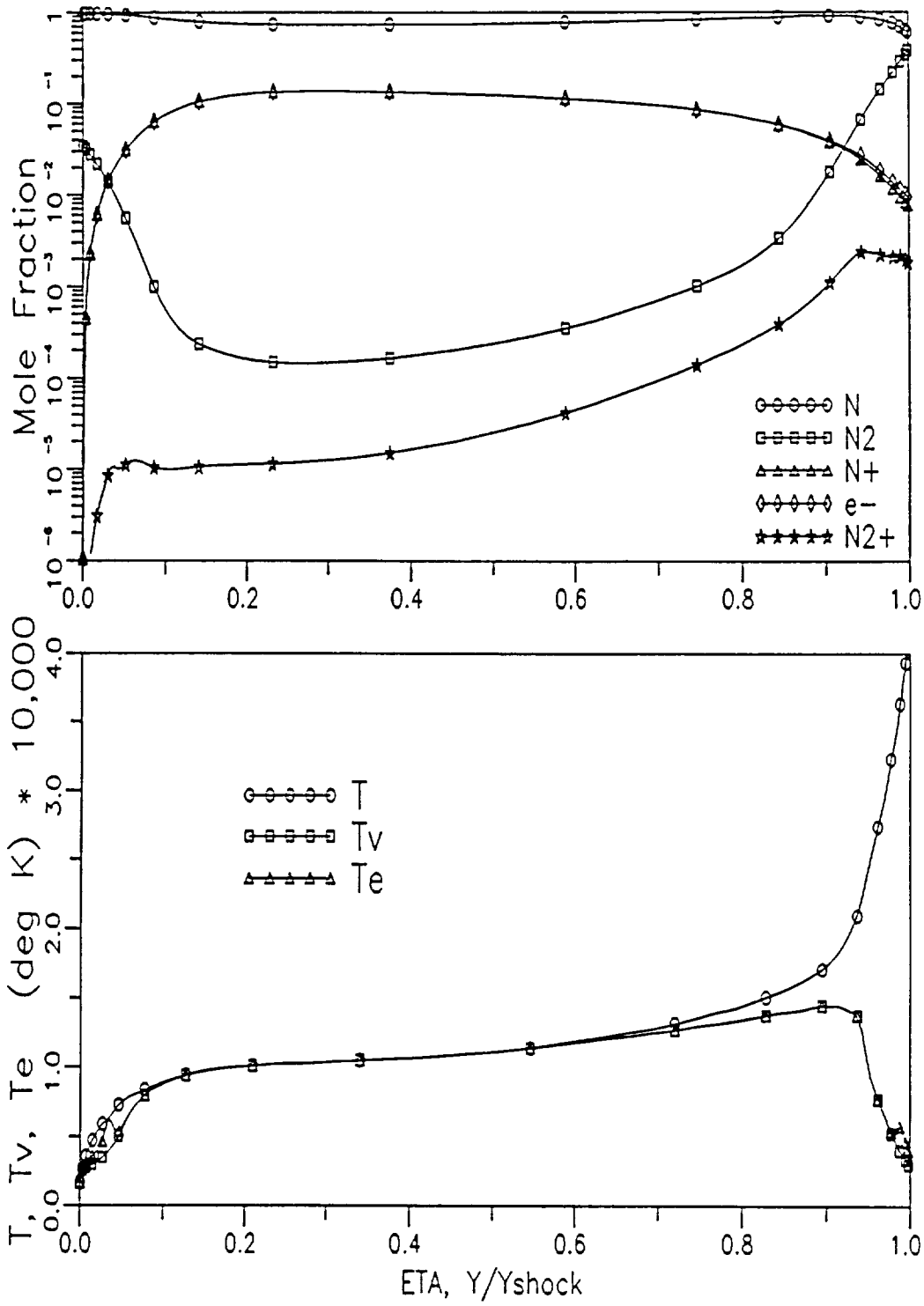

Figure 23: Coupled QEE/CVDV3 Model at $U_\infty = 12$ km/sec
Yshock = 11.75 cm

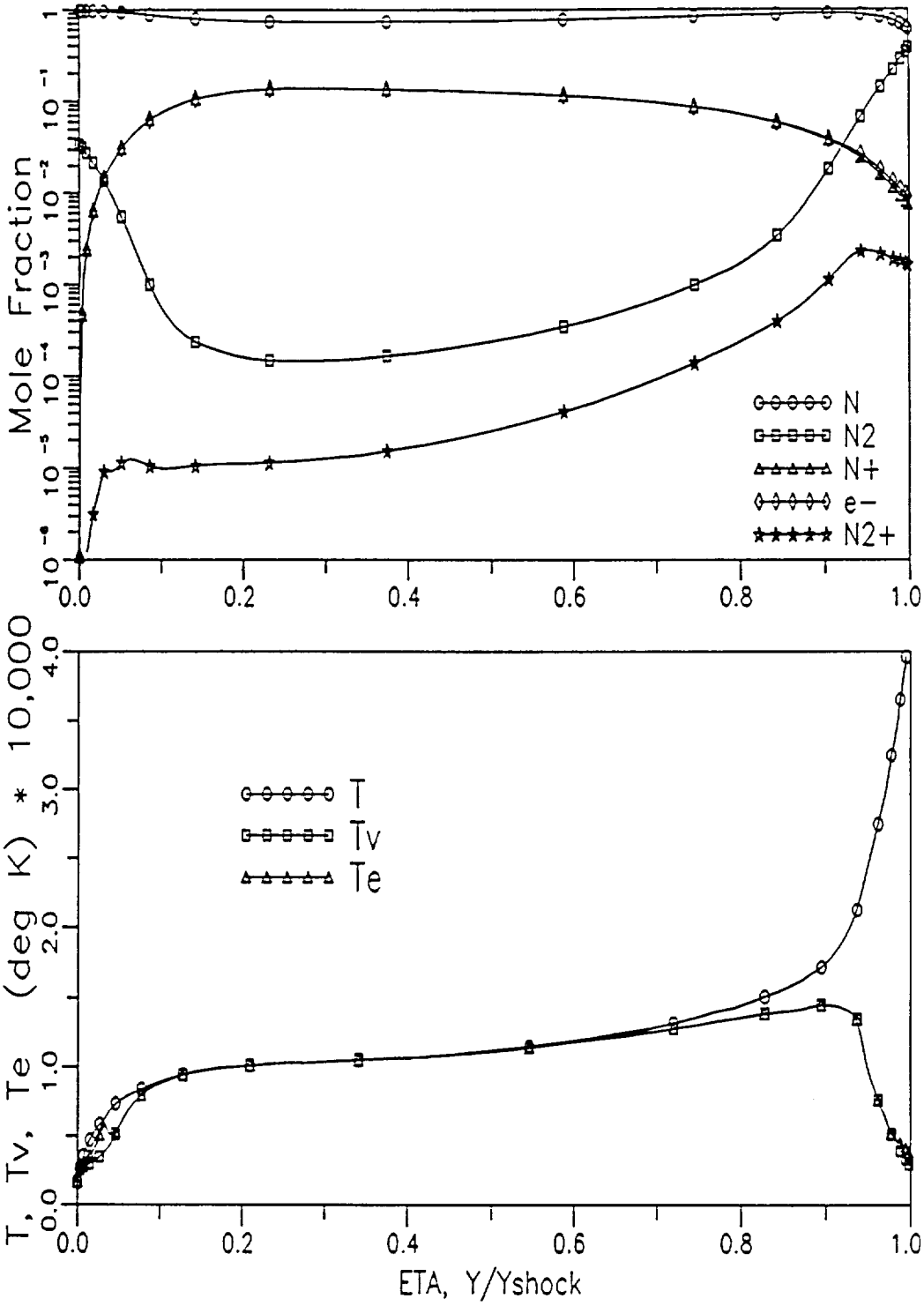

Figure 24: Coupled QEEE/CVDV3 Model at $U_\infty = 12$ km/sec
Yshock=11.80 cm

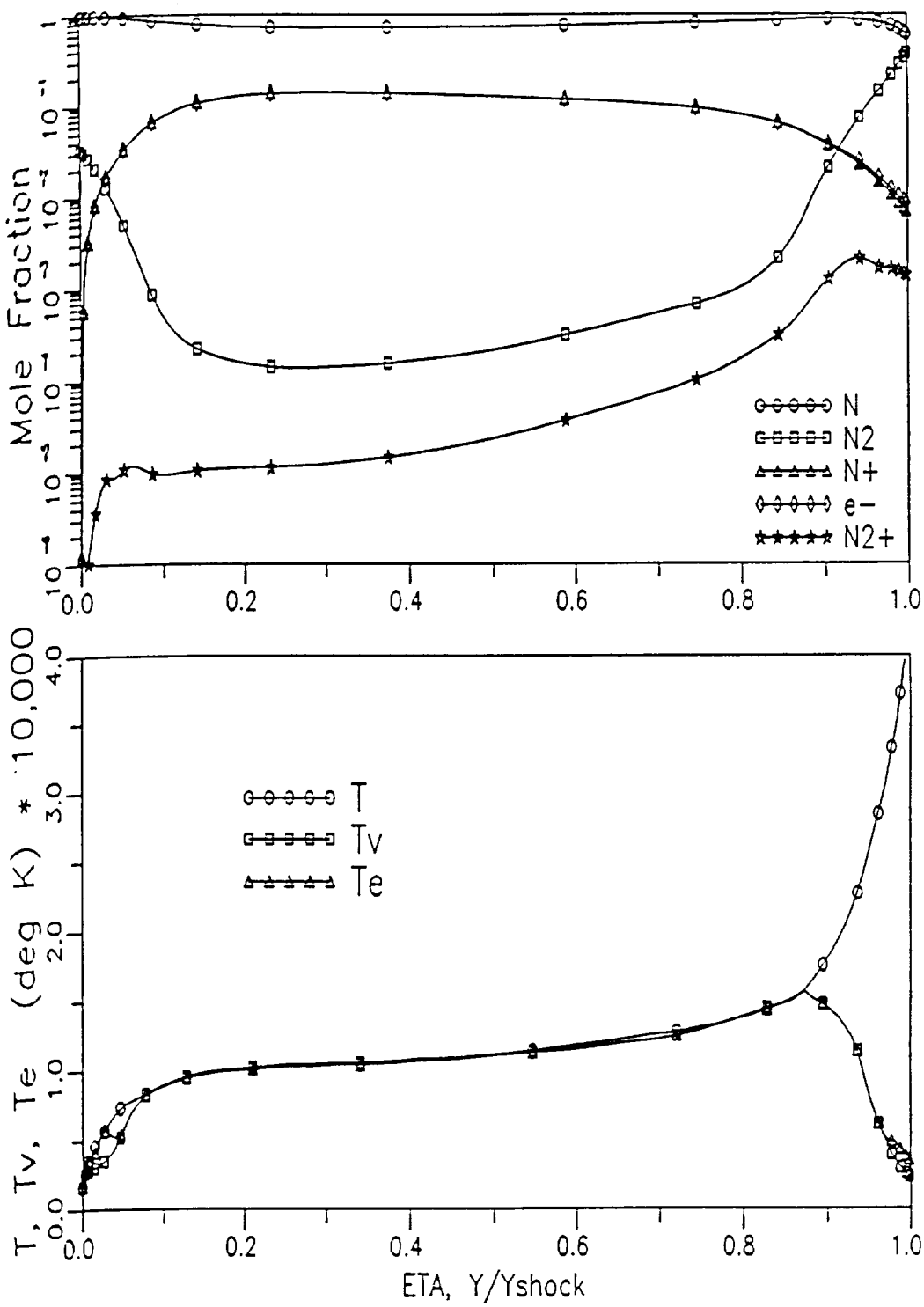

Figure 25: Coupled QEEE/CVDV4 Model at $U_\infty = 12$ km/sec
Yshock = 11.73 cm

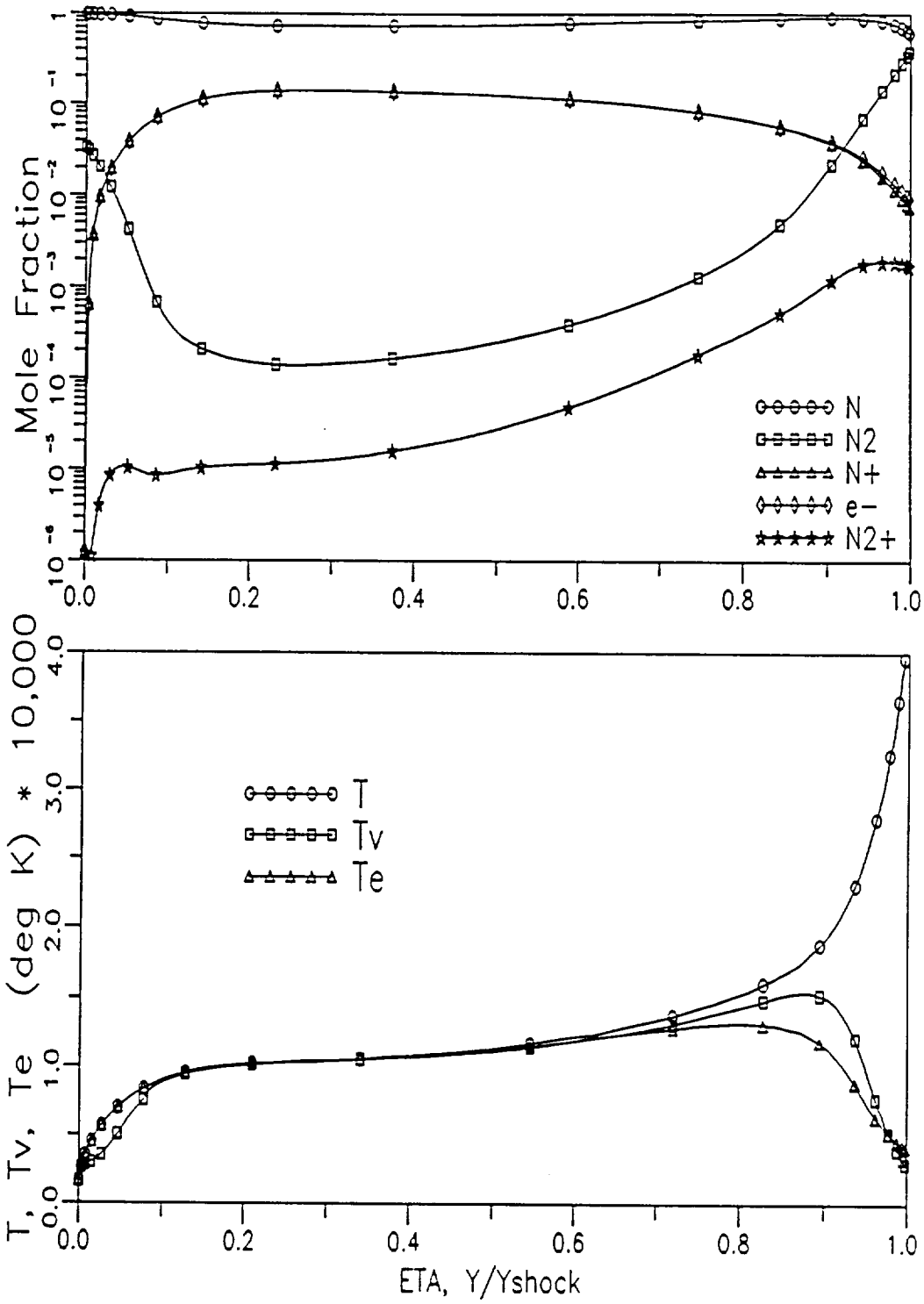

Figure 26: Uncoupled QEEE/CVDV3 Model at $U_\infty = 12$ km/sec
Yshock = 11.98 cm

show slower dissociation rates as compared with two temperature model results in Figures 19 and 20. However, due to electron-vibrational coupling, the T_e in the CVDV1 case is higher which leads to a faster ionization rate than in the two temperature case. Further, it is noted that near the wall boundary the deficit in vibrational temperature as compared to the heavy particle temperature is more pronounced than at speeds of 8.915 and 9.326 km/sec. Since the T_v decrease is created by low energy molecules diffusing away from the cold wall, the larger deficit must be due to a greater diffusion rate of molecules away from the wall than in the lower speed case.

A comparison of T_v profiles for each of the CVDV models at 12 km/sec is presented in Figure 27. Near the shock front the effects of the Park modification to the relaxation time in the CVDV2 and CVDV4 models are dominant in that the T_v gradient near the shock is significantly decreased by the added term in the CVDV2 model and the CVDV4 model slows down the vibrational relaxation process even more. This behavior is consistent since the CVDV4 model effectively increases the magnitude of the Park modification in the CVDV2 model. Further, it should be noted that the T_v profiles predicted by the coupled CVDV3 models are similar to the results of CVDV2 model. While at the lower speeds of 8.915 and 9.326 km/sec, the modifications of the CVDV3 model to account for the diffusive nature of vibrational relaxation noticeably slowed the vibrational equilibration process; at higher speeds, the heavy particle temperature at the shock is greater, forcing the A coefficient in the CVDV3 model closer to unity.

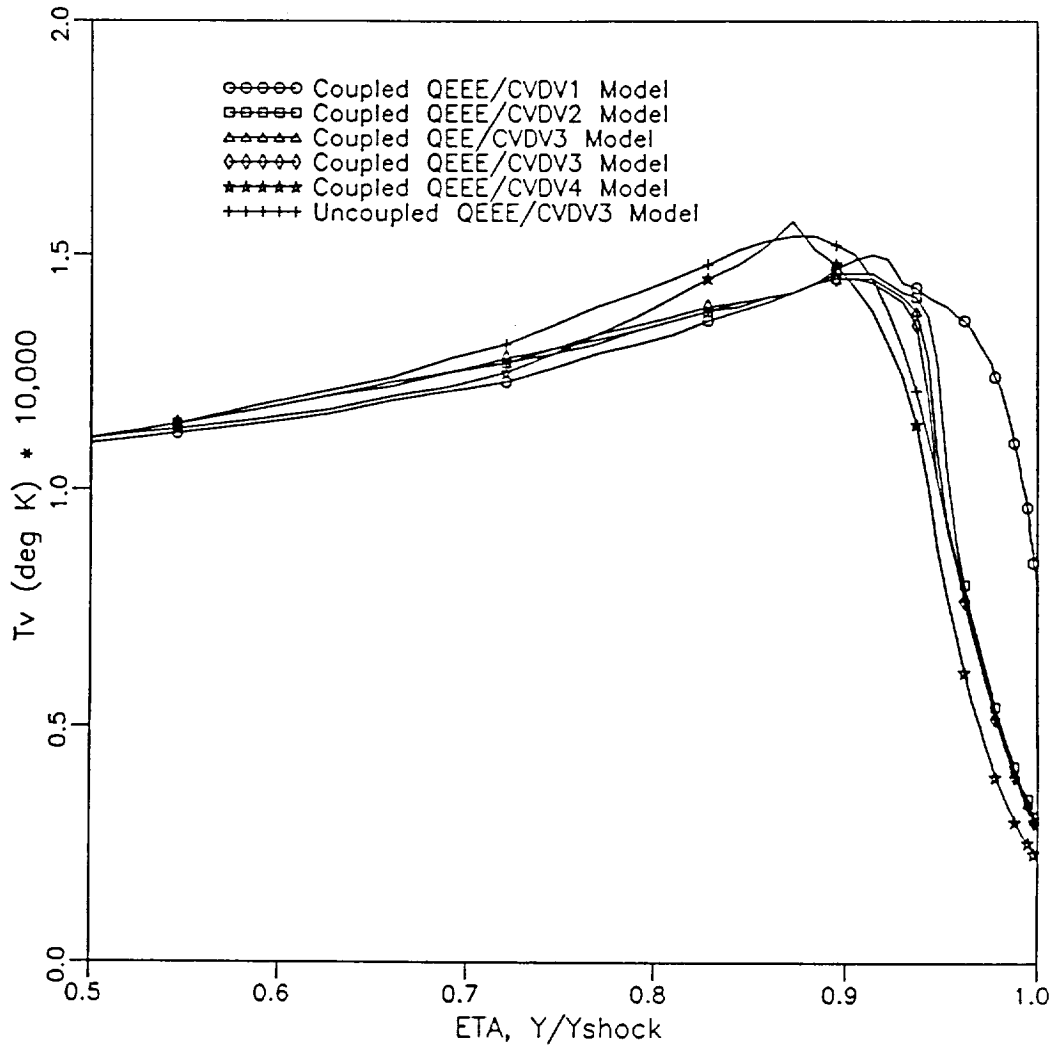

Figure 27: Comparison of CVDV Models at $U_\infty = 12$ km/sec

Comparing the uncoupled and coupled solutions to the CVDV3 models in Figure 27, it is apparent that T_v-T_e coupling has an effect on the T_v profiles. However, examination of Figures 24 and 26 reveals that the primary effect of coupling is to increase the T_e values. Further, very few differences in T_v and T_e are seen when changing from the QEE to the QEEE electron energy models since at these conditions electron-electronic energy is starting to be dominated by ionization chemistry and free

electron effects.

14 and 16 km/sec, 80 km

The AOTV flowfield for freestream velocities of 14 and 16 km/sec at an altitude of 80 km is characterized by thermal nonequilibrium, radiative heat transfer, and almost complete dissociation. To study the vibrational effects at these higher speeds, which should be reduced due to the nearly complete dissociation of diatomic nitrogen soon after the shock, computer simulations were conducted for a QEEE two temperature model and a coupled QEEE/CVDV3 three temperature model. These temperature models were chosen because currently it is believed that the two models are the most complete of those considered.

Unlike the results presented for velocities of 8.915, 9.326, and 12 km/sec, the results at 14 and 16 km/sec where radiative effects should be minimal, the results at 14 and 16 km/sec also include radiative transfer and radiative gas dynamic coupling in the energy in the energy model. The temperature and species concentration results predicted by the QEEE two temperature model at 14 and 16 km/sec are given in Figures 28 and 30, and the coupled QEEE/CVDV3 three temperature model results for 14 and 16 km/sec are presented on Figures 29 and 31.

When comparing the two temperature and three temperature results at 14 km/sec in Figures 28 and 29, it appears that the QEEE electron temperature model and the CVDV3 vibrational energy model predict nearly identical profiles for T_e. Similar effects are seen in the results at 16 km/sec in Figures 30 and 31. It is concluded that a single temperature for electron energy and vibrational energy would accurately predict the thermal nonequilibrium effects at 14 and 16 km/sec. Further, as shown on Figures

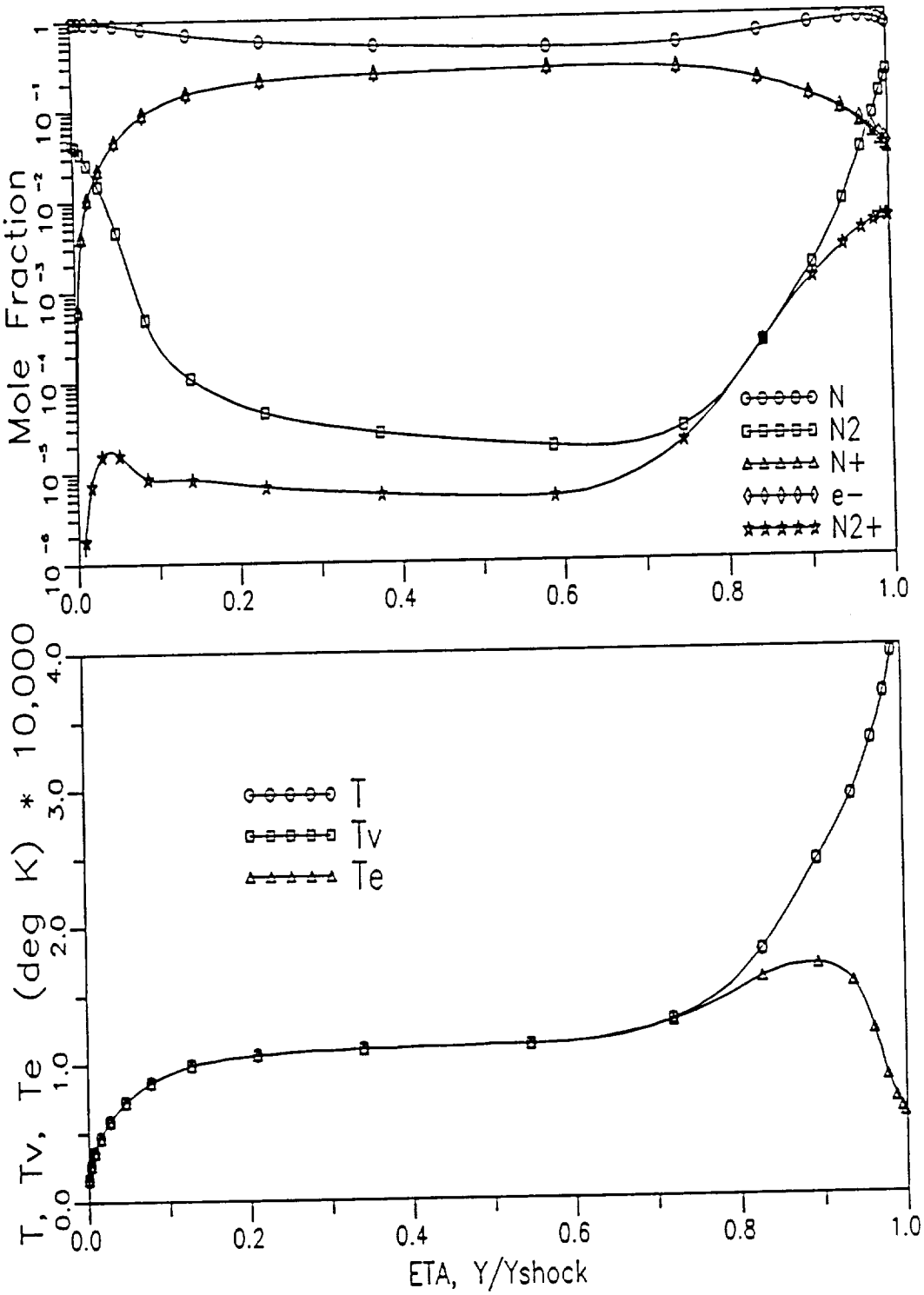

Figure 28: Uncoupled QEEE/T_v=T Model at U_∞=14 km/sec
Yshock=9.09 cm

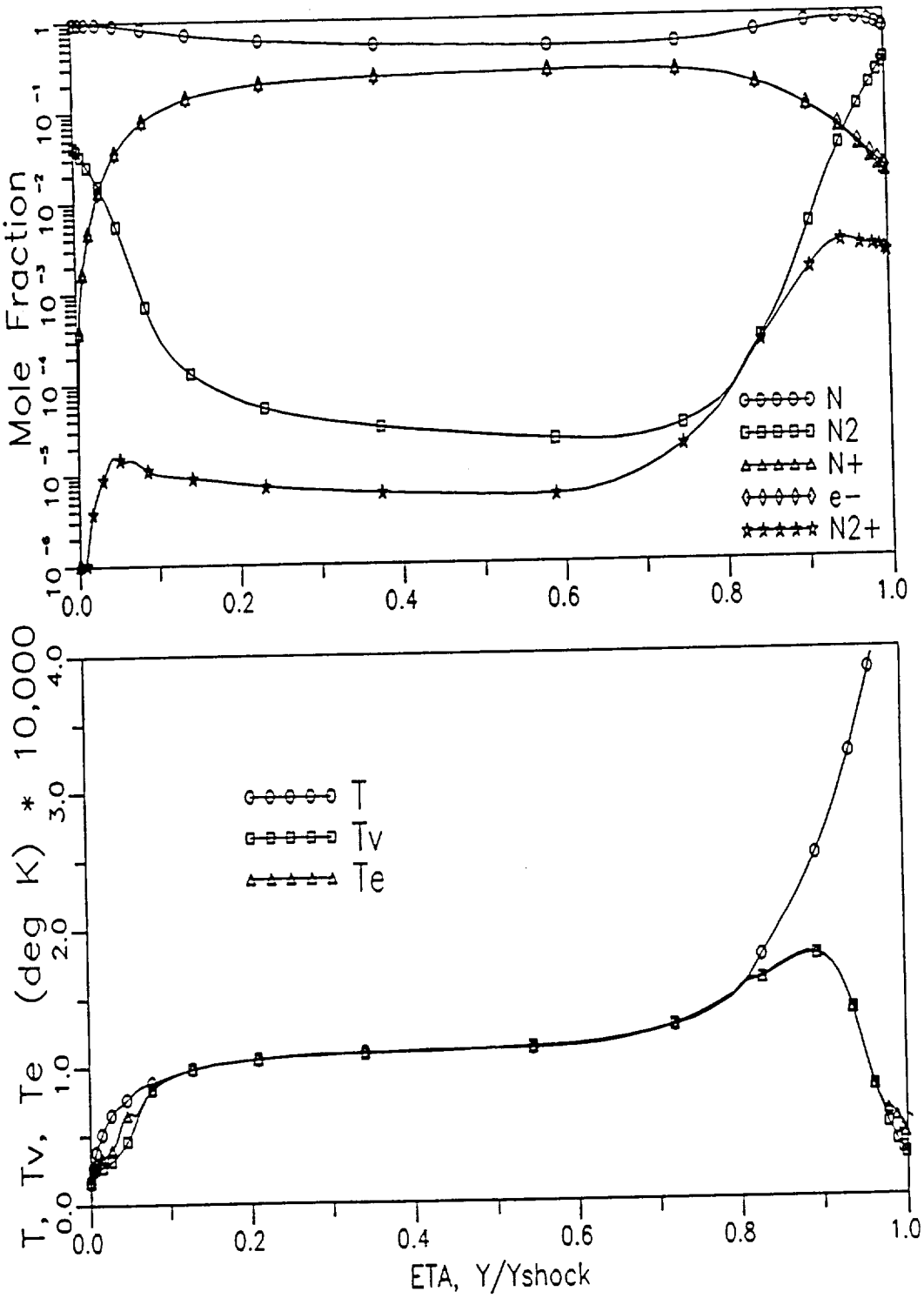

Figure 29: Coupled QEEE/CVDV3 Model at U_∞=14 km/sec
Yshock=9.25 cm

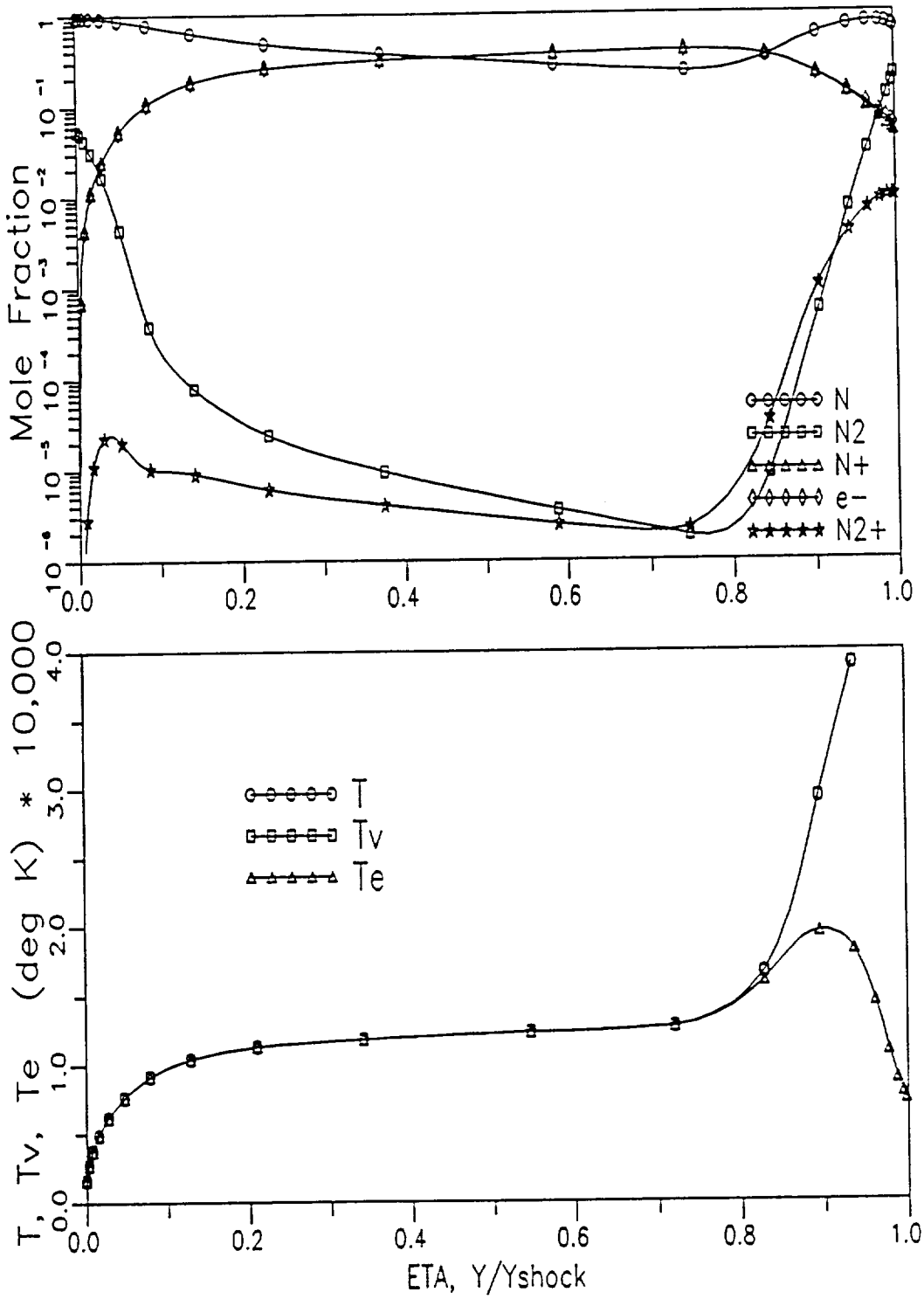

Figure 30: Uncoupled QEEE/T_v=T Model at U_∞=16 km/sec
Yshock=7.54 cm

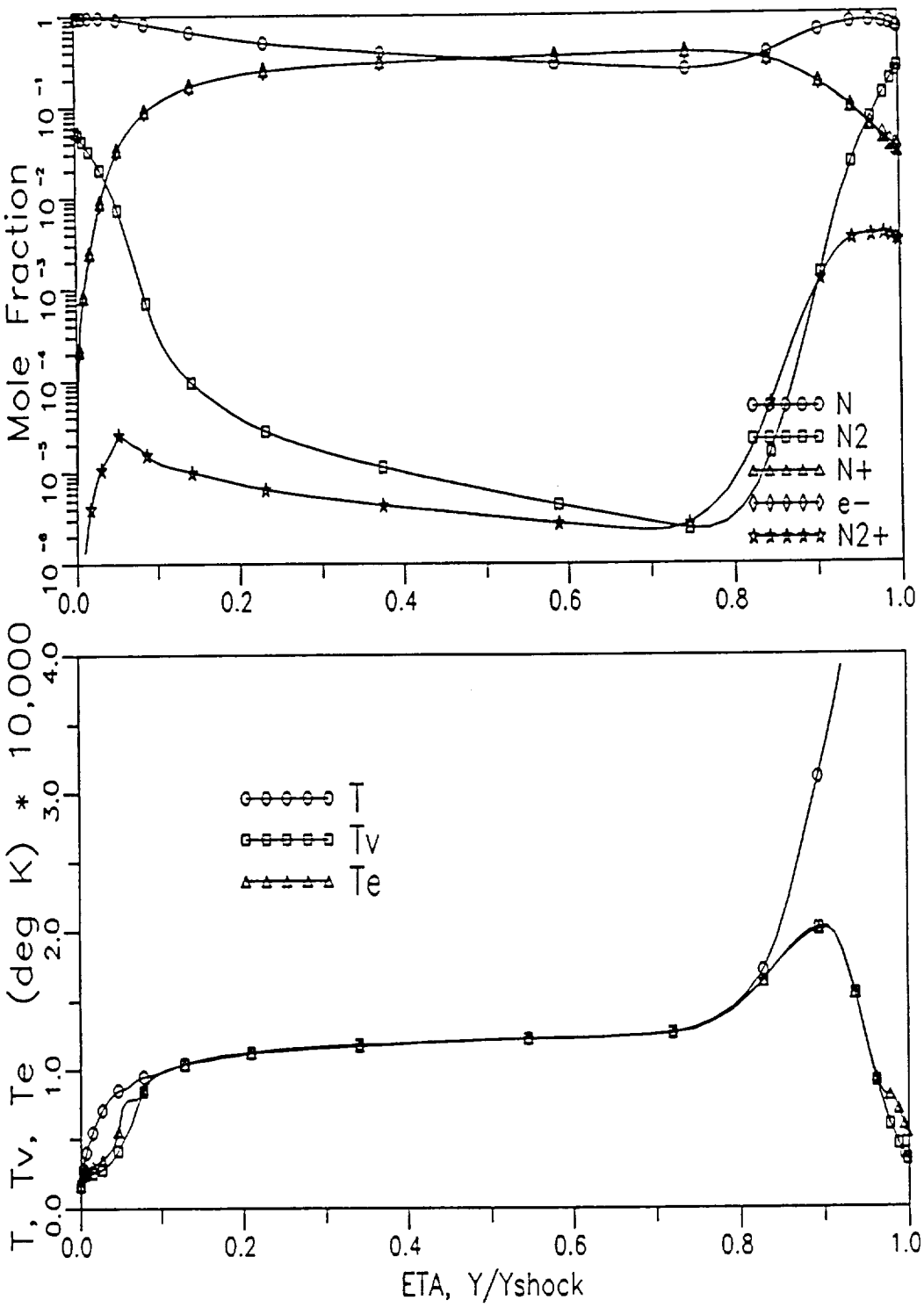

Figure 31: Couple QEEE/CVDV3 Model at $U_\infty = 16$ km/sec
Yshock=7.71 cm

29 and 31 at temperatures less than approximately 7,500° K the T_e profile deviates from the T_v profile. This effect also occurs to a lesser degree at 12 km/sec and can be seen in Figures 22-25. Examination indicates that the coefficient A_e on the vibrational-electron coupling term is responsible for this effect. Since A_e is proportional to the difference of T_e at the shock and local T_v, A_e approaches zero as the local value of T_v approaches the shock value of T_e. As A_e approaches zero, the T_v-T_e coupling becomes negligible, and T_e tends towards an uncoupled solution as seen in Figures 29 and 31. This behavior indicates that the form of A_e should be examined in more detail and perhaps improved.

Finally, the effects of the two temperature verses three temperature models on heat transfer at the wall are presented in Table 3. The heat transfer includes radiative and convective heating.

U_∞ km/sec	2 Temperature Model Q_{wall} W/cm^2	3 Temperature Model Q_{wall} W/cm^2	% Difference
14.0	-148.30	-143.03	3.44
16.0	-341.12	-325.89	4.57

Table 3: Heat Transfer at Wall Boundary

Negative heat transfer implies absorption by the wall. From the results at 14 and 16 km/sec it appears that a three temperature models predicts slightly lower heating at the wall; however, a more in depth study should be made before any real conclusions are

drawn concerning the effects of vibrational nonequilibrium on radiative heat transfer.

CONCLUSIONS

Specific conclusions relating to the various vibrational relaxation models have been drawn from the current research of AOTV flight regimes. Results at each of the different velocities ranging from 8.915 to 16 km/sec have yielded insights pertinent to that particular condition.

At 8.915 km/sec, vibrational-electron coupling dominates the electron energy equation, the effects of the Park modification to the relaxation time are strongest near the shock, and modifications accounting for the diffusive nature become significant as T_v approaches equilibrium temperature. For the 9.326 km/sec case, which is also at a higher freestream density, the Park modification to the relaxation time becomes insignificant, using a smaller coefficient in the expression for minimum cross section makes the Park modification to relaxation time significant, and in each model vibrational relaxation is faster than at 8.915 km/sec due to the higher freestream density. The results at 12 km/sec implied that the Park modification for the diffusive nature of vibrational relaxation had very little effect on the T_v profile; and unlike the 9.326 km/sec case, the Park modification to the relaxation time predicted a slower equilibration of T_v near the shock. At 14 and 16 km/sec, T_v and T_e became uncoupled when T_v approached the shock value of T_e due to the nature of the Park like modification of the vibrational-electron coupling term.

Finally, in every three temperature models the vibrational temperature deviates

from the heavy particle temperature near the wall, long after thermal equilibrium is reached. This deviation is caused by a low temperature and high molecular concentration gradient at the wall, forcing the diffusion of molecules having low vibrational energy away from the wall.

REFERENCES

[1]Lee, J. H., "Basic Governing Equations for the Flight Regimes of Aeroassisted Orbital Transfer Vehicles," AIAA Paper 84-1729, June 1984.

[2]Park, C., "Radiation Enhancement by Nonequilibrium in Earth's Atmosphere," AIAA Paper 83-0410, January 1983.

[3]Menees, G. P., Park, C., and Wilson, J. F., "Design and Performance Analysis of a Conical-Aerobrake Orbital-Transfer Vehicle Concept," AIAA Paper 84-0410, January 1984.

[4]Treanor, C. E. and Marrone, P. V., "Effect of Dissociation on the Rate of Vibrational Relaxation," *Physics of Fluids*, Vol.5, September 1962, pp. 1022-1026.

[5]Park, C., "Problems of Rate Chemistry in the Flight Regimes of Aeroassisted Orbital Transfer Vehicles," in *Progress in Astronautics and Aeronautics , Vol. 96, Thermal Design of Aeroassisted Orbital Transfer Vehicles*, H. F. Nelson, ed., AIAA, NY, 1985, pp. 511-537.

[6]Park, C., "Assessment of a Two-Temperature Kinetic Model for Dissociating and Weakly Ionizing Nitrogen," *Journal of Thermophysics and Heat Transfer*, Vol. 2, January 1988, pp. 8-16.

[7]Vincenti, W. G. and Kruger, C. H., *Introduction to Physical Gas Dynamics*, Robert E. Krieger Publishing Co., Malabar, Florida, 1965.

[8]Millikan, R. C. and White, D. R., " Systematics of Vibrational Relaxation ,"*Journal of Chemical Physics*, Vol. 39, No. 12, December 1963, pp. 3209-3213.

[9]Lee, J. H., "Electron-Impact Vibrational Excitation Rates in the Flowfield of Aeroassisted Orbital Transfer Vehicles," *Thermophysical Aspects of Re-entry Flows*, eds. J. N. Moss and C. D. Scott, *Progress in Aeronautics and Astronautics*, Vol. 103, 1986, pp. 197-224.

[10]Candler, G. and Park, C., "The Computation of Radiation from Nonequilibrium Hypersonic Flows," AIAA Paper 88-2678, June 1988.
on Equations and Physical Models for Hypersonic Air Flows in Thermal and Chemical Nonequilibrium," NASA Technical Paper 2867, 1989.

[12]Marrone, P. V., "Inviscid Nonequilibrium Flow Behind Bow and Normal Shock Waves, Part I. General Analysis and Numerical Examples," Cornell, Buffalo, NY, Cornell Aeronautical Rept. QM-1626-A-12(I), May 1963.

[13]Park, C., "Assessment of Two-Temperature Kinetic Model for Ionizing Air," AIAA Paper 87-1574, June 1987.

[14]Carlson, L. A., Bobskill, G. J. and Greendyke, R. B., "Comparison of Vibration-Dissociation Coupling and Radiative Heat Transfer Models for AOTV/AFE Flowfields," *Journal of Thermophysics and Heat Transfer*, Vol. 4, No. 1, January 1990, pp. 16-26.

[15]Anderson, D. A., Tannehill, J. C. and Pletcher, R. H., *Computational Fluid Mechanics and Heat Transfer*, Hemisphere Publishing Corporation, New York, 1984, pp. 468-472.

[16]Davis, R. T., "Numerical Solution of the Hypersonic Viscous Shock-Layer Equations," *AIAA Journal*, Vol. 8, No. 5, May 1970, pp. 843-851.

[17]Moss, J. N., "Reacting Viscous-Shock-Layer Solutions with Multicomponent Diffusion and Mass Injection," NASA Technical Report R-411, June 1974.

[18]Thompson, R. A., "Comparison of Nonequilibrium Viscous Shock Layer Solutions with Windward Surface Shuttle Heating Data," AIAA Paper 87-1473, June 1987.

[19]Carlson, L. A. and Gally, T. A., "Nonequilibrium Chemical and Radiation Coupling Phenomena in AOTV Flowfields", AIAA Paper 91-0569, January 1991.

[20]Frieders, M. C. and Lewis, C. H., "Effects of Mass Transfer into Laminar and Turbulent Boundary Layers over Cones at Angle of Attack," VPI-AERO-031, March 1975.

APPENDIX I: TRANSPORT PROPERTIES

Thermal Conductivity

Assuming that the vibrational energy of each diatomic species is in a Boltzmann distribution with reference to T_v, the vibrational thermal conductivity is given by[1]

$$\eta_v = k \sum_{s=mol.} \frac{y_s}{\sum_{r=h.p.} [y_r \Delta_{sr}^{(1)}(T)] + y_e \Delta_{se}^{(1)}} \tag{47}$$

where $\Delta_{sr}^{(1)}(T)$ and $\Delta_{se}^{(1)}(T_e)$ can be expressed as

$$\Delta_{sr}^{(1)}(T) = \frac{8}{3}\left[\frac{2m_s m_r}{\pi kT(m_s+m_r)}\right]^{1/2} \pi \Omega_{sr}^{(1,1)}$$

$$\Delta_{se}^{(1)}(T_e) = \frac{8}{3}\left[\frac{2m_s m_e}{\pi kT_e(m_s+m_e)}\right]^{1/2} \pi \Omega_{se}^{(1,1)} \tag{48}$$

In the above expression, $\pi\Omega_{sr}^{(1,1)}$ and $\pi\Omega_{se}^{(1,1)}$ are collision integrals that are evaluated by logarithmic curve fits of T and T_e.[7]

Diffusion Coefficient

The binary diffusion coefficient is a function of specific heat, thermal conductivity, and Lewis number and is expressed as[17]

$$Lew = \frac{\rho\, Cp\, D_{sr}}{\eta} \tag{49}$$

APPENDIX 2: CHEMICAL KINETICS MODEL

The forward reaction rate coefficients were curve fit using the expression

$$k_f = A T^B e^{(-E/T)} \tag{50}$$

where T (° K) was equal to the heavy particle temperature, except for electron impact reactions where T was equal to the electron temperature. The reverse rate coefficients were based on the forward rate coefficients given by equation (51) and the equilibrium constant calculated with partition functions. The species reactions and corresponding constants used to model the chemically reacting flowfield of the AOTV flight regime are given in Table 4.

Reaction	A	B	E
$N_2 + N \rightleftarrows 3N$	4.085×10^{22}	-1.5	113000
$N_2 + N_2 \rightleftarrows 2N + N_2$	4.70×10^{17}	-0.5	113000
$N_2 + N^+ \rightleftarrows N_2^+ + N$	2.02×10^{11}	0.8	13000
$N + N \rightleftarrows N_2^+ + e^-$	1.40×10^{13}	0.5	67800
$N + e^- \rightleftarrows N^+ + 2e^-$	4.16×10^{13}	0.5	120000
$N + N \rightleftarrows N^+ + N + e^-$	2.34×10^{11}	0.5	120000
$N + N^+ \rightleftarrows 2N^+ + e^-$	2.34×10^{11}	0.5	120000
$N_2 + e^- \rightleftarrows 2N + e^-$	3.00×10^{24}	-1.6	113100

Table 4: Chemical Reactions and Rate Coefficients

APPENDIX 2: CHEMICAL KINETICS MODEL

The forward reaction rate coefficients were curve fit using the expression

$$k_f = A T^B e^{(-E/T)} \tag{50}$$

where T (° K) was equal to the heavy particle temperature, except for electron impact reactions where T was equal to the electron temperature. The reverse rate coefficients were based on the forward rate coefficients given by equation (51) and the equilibrium constant calculated with partition functions. The species reactions and corresponding constants used to model the chemically reacting flowfield of the AOTV flight regime are given in Table 4.

Reaction	A	B	E
$N_2 + N \rightleftarrows 3N$	4.085×10^{22}	-1.5	113000
$N_2 + N_2 \rightleftarrows 2N + N_2$	4.70×10^{17}	-0.5	113000
$N_2 + N^+ \rightleftarrows N_2^+ + N$	2.02×10^{11}	0.8	13000
$N + N \rightleftarrows N_2^+ + e^-$	1.40×10^{13}	0.5	67800
$N + e^- \rightleftarrows N^+ + 2e^-$	4.16×10^{13}	0.5	120000
$N + N \rightleftarrows N^+ + N + e^-$	2.34×10^{11}	0.5	120000
$N + N^+ \rightleftarrows 2N^+ + e^-$	2.34×10^{11}	0.5	120000
$N_2 + e^- \rightleftarrows 2N + e^-$	3.00×10^{24}	-1.6	113100

Table 4: Chemical Reactions and Rate Coefficients

VITA

Derek Scott Green was born in [redacted]. Soon after graduation from high school in Irving, Texas in May 1985, he began undergraduate studies at Texas A&M University. He obtained a B.S. degree in Aerospace Engineering in May 1989 and was accepted into the Texas A&M Graduate College that same spring. He will receive his M.S. degree in Aerospace Engineering in May of 1991 and is currently working in the aerospace industry at Lockheed Engineering and Science Company in Houston, Texas.

APPENDIX III

"The Effects of Shock Wave Precursors Ahead of Hypersonic Entry Vehicles"

by

S. A. Stanley and L. A. Carlson

AIAA Paper 91-1465

AIAA 91-1465

The Effects of Shock Wave Precursors Ahead of Hypersonic Entry Vehicles

S.A. Stanley and L.A. Carlson
Texas A&M University
College Station, TX

AIAA 22nd Fluid Dynamics, Plasma Dynamics & Lasers Conference
June 24-26, 1991 / Honolulu, Hawaii

For permission to copy or republish, contact the American Institute of Aeronautics and Astronautics
370 L'Enfant Promenade, S.W., Washington, D.C. 20024

The Effects of Shock Wave Precursors Ahead of Hypersonic Entry Vehicles

Scott A. Stanley*

and

Leland A. Carlson**
Texas A&M University
College Station, TX

Abstract

A model has been developed to predict the magnitude and characteristics of the shock wave precursor ahead of a hypervelocity vehicle. This model includes both chemical and thermal nonequilibrium, utilizes detailed mass production rates for the photodissociation and photoionization reactions, and accounts for the effects of radiative absorption and emission on the individual internal energy modes of both atomic and diatomic species. Comparison of the present results with shock tube data indicates that the model is reasonably accurate. A series of test cases representing earth aerocapture return from Mars indicate that there is significant production of atoms, ions and electrons ahead of the shock front due to radiative absorption and that the precursor is characterized by an enhanced electron/electronic temperature and molecular ionization. However, the precursor has a negligible effect on the shock layer flow field.

Nomenclature

AF - Radiation attenuation factor (-)
D_n - Dissociation energy for the nth species (eV)
e - Energy per unit mass (erg/g)
e''_e - Electron/electronic energy (erg/g)
E - Energy per particle (eV)
E_3 - Third exponential integral (-)
h - Static enthalpy (erg/g)
$h\nu$ - Photon energy (eV)
H - Total enthalpy (erg/g)
I_i - Ionization energy of the ith species (eV)
k - Boltzmann's constant (1.38×10^{-16} erg/°K)
k'_ν - Absorption coefficient (1/cm)
m_n - Mass per particle of the nth species (g)
M_n - Molecular weight of the nth species (g/Mole)
n_{diss} - Number of bound-free dissociation processes
n_{mb} - Number of molecular bands
n_s - Number of species
N_n - Number density of the nth species (1/cm^3)
p - Pressure (dyn/cm^2)
q - Radiative flux (W/cm^2)
$\hat{R}$ - Universal gas constant (8.317×10^7 erg/°K gram Mole)
T - Heavy particle temperature (°K)
T_e - Electron/electronic temperature (°K)
V - Velocity (cm/sec)
$\dot{w}$ - Mass production rate of the nth species (g/cm^3 sec)
x - Spatial variable in the precursor (cm)
Y - Absorption coefficient ratio (-)
β - One-half of the angle subtended by the body
ν - Frequency (1/sec)
ρ - Density (g/cm^3)
τ - Optical depth (-)

Subscripts
$elct$ - Electronic
i - for the ith process
j - for the jth electronic level
n - For the nth species
rot - Rotational
tr - Translational
vib - Vibrational
ν - At the frequency ν

Superscripts
TS - Tangent slab approximation
s - At the shock

Introduction

The recent emphasis placed on a mission to Mars and the subsequent return of samples has caused an increased interest in the development of accurate methods for predicting the fluid flow around hypersonic entry vehicles. This interest is a result of the plan to use an aerocapture technique to provide the reduction in velocity necessary to place the spacecraft in earth orbit. This technique uses aerodynamic drag, resulting from the interaction of the spacecraft with the earth's atmosphere, instead of propulsive braking to slow the vehicle to orbital speeds. Such an approach provides a reduction in the fuel necessary for the mission and an increase in the payload capabilities. A vehicle entering the earth's atmosphere upon return from Mars will experience velocities in the high hypersonic

---

* Member AIAA
** Professor Aerospace Engineering, Associate Fellow AIAA

Copyright © American Institute of Aeronautics and Astronautics, Inc., 1991. All rights reserved.

range, 11 Km/sec to 16 Km/sec.[1,2]

The majority of the recent work associated with hypersonic flow fields has involved the shock layer; but the shock wave precursor, on the other hand, has received little attention. The precursor is the region ahead of the shock wave in which radiation, primarily ultraviolet, emitted by the hot shock layer is reabsorbed by the gas. This absorption of radiation causes a heating of the gas in the precursor and the production of atoms as well as ions through the photoionization and photodissociation reactions. These changes might also in turn affect the gas behind the shock front. For example, the preheating of the gas in the precursor as well as the introduction of electrons and ions could potentially increase the rate at which the gas behind the shock approaches equilibrium. It has also been shown that for certain conditions the absorption of radiation ahead of the shock can cause significant increases in the radiative heating to the body.[3,4] Further, the presence of free electrons in the precursor can significantly affect communications with and identification of entry vehicles.[5,6]

Much of the previous work on shock wave precursors has been performed using shock tubes and shock tunnels[7,8,9] and a number of computational studies have also been performed.[10,11,12,13] The majority of this previous work, however, has involved monatomic gasses and is therefore not directly applicable to the earth's atmosphere.

The studies by Tiwari and Szema[13,14] as well as by Omura and Presley[15,16] involve diatomic gases and therefore are significant to a study of the earth's atmosphere. Tiwari and Szema calculated the effects of the precursor on the shock layer and the radiative heating of a body entering the hydrogen atmosphere of Jupiter, while Omura and Presley conducted a shock tube study of the electron densities ahead of strong shock waves in nitrogen as well as air.

The objective of this study was to develop a technique for predicting the character and magnitude of the chemical and thermal nonequilibrium shock wave precursor ahead of a hypervelocity entry vehicle that includes in detail the mass production due to photodissociation and photoionization of the various species and properly accounts for radiative absorption and emission effects on the internal energy modes of both atomic and diatomic species. A secondary objective was to ascertain the effect of this precursor on the vehicle flow field.

Radiative Transfer Formulation

In most of the previous work investigating shock wave precursors, several assumptions have been imposed on the radiative transfer calculations. A common assumption has been that the shock layer emits radiation as a black body at the equilibrium temperature behind the shock front.[10,12,17] Also, several of the previous works have utilized a multiple step absorption coefficient model[1,13,14] where at a given temperature, the species radiative properties have been assumed constant over specific frequency regions. However, since photochemical reactions are being considered, variations in the radiative transfer can cause significant changes in the gas. Likewise, the spectral details are very important in these calculations since the important radiative processes occur over different frequency ranges and the frequency of the photon absorbed as well as the process through which it is absorbed directly affects how the photon energy changes the energy of the gas. Without sufficient spectral detail, it is not possible to ascertain what portion of the radiation absorbed causes photoionization or photodissociation and what portion simply causes an increase in the internal energy of the gas.

Because of the necessity of accurate radiation predictions for the calculation of the photochemical reactions, it was decided that a complete spectrally detailed method of calculating the radiative flux was in order. Thus, an extensively modified version of the program RADICAL was utilized. This program, originally created by Nicolet[18], allows the user to select the frequency points used for the continuum radiation, so it was possible to obtain the spectral detail necessary for accuracy in the calculation of the photochemical reactions. RADICAL also performs detailed calculations of the atomic line radiation.

RADICAL, like many of the schemes currently used in the calculation of radiative transfer, uses the tangent slab approximation. This assumption is a one-dimensional approximation of the full equation of radiative transfer, which treats the radiation emitted at a point in the gas as if it were emitted by an infinite plane of gas positioned perpendicular to the direction of travel of the radiation. Since the thickness of the shock layer is much smaller than the body dimensions, each point in the shock layer is positioned close enough to the body that the rest of the gas in the radiating shock layer indeed appears to be of infinite extent; therefore, this is a reasonable assumption in the shock layer. The precursor, on the other hand, can extend to distances ahead of the shock which are of the same order of magnitude as the body diameter. Therefore, in the precursor, the radiating shock layer no longer appears to be of infinite extent but instead appears to be a slab of finite diameter.

In the one-dimensional problem, as in the shock layer, absorption is the only method by which the radiation is attenuated as it travels through the gas. Therefore, any decrease in the radiative intensity through the gas can be attributed to absorption, which in turn causes an increase in the energy of the gas equal to the decrease in the radiative energy. Since the shock layer does not appear to be of infinite extent at each point in the precursor, however, the radiation no longer behaves one-dimensionally. Consequently, in the precursor the radiative transfer is a three-dimensional problem in which a decrease in the

radiative intensity can occur due to the geometry as well as due to absorption.

This geometric attenuation in the precursor occurs due to the fact that the radiative energy emitted by the finite diameter shock layer propagates radially outward into the forward 180 degree semisphere. Therefore, as the energy emitted progresses outward the area through which it passes increases, thus producing a decrease in the radiative flux. This decrease, however, is not due to absorption by the gas and therefore has no effect on the gas.

Thus to use RADICAL for the radiation calculations, it was necessary to correct for the geometric attenuation of the radiation. This was done by expressing the radiative flux in the precursor as

$$q_\nu = AF_\nu \, q_\nu^{TS} \tag{1}$$

where q_ν^{TS} is the radiative flux at the point of interest using the tangent slab approximation and AF_ν is the geometric attenuation factor defined by

$$AF_\nu = \left[1 - Cos^2(\beta) \frac{E_3\left(\left(\tau_\nu - \tau_\nu^s\right) Sec(\beta)\right) - E_3\left(\tau_\nu Sec(\beta)\right)}{E_3\left(\tau_\nu - \tau_\nu^s\right) - E_3(\tau_\nu)}\right] \tag{2}$$

In this expression, β is half of the angle subtended by the body as viewed from the point of interest in the precursor. This expression is derived in detail by Stanley[19]

In the species continuity and energy equations, the terms involving the radiation appear as a divergence of the flux and are defined to account for the absorption and emission of radiation at a point. However, simple differentiation of equation (1) yields

$$\frac{\partial q_\nu}{\partial x} = AF_\nu \frac{\partial q_\nu^{TS}}{\partial x} + q_\nu^{TS} \frac{\partial AF_\nu}{\partial x} \tag{3}$$

In this expression, the first term on the right hand side is the change in the radiative flux due to the emission and absorption of radiation and the second term is the change due to the geometry of the problem and should not affect the gas. Therefore, the second term was neglected in the flow field calculations. Notice that if the second term was included in the species continuity and energy equations, an essentially transparent radiation would appear to be absorbed due to the spatial variation of the attenuation factor.

In order to properly account for the effects of absorption and emission of radiation on the energy of the gas, it is necessary to have an understanding of how each radiative process physically changes the particles involved. The effects of the absorption and emission of radiative energy on the internal energy modes depends on the type of radiative process as well as the frequency of the photon absorbed or emitted. Radiative processes can be separated into three categories: free-free, bound-bound and bound-free. While free-free and bound-bound processes cause a change in the energy of the gas with no chemical change, the bound-free processes are associated with chemical reactions in the gas, such as photoionization or photodissociation.

Photodissociation of the relatively cool nitrogen in the precursor occurs through a process called predissociation, a radiationless process in which a molecule transitions from a discreet electronic state to a dissociated state.[20] In cool nitrogen, this predissociation occurs primarily through the Lyman-Birge-Hopfield molecular band and the subsequent transfer out of the $a^1\Pi_g$ state into the repulsive $^5\Sigma_g^+$ state, Figure 1.

The radiative processes included in the calculation of the emission and absorption in the shock layer and precursor for this study are given in Table 1. The radiative processes included in the shock layer are those originally accounted for in the modified version of RADICAL. These processes include not only the continuum processes, but also the atomic lines associated with the nitrogen atom. Since only continuum processes were included in the precursor, the continuum mechanisms originally included in RADICAL were retained. Also, the photoionization of molecular nitrogen, the Lyman-Birge-Hopfield molecular band and the dissociation of molecular nitrogen through a continuum adjoining the Lyman-Birge-Hopfield band were added to the processes in RADICAL.

The absorption coefficients for photoionization of molecular nitrogen and the Lyman-Birge-Hopfield molecular band were determined using theoretical expressions derived according to Zel'dovich and Raizer[21]. For the photoionization process, the absorption coefficient was found to be given by the expression

$$k_\nu = 1.9986 \times 10^{-14} \frac{N_{N_2}}{(h\nu)^3} \sum_{j=j^*}^{\infty} \frac{1}{J^3} e^{-(x_1 - x_j)}$$

$$x_j = \frac{\left(I_{N_2} - E_{elct_j}\right)}{kT} \tag{4}$$

where the photon energy, $h\nu$, is given in electron volts. The lower limit on the summation over the electronic states in this equation is governed by the requirement that the photon energy be greater than the binding energy for the state. Otherwise, the photon has insufficient energy to cause photoionization.

For this study, the summation in equation (4) was limited to the lowest four electronic states of the nitrogen

molecule. However, in the cool precursor the populations of all except the ground electronic state were small. It should be noted that equation (4) provides values near the ionization threshold on the same order of magnitude as those predicted by Zel'dovich and Raizer[22] as well as those predicted by Marr[23].

The absorption coefficient for the Lyman-Birge-Hopfield molecular band was found to be given by

$$k_\nu = 9.1458 \times 10^{16} \frac{N_{N_2}}{T} e^{-\frac{(113{,}314.97 - 11{,}610.14\, h\nu)}{T}} \tag{5}$$

This equation was obtained from expressions given by Zel'dovich and Raizer[21] using an absorption oscillator strength of 3.7×10^{-6} from Allen[24] and then correcting to match experimental predictions given by Watanabe[25]. The absorption coefficient for the dissociation continuum adjoining this molecular band was assumed to be given by the expression

$$k_\nu = 4.97 \times 10^{-20} N_{N_2} \tag{6}$$

The constant in this equation was taken from the data presented by Watanabe for absorption through this process in cool air.

Precursor Formulation

For this study, the earth's atmosphere was modeled as pure nitrogen rather than a nitrogen oxygen mixture. This approach is a common simplifying assumption when performing nonequilibrium, hypervelocity flow field calculations since a nitrogen gas represents the properties of air quite well. In dealing with the precursor, however, the primary concern was whether or not the absorption processes of nitrogen sufficiently model those of air. After careful consideration it was decided that due to the predominance of nitrogen in the atmosphere it would be reasonable to represent the atmosphere as nitrogen in this initial study.

The effects of thermal nonequilibrium in the precursor were included in this study by permitting the free electrons and heavy particles to have different temperatures. Further, it was assumed that the free electrons and electronic states were in equilibrium at a common temperature, which as discussed by Nelson and Goulard[11], is one of the limiting cases for the precursor. For this region of the gas, the temperature governing the electronic states would normally be expected to be greater than the heavy particle temperature but less than the electron temperature. Thus, ideally a three temperature model should be used allowing a separate electronic temperature. Nevertheless, since the mechanisms and expressions for the transfer of energy between the electronic states and the free electrons are not well known or well understood, it was decided to use only a two temperature model. However, in order to correct for the local thermodynamic nonequilibrium between the electrons and the electronic states, a collision limiting correction[26] was applied to the populations of the molecular electronic states when computing the radiative emission and absorption phenomena.

For this study, the mass production rates in the precursor due to collisional reactions were neglected in comparison to those due to photochemical reactions. The photoreactions used in the precursor include the dissociation of molecular nitrogen and the ionization of both molecular and atomic nitrogen, i.e.

$$N_2 + h\nu \leftrightarrow^{k_{\nu 1'}} 2N$$

$$N_2 + h\nu \leftrightarrow^{k_{\nu 2'}} N_2^+ + e^-$$

$$N + h\nu \leftrightarrow^{k_{\nu 3'}} N^+ + e^-$$

The elastic collisional terms in the electron/electronic energy equation were evaluated using the collisional cross sections of Gnoffo, Gupta and Shinn[27].

The effects of the absorption of radiation through free-free and bound-bound processes were also included in this study. While these processes do not cause chemical reactions, they do cause an increase in the energy of the gas and their effects must be included in the electron/electronic energy equation. Absorption through atomic lines was neglected due to the expected low concentration of atomic species.

The equations governing the fluid properties on the stagnation streamline in the precursor are the steady, one-dimensional, nonequilibrium Euler equations.

Global Continuity

$$\frac{\partial}{\partial x}(\rho V) = 0 \tag{7}$$

Momentum

$$\rho V \frac{\partial V}{\partial x} + \frac{\partial p}{\partial x} = 0 \tag{8}$$

Energy

$$\rho V \frac{\partial H}{\partial x} + \frac{\partial q}{\partial x} = 0 \tag{9}$$

In equation (9), H is the total enthalpy of the gas defined in terms of the static enthalpy such that

$$H = h + \frac{1}{2}V^2 \tag{10}$$

where

$$h = \frac{p}{\rho} + \sum_{n=1}^{n_s}\left(e_{tr_n} + e_{rot_n} + e_{vib_n} + e_{elct_n} + e_n^o\right) \tag{11}$$

The second term in equation (9) is the gradient of the radiative flux. This term accounts for the increase or decrease in the energy of the gas due to absorption and emission of radiation. In addition to these equations, the equation of state for a two temperature gas is required,

$$p = \rho\hat{R}T\sum_{n=1}^{n_s}\left(\frac{\rho_n}{\rho}\frac{1}{M_n}\right) + \rho\frac{\hat{R}}{M_{e^-}}\frac{\rho_{e^-}}{\rho}(T_e - T) \tag{12}$$

To allow for the effects of thermal nonequilibrium, an electron/electronic energy equation was added to these equations,

$$\begin{aligned}\frac{\partial}{\partial x}(\rho V e''_e) = &-p_e\frac{\partial V}{\partial x} + \sum_{n=1}^{n_s}\xi_{e,n} + \dot{w}_e\frac{V^2}{2} - \frac{\partial q}{\partial x} \\ &+ \sum_{i=1}^{n_{diss}}\int_0^\infty \frac{Y_{v_i}^p\left(h\nu - \Delta E_{elct_i} - D_i\right)}{h\nu}\frac{\partial q_\nu}{\partial x}d\nu \\ &+ \sum_{i=1}^{n_{mb}}\int_0^\infty \frac{Y_{v_i}^p\left(h\nu - E_{elct_i}^{upp} + E_{elct_i}^{low}\right)}{h\nu}\frac{\partial q_\nu}{\partial x}d\nu\end{aligned} \tag{13}$$

where

$$e''_e = \frac{\rho_{e^-}}{\rho}e_{e^-} + \sum_{n=1}^{n_s}\left(e_{elct_n} + e_n^o\right) \tag{14}$$

In this equation, e_{e^-} is the kinetic energy of the free electrons, $3/2kT_e/m_{e^-}$, while e_{elct_n} and e_n^o are the electronic and zero point energies of the nth species. The last three terms on the right hand side of equation (13) allow for the effects of the absorption of radiation. This equation is derived in detail in Reference 19.

Chemical nonequilibrium was accounted for in the precursor through the addition of a species continuity equation for each of the five species in the problem. These equations are of the form

$$\rho V\frac{\partial\left(\frac{\rho_n}{\rho}\right)}{\partial x} = -m_n\int_0^\infty \frac{Y_{v_n}^s}{h\nu}\frac{\partial q_\nu}{\partial x}d\nu \tag{15}$$

where

$$\begin{aligned} Y_{v_{N_2}}^s &= -\frac{k'_{v_1} + k'_{v_2}}{k'_{v_{tot}}} & Y_{v_{N_2^+}}^s &= \frac{k'_{v_2}}{k'_{v_{tot}}} \\ Y_{v_N}^s &= \frac{2k'_{v_1} - k'_{v_3}}{k'_{v_{tot}}} & Y_{v_{N^+}}^s &= \frac{k'_{v_3}}{k'_{v_{tot}}} \\ Y_{v_{e^-}}^s &= \frac{k'_{v_2} + k'_{v_3}}{k'_{v_{tot}}} \end{aligned} \tag{16}$$

The term on the right hand side of equation (15) is the mass production rate of the nth species due to photoprocesses. The absorption coefficients, k'_{v1}, k'_{v2} and k'_{v3} are those for the absorption and emission processes associated with each of the three photochemical reactions discussed previously. Equation (15) is derived in detail in Reference 19.

In all of the above equations, the radiative terms, $\partial q/\partial x$, are the changes in the radiative flux due only to the absorption of radiation and not those due to the geometry of the problem as discussed in the previous section.

Shock Layer Formulation

In order to properly model the precursor ahead of a shock wave, it is necessary to know the spectral details of the radiation which passes from the shock layer and through the shock front to the precursor. In order to calculate these spectral details, the conditions of the gas in the shock layer must be known in detail. For the flight conditions of interest in this study, a number of important phenomena such as chemical and thermal nonequilibrium must be included to properly model the shock layer. Also, since the effects of radiation are of primary importance in the precursor, it is desirable that they be included in the shock layer model. The inclusion of these three phenomena can significantly affect the radiation and hence the precursor.

For this portion of the flow field, a viscous shock layer, VSL, scheme based on a version of the NASA code VSL3DNQ[28] was used. The version of VSL3DNQ used in this study was modified extensively by Carlson and Gally[29]. These modifications primarily involved the nonequilibrium chemistry and the effects of thermal nonequilibrium.

ORIGINAL PAGE IS
OF POOR QUALITY

However, they also modified the code to allow the shock layer and radiation calculations to be coupled to the gas dynamics, thus incorporating the effects of the emission and absorption of radiation into the flow field solution.

Results and Discussion

Figure 2 compares of the electron mass fractions found by Omura and Presley[15,16] in the precursor ahead of a shock wave in a nitrogen gas to those calculated using the present method. Omura and Presley measured the electron densities in the precursor using a 12 inch shock tube. The shock velocity for their case was 11.89 Km/sec. Shown in this figure, along with Omura and Presley's results, are two curves showing the electron mass fractions calculated using the current method. The dashed curve was calculated using Omura and Presley's freestream conditions and shock velocity with a 12 inch diameter body. However, the solid curve was calculated using a lower freestream density and pressure than Omura and Presley along with a larger diameter body scaled so that the conditions match those of Omura and Presley's case using binary scaling.

As can be seen from this figure, the electron mass fractions calculated using this method match those found by Omura and Presley reasonably well near the shock front. However, far from the shock they deviate. It is believed that the differences in the electron mass fraction far from the shock are due to the reflection of the radiative flux off of the shock tube walls in the Omura and Presley case. This reflection should greatly increase the quantity of radiation present far ahead of the shock wave over that which would be present in a free field such as is being used for the calculations. This increased presence of radiation far from the shock would induce greater absorption and thus an increase in the production of electrons due to photoionization. It is also interesting to note how well the two sets of calculations match using binary scaling.

The results discussed in the remainder of this section are representative of "typical" conditions for an aerobrake vehicle entering the earth's atmosphere upon return from Mars. These results were calculated for the stagnation streamline of a 2.3 meter nose radius vehicle at three altitudes, 72 Km, 75 Km and 80 Km. The shock layer calculations were made using 52 points between the shock wave and the body and allowing for atomic local thermodynamic nonequilibrium as well as radiation/gasdynamic coupling. The radiation calculations were made using 74 continuum frequency points selected to provide good spectral detail in the ultraviolet absorption region of interest in the precursor. A wall temperature of 1650 °K was used in both the shock layer and the radiation calculations.

72 Km, 16 Km/sec

Figure 3 shows the heavy particle temperature, electron/electronic temperature, pressure and the five species mole fraction variations through the precursor for this case. The radiative flux through the shock front for this case was 1,385.0 W/cm^2 and the spectral details of this radiation are shown in Figure 4. The shock standoff distance for this case was 6.60 cm. The radiation emitted from the shock layer for this case was the greatest of all of those considered. Thus this case experienced the largest flow field perturbations in the precursor region.

From these figures, it can be seen that the heavy particle temperature and pressure increased steadily through the precursor region. However, even for this extreme case the changes in these values were small. The density and velocity of the gas were found to be essentially constant in the precursor. This behavior verifies what was shown by Tiwari and Szema[13,14] and assumed by many others[10,11,12,15].

The electron/electronic energy of the gas also increased from a value of essentially zero in the freestream to a value on the order of 10^9 immediately ahead of the shock front. It should be noted that 99 percent of the radiative energy absorbed in the precursor affected the electron/electronic energy of the gas and only 1 percent of the energy affected the heavy particle translational, rotational and vibrational energies of the gas. Likewise, of the increase in the electron/electronic energy, 96 percent was involved with an increase in the zero point energy of the gas. Therefore, the majority of the energy absorbed in the precursor was involved with the ionization and dissociation of the gas.

The electron/electronic temperature behaved differently in the precursor than the other gas properties. It increased steadily to a maximum value of approximately 6,300 °K at a distance of 40 shock standoff distances ahead of the body. It then decreased rapidly to a value of 4,290 °K immediately ahead of the shock front. This decrease in the electron/electronic temperature was a result of the production of "low" energy electrons through photoionization caused by photons of frequencies only slightly larger than the ionization threshold of N_2. The production of these "low" energy electrons caused a decrease in the average energy per electron, hence a decrease in the electron/electronic temperature. That this decrease was a result of the production of "low" energy electrons rather than due to a transfer of energy from the electrons through elastic collisions was evident since there was no decrease in the electron/electronic energy accompanying this decrease in the electron/electronic temperature. This decrease also coincided with a region of rapid increase in the electron concentration in the gas due to the photoionization of molecular nitrogen.

The photons with energy near the ionization threshold of molecular nitrogen were absorbed rapidly in front of the shock since the strongest absorption region for an ionization process is at frequencies near the threshold. The higher energy photons in the weaker absorption range, far from the

ORIGINAL PAGE IS
OF POOR QUALITY

threshold, escaped to distances further from the shock where they were absorbed causing the creation of high energy electrons. The production of these high energy electrons resulted in a high electron/electronic temperature far from the shock. However, although the electron/electronic temperature was high far from the shock the electron mass fraction in this region was extremely small. It should be noted that a similar decrease in the precursor electron temperature near the shock was also predicted by Foley and Clarke[12], although they attributed it to collisional electron impact ionization.

Considering the mole fractions of the five species, it can be seen that the dominant chemical reaction far from the shock was the photoionization of atomic nitrogen. However, near the shock photoionization of molecular nitrogen dominated. The mole fractions of the ionized nitrogen molecule immediately ahead of the shock were at least an order of magnitude greater than those for the nitrogen atom and ionized nitrogen atom; although, there were significant quantities of all three species.

Due to the fact that the dominant change in the precursor was due to the photoionization of molecular nitrogen, the thickness of the precursor was considered to be the distance through which this reaction had an effect. By this definition, for this case the shock precursor thickness was in the range of 75 shock standoff distances, or 495 cm. Although there was a slight heating of the gas as well as the production of nitrogen atoms through photodissociation at greater distances from the shock, their effects were small compared to the changes within 495 cm of the shock front.

As can be seen in Figure 4, the radiation propagating through the shock wave from the shock layer into the precursor was distributed over a wide range of frequencies. A large portion of this radiative energy was in the infrared frequency range ($h\nu \leq 5$ eV). Most of the radiation in this region was emitted by the entry body itself; although, embedded within the continuum radiation from the body were a number of atomic lines. Also, the peak of radiation near 3.5 eV was due to three molecular bands, the 1st negative band of N_2^+ and the 1st and 2nd positive bands of N_2. There was also a large quantity of radiative energy in the ultraviolet frequency range. That above 10 eV was due primarily to the Birge-Hopfield band of molecular nitrogen as well as the ionization continuum and lines of atomic nitrogen. Through the visible frequency ranges (5 eV $\leq h\nu \leq$ 8 eV) there was very little radiative energy.

The second curve on Figure 4 shows the radiative flux at a position 75 shock standoff distances ahead of the shock front uncorrected for the geometric attenuation. By comparing this uncorrected radiative flux to the radiative flux through the shock front, it is possible to ascertain in what portion of the frequency range the cool precursor absorbed. This figure shows that the precursor absorbed radiation strongly at frequencies above the ionization threshold of molecular nitrogen, 15.59 eV. Although there was energy absorbed at frequencies less than this threshold due to photodissociation of molecular nitrogen and photoionization of atomic nitrogen, the amount of energy absorbed in these processes was small compared to that absorbed in the photoionization of molecular nitrogen. This result agrees with the previous statements that the dominant reaction was molecular ionization.

Through the course of this study it was found that even though there was significant production of dissociated and ionized nitrogen in the precursor region, the precursor had very little effect on the gas in the shock layer. By including these perturbed preshock conditions in the viscous shock layer calculations, it was found that they had negligible effect on the shock layer solution and produced no measurable change in the radiative heat transfer to the body. The primary change due to the inclusion of the precursor was in the conditions of the gas immediately behind the shock wave. Neglecting the precursor, the mass fractions for the free electrons, ions and atoms were zero upon crossing the shock; however, including the effects of the precursor these mass fractions had nonzero values. Likewise, including the effects of the precursor resulted in a slight increase in the electron temperature in the region immediately behind the shock front. However, within two spatial points of the shock front the shock layer solutions with and without the precursor agreed.

Parametric Studies

Figure 5 shows the electron number densities and the electron/electronic temperature in the precursor for three cases. All three of these cases were at a velocity of 16 Km/sec; however, each case was at a different altitude, 72 Km, 75 Km and 80 Km. The shock standoff distance and radiative flux through the shock front for each of these cases are presented in Table 2.

From these figures, it can be seen that for a constant velocity the magnitude of the changes in the precursor increased with decreasing altitude. This inverse relationship corresponds with trends observed by Dobbins[17] and was a result of two factors. First and foremost, as shown in Table 2, with the decrease in altitude the radiative flux through the shock increased due to an increase in the extent of the equilibrium region in the shock layer. Second, with the increase in density at the lower altitudes, a larger percentage of the radiation passing through the shock was absorbed before being attenuated due to the geometry.

It should also be noted that as the altitude decreased, the length of the precursor region decreased. This change was a result of the increased density at the lower altitudes, which caused the radiative mean free paths to decrease. Hence, the radiation was absorbed in a shorter distance ahead of the shock. This trend was also predicted by previous studies.[11]

Figure 6 shows the electron number densities and

electron/electronic temperature for four cases. All of these cases were at an altitude of 80 Km and the freestream velocities ranged from 10 to 16 Km/sec. The shock standoff distance and radiative flux through the shock front for each of these cases are presented in Table 2.

From these figures, it can be seen that at a constant altitude, as the freestream velocity increased the magnitude of the electron number densities in the precursor also increased. This trend was a result of the increase in the equilibrium temperature in the shock layer as the velocity increased and the accompanying rise in the radiative flux through the shock front; this trend is also in agreement with the results and predictions of previous researchers.[16,17] The precursor thickness also increased with velocity, again as a result of the increased radiative flux with velocity. As the radiative energy passing through the shock increased, a larger distance was required for this energy to be absorbed or attenuated ahead of the shock.

The increase in the velocity had varied effects on the electron/electronic temperature, however. The electron/electronic temperature at the shock decreased with velocity from 10 to 14 Km/sec. However, from 14 to 16 Km/sec it increased. This varied effect is due to differences in the quantity of "low" energy electrons created immediately ahead of the shock due to the ionization of molecular nitrogen. In fact, at 10 Km/sec there was insufficient ionization of molecular nitrogen ahead of the shock to cause a decrease in the electron/electronic temperature.

Conclusions

In this paper, a model for predicting the magnitude and characteristics of the shock wave precursor ahead of a hypervelocity vehicle has been presented. This method includes detailed mass production for photodissociation and photoionization and accounts for the effects of emission and absorption on the individual energy modes of the gas. This technique includes the effects of both chemical and thermal nonequilibrium as well as in the radiative flux calculations the consequences of local thermodynamic nonequilibrium for the molecular species.

This method has been used to determine the shock wave precursor ahead of vehicles entering the earth's atmosphere upon return from Mars. Comparison of the results to previous shock tube studies has shown that the method provides reasonably accurate results. The test cases have shown that there is significant production of atoms, ions, and electrons ahead of the shock front and that the precursor is characterized by molecular ionization and an enhanced electron/electronic temperature. However, the precursor has negligible effect on the subsequent shock layer flow field.

Acknowledgement

This work was primarily supported by NASA grant NAG-1-1003 from the NASA Langley Research Center, with Lin C. Hartung acting as technical monitor.

References

1 Smith, G.L., "Radiation-Induced Precursor Flow Field Ahead of a Reentering Body", PhD Thesis, Virginia Polytechnic Institute, Blacksburg, VA, March 1968.

2 Williams, S.D., "Pavlosky, J.E., and Curry, D.M., "A Preliminary TPS Design for MRSR-Aerobraking at Mars and at Earth", AIAA Paper 90-0052, Jan. 1990.

3 Lasher, L.E., and Wilson, K.H., "Effects of Shock Precursor Heating on Radiative Flux to Blunt Bodies", Lockheed Missiles and Space Co., Palo Alto, CA, NASA-CR-1265, 1969.

4 Tiwari, S.N., and Szema, K.Y., "Effects of Precursor Heating on Chemical and Radiative Nonequilibrium Viscous Flow Around a Jovian Entry Body", AIAA Paper 78-907, May 1978.

5 Wetzel, L., "Far-Flow Approximation for Precursor Ionization Profiles", *AIAA Journal*, Vol. 2, No. 7, July 1964, pp. 1208-1214.

6 Lederman, S., and Wilson, D.S., "Microwave Resonant Cavity Measurements of Shock Produced Electron Precursor", *AIAA Journal*, Vol. 5, No. 1, Jan. 1967, pp. 71-77.

7 Shreffler, R.G., and Christian, R.H., "Boundary Disturbances in High Explosive Shock Tube", *J. Appl. Phys.*, Vol. 25, No. 3, March 1954, pp. 324-331.

8 Voorhies, H.G., and Scott, F.R., "optical Measurements in a Helium Shock Tube", *Bull. Amer. Phys. Soc.*, Vol. 4, June 1959, p. 40.

9 Weymann, H.D., "Electron Diffusion Ahead of Shock Waves in Argon", *Phys. of Fluids*, Vol. 3, No. 4, July 1960, pp. 545-548.

10 Murty, S.S.R., "Effects of Line Radiation on Precursor Ionization", *J. Quant. Spect. Rad. Trans.*, Vol. 8, Sept. 1968, pp. 531-554.

11 Nelson, H.F., and Goulard, R., "Structure of Shock Waves with Nonequilibrium Radiation and Ionization", *Phys. of Fluids*, Vol. 12, No. 8, Aug. 1969, pp. 1605-1617.

12 Foley, W.H., and Clarke, J.H., "Shock Waves Structured by Nonequilibrium Ionizing and Thermal Phenomena", *Phys. of Fluids*, Vol. 16, No. 3, March 1973, pp. 373-383.

13 Tiwari, S.N., and Szema, K.Y., "Radiation Induced Precursor Flow Field Ahead of a Jovian Entry Body", AIAA Paper 77-768, June 1977.

14 Tiwari, S.N., and Szema, K.Y., "Influence on Precursor Heating on Viscous Flow Around a Jovian Entry Body", AIAA Paper 78-190, Jan. 1978.

15 Omura, M., and Presley, L.L., "Electron Density Measurements Ahead of Shock Waves in Air", *AIAA Journal*, Vol. 7, No. 12, Dec. 1969, pp. 2363-2365.

16 Omura, M., and Presley, L.L., "Further Studies of Precursor Electron Densities Ahead of Shock Waves", *Proceedings of the 4th Plasma Sheath Symposium*, NASA-SP-252, Oct. 1970, pp. 335-358.

17 Dobbins, R.A., "Photoexcitation and Photoionization of

Argon Ahead of a Strong Shock Wave", AIAA Paper 68-666, June 1968.

[18] Nicolet, W.E., "Advanced Methods for Calculating Radiation Transport in Ablation Product Contaminated Boundary Layers", Aerotherm Corp., Mountain View, CA, NASA-CR-1656, Sept. 1970.

[19] Stanley, S.A., "The Effects of Shock Wave Precursors Ahead of Hypersonic Entry Vehicles", Master's Thesis, Texas A&M University, College Station, TX, Dec. 1990.

[20] Herzberg, G., *Molecular Spectra and Molecular Structure, I. Spectra of Diatomic Molecules*, 2nd ed., Krieger, Malabar, FL, 1989.

[21] Zel'dovich, Y.B., and Raizer, Y.P., *Physics of Shock Waves and High-Temperature Phenomena*, Vol. 1, Academic Press, New York, NY, 1966.

[22] Zel'dovich, Y.B., and Raizer, Y.P., *Physics of Shock Waves and High-Temperature Hydrodynamic Phenomena*, Vol. 2, Academic Press, New York, NY, 1967.

[23] Marr, G.V., *Photoionization Processes in Gases*, Academic Press, New York, NY, 1967.

[24] Allen, R.A., "Air Radiation Graphs: Spectrally Integrated Fluxes Including Line Contributions and Self Absorption", Avco Corporation, Everett, MA, NASA-CR-556, 1965.

[25] Watanabe, K., "Ultraviolet Absorption Processes in the Upper Atmosphere", *Advances in Geophys.*, Vol. 5, 1958, pp. 153-221.

[26] Horton, T.E., "Radiative Coupled Nonequilibrium Flow Fields Associated with Aeroassisted Orbital Transfer", University of Mississippi, University, MS, NASA Contractor Rept. NAG-1-496, March 1986.

[27] Gnoffo, P.A., Gupta, R.N., and Shinn, J.L., "Conservation Equations and Physical Models for Hypersonic Air Flows in Thermal and Chemical Nonequilibrium", NASA Langley Research Center, Hampton, VA, NASA-TP-2867, Feb. 1989.

[28] Thompson, R.A., "Comparison of Nonequilibrium Viscous Shock Layer Solutions with Windward Surface Shuttle Heating Data", AIAA Paper 87-1473, June 1987.

[29] Carlson, L.A., "Nonequilibrium Radiation and Chemistry Models for Aerocapture Vehicle Flowfields", Texas A&M University, College Station, TX, TAMRF Rep. No. 6382-90-02, June 1990.

Table 1: Radiative Processes Included in the Shock Layer and Precursor

Radiative Process	Freq. Range
Shock Layer	
Free-Free, Bremsstrahlung	$0.0 < h\nu$
N - Low Frequency ionization (Highly excited states)	$0.0 < h\nu$
- High Frequency Ionization (Ground and first two excited states)	$10.9 < h\nu$
- Atomic Lines	–
N_2 - Birge-Hopfield Molecular Band	$6.50 < h\nu < 12.77$
- 1st Positive Molecular Band	$0.75 < h\nu < 4.5$
- 2nd Positive Molecular Band	$0.75 < h\nu < 4.5$
N_2^+ - 1st Negative Molecular Band	$2.23 < h\nu < 4.46$
Precursor	
Free-Free, Bremsstrahlung	$0.0 < h\nu$
N - Low Frequency Ionization (Highly excited states)	$0.0 < h\nu$
- High Frequency Ionization (Ground and first two excited states)	$10.8 < h\nu$
N_2 - Ionization Continuum (Ground and first three excited states)	$8.24 < h\nu$
- Birge-Hopfield Molecular Band	$6.5 < h\nu < 12.77$
- 1st Positive Molecular Band	$0.75 < h\nu < 4.5$
- 2nd Positive Molecular Band	$0.75 < h\nu < 4.5$
- Lyman-Birge-Hopfield Molecular Band	$4.77 < h\nu < 9.78$
- Dissociation Continuum (Adjoining Lyman-Birge-Hopfield molecular band)	$9.78 < h\nu$
N_2^+ - 1st Negative Molecular Band	$2.23 < h\nu < 4.46$

Table 2: Shock Standoff Distances and Radiative Fluxes

V (Km/sec)	Alt. (Km)	X_{shock} (cm)	q_{shock} (W/cm^2)
16	72	6.60	1,385.0
16	75	6.72	776.2
16	80	7.25	264.5
14	80	8.69	126.9
12	80	10.70	65.9
10	80	11.14	54.2

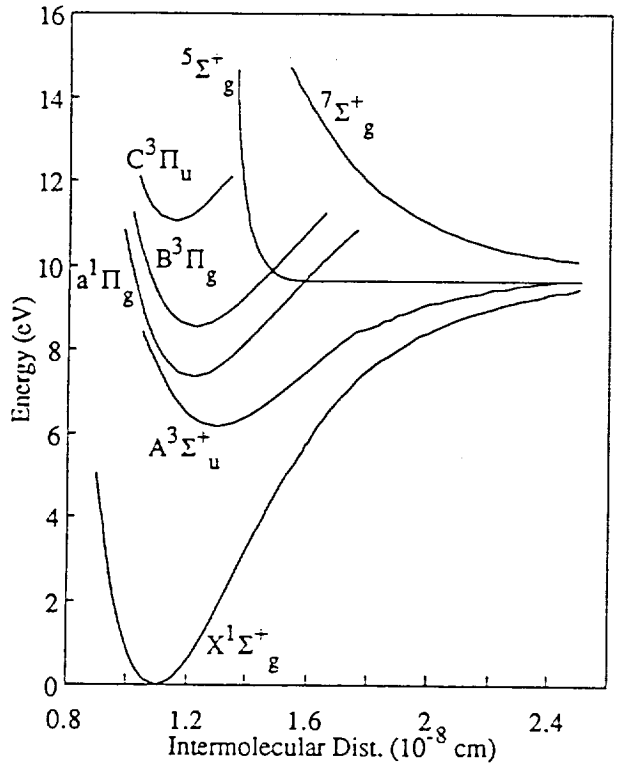

Fig. 1: Potential Energy Diagram of N_2

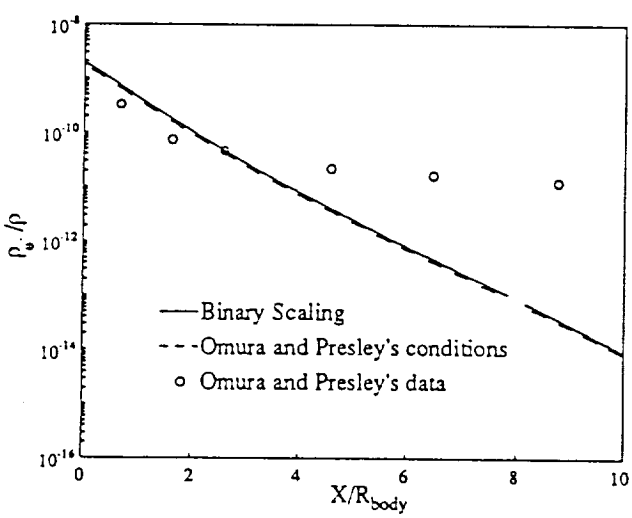

Fig. 2: Comparison Between Current Method and Shock Tube Data from Omura and Presley

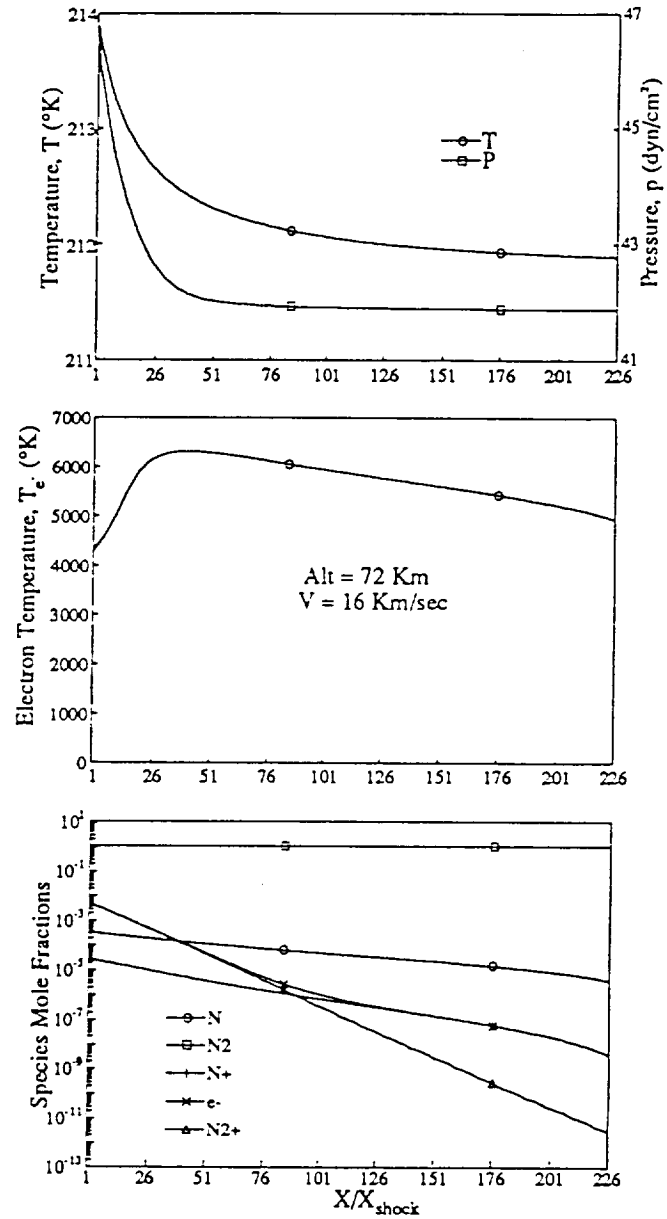

Fig. 3: Precursor Profiles for 16Km/sec Case at 72Km Alt.

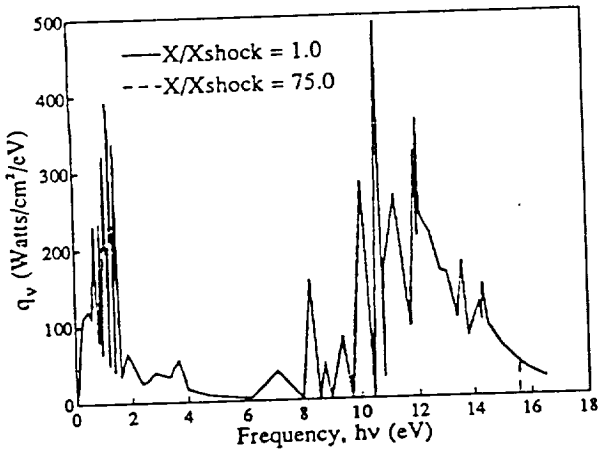

Fig. 4: Radiative Transfer for 16Km/sec Case at 72Km Alt.

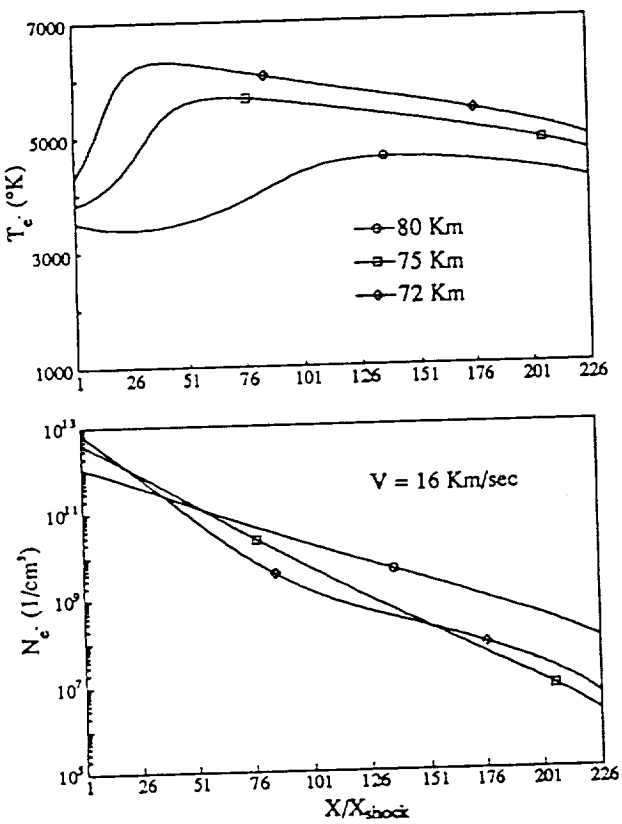

Fig. 5: Variation of the Precursor Flowfield with Changes in Altitude

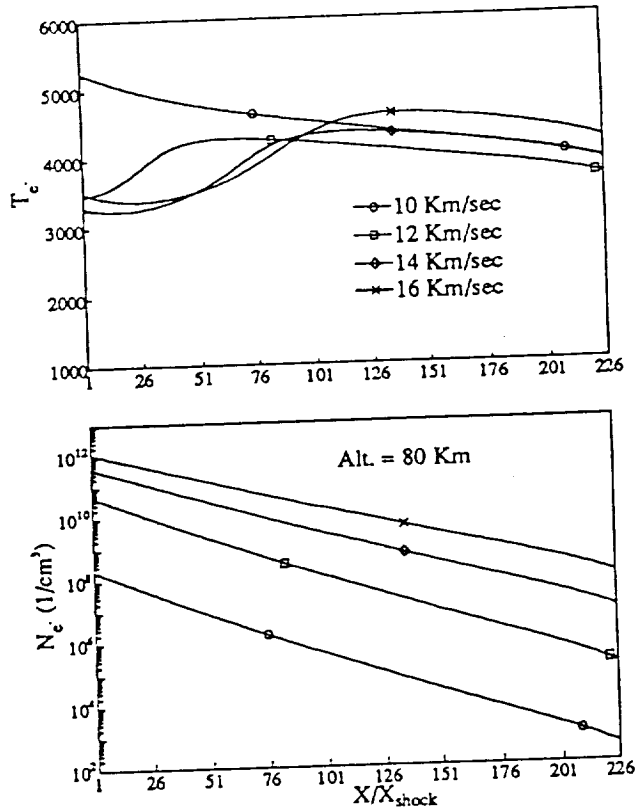

Fig. 6: Variation of the Precursor Flowfield with Changes in Freestream Velocity

APPENDIX IV

"Effect of Electron Temperature and Impact Ionization on Martian Return AOTV Flowfields"

by

L. A. Carlson and T. A. Gally

Journal of Thermophysics and Heat Transfer
Vol. 5, No. 1, January 1991, Pages 9-20

Effect of Electron Temperature and Impact Ionization on Martian Return AOTV Flowfields

L. A. Carlson and T. A. Gally

Reprinted from

Journal of Thermophysics and Heat Transfer

Volume 5, Number 1, January 1991, Pages 9–20

AIAA

A publication of the
American Institute of Aeronautics and Astronautics, Inc.
The Aerospace Center, 370 L'Enfant Promenade, SW
Washington, DC 20024-2518

PRECEDING PAGE BLANK NOT FILMED

Effect of Electron Temperature and Impact Ionization on Martian Return AOTV Flowfields

Leland A. Carlson* and Thomas A. Gally†
Texas A&M University, College Station, Texas 77843

Various electron impact ionization models in conjunction with a quasiequilibrium electron temperature model have been investigated and applied to the stagnation region of a hypothetical 2.3-m nose radius Martian return aeroassisted orbital transfer vehicle (AOTV). For the conditions considered, $U = 12$ km/s at 80 km, both multitemperature inviscid and viscous results indicate that a two-step ionization impact model predicts ionization distances in agreement with experimental data, that nonequilibrium chemistry and radiation effects are important throughout the stagnation zone, and that the quasiequilibrium electron temperature model is reasonable. Also, using a nongray emission-absorption radiation step model, it is shown that nonequilibrium causes a reduction in radiative heating from that predicted for equilibrium conditions and that, compared to an adiabatic wall, a cool wall (1650 K) results in a 28–45% reduction in radiative heating due to absorption near the wall.

Introduction

IN the future, various space programs will be conducted that will require the efficient return of large payloads to low Earth orbit (LEO) from missions to the moon or planets such as Mars. To accomplish this task, the return vehicles will utilize aerocapture techniques that will involve re-entry and deceleration at high altitudes, and to design these vehicles, a thorough understanding of the physical phenomena will be required. Because of the high altitudes associated with aerocapture, the vehicle flowfields will be dominated by chemical, thermal, and radiative nonequilibrium phenomena, which in many cases have not been extensively studied since the Apollo era.[1] Recently, as a result of the Aeroassisted Flight Experiment (AFE) program, results have been presented for aerocapture flowfields in the range of 7.5–10 km/s (Refs. 2–7). These results have demonstrated the importance of nonequilibrium phenomena in this flight regime.

However, for a Martian return vehicle the minimum nominal Earth entry velocity is approximately 12 km/s and the vehicle might be required under certain conditions to be able to operate and survive at Earth entry speeds up to 16 km/s.[8] At these higher velocities, the nonequilibrium phenomena will be different from those associated with the AFE vehicle. In the stagnation region, for example, nonequilibrium should be dominated by electron impact ionization processes instead of dissociation reactions; extensive thermal nonequilibrium involving at least three temperatures (heavy particle, vibrational, and electron) will exist; and the radiative heat transfer may be significantly affected by local thermodynamic nonequilibrium or nonequilibrium radiation effects. In addition, the electron temperature and nonequilibrium chemistry will be strongly coupled, and this coupling will influence the radiative heat transfer to the vehicle. Furthermore, at the higher end of the velocity range (14–16 km/s), the radiative transfer and the flowfield gasdynamics will be coupled due to the significant energy losses associated with radiation cooling.

Currently, several different engineering models and reaction rates have been postulated for electron impact ionization chemistry, all of which depend on the accurate prediction of electron temperature. The purpose of the present effort is to examine these different electron impact ionization models using flowfield results obtained from both inviscid and viscous, nonequilibrium chemistry, multitemperature computational models. By comparing the results with each other, the consequences of using a specific model can be determined. Furthermore, by comparing these results with experimental data, a suitable ionization model for the stagnation region can be determined.

Problem Formulation

Flowfield Models

In this study both inviscid and viscous flowfield representations have been utilized. For the inviscid calculations an improved version of a previously developed[6] nonequilibrium chemistry axisymmetric inverse method based on the work of Grosse[9] has been utilized as the basic Euler equation flow solver. This method permits arbitrary chemistry, includes options for a variety of vibration dissociation coupling models, and, in the computation of radiative transfer, accounts for nongray gas spectral and local thermodynamic nonequilibrium phenomena. For the present effort it has been further modified to include an electron temperature model and both one- and two-step atomic ionization models.

Since at the high altitudes and low densities of interest in aerocapture both viscous phenomena and wall thermal boundary-layer effects will be important, calculations have also been obtained using a modified version of the NASA Langley nonequilibrium chemistry viscous shock-layer code VSL3DNQ, which is an axisymmetric version of the SHTNEQ code described in Ref. 10. Like the inviscid code, this viscous shock-layer (VSL) method has also been modified to include an electron temperature model and both one- and two-step atomic ionization formulations. In addition, it has been combined with a nongray emission-absorption radiation model to permit the computation of radiative heat transfer. However, the effects of radiation gasdynamic coupling due to radiation cooling have not yet been included in the VSL formulation.

Presented as Paper 89-1729 at the AIAA 24th Thermophysics Conference, Buffalo, NY, June 12–14, 1989; received July 13, 1989; revision received Dec. 18, 1989. Copyright © 1990 by the American Institute of Aeronautics and Astronautics, Inc. All rights reserved.

*Professor, Department of Aerospace Engineering. Associate Fellow AIAA.

†Research Assistant, Department of Aerospace Engineering. Student Member AIAA.

Electron Impact Ionization

At conditions of interest for Earth return from Mars, the nonequilibrium chemistry region behind the bow shock will be dominated by ionization chemistry. Initially, ions will be produced via reactions involving NO^+ and N_2^+ and precursor photoionization, but once significant dissociation has occurred and reasonable amounts of atomic nitrogen and oxygen are present, the atoms will directly ionize in collisional reactions. Of these the most important are the electron impact reactions:

$$N + e^- = N^+ + e^- + e^- \tag{1a}$$

$$O + e^- = O^+ + e^- + e^- \tag{1b}$$

since they can induce electron avalanche and, thus, strongly affect the length and character of the nonequilibrium zone.

The classical model for these reactions uses standard forms for the species production terms, reaction rates, and equilibrium constant. This approach essentially assumes that the ionization mechanism proceeds via a one-step process, and a widely used set of reaction rates for these reactions consists of the following:

For $N + e^- = N^+ + e^- + e^-$,

$$k_f = 1.1 \times 10^{32} T_e^{-3.14} \exp(-169{,}000/T_e) \tag{2}$$

$$k_b = 2.2 \times 10^{40} T_e^{-4.5} \tag{3}$$

where k_f and k_b are the forward and reverse rate coefficients based on the local electron temperature T_e.

For $O + e^- = O^+ + e^- + e^-$,

$$k_f = 3.6 \times 10^{31} T_e^{-2.91} \exp(-158{,}000/T_e) \tag{4}$$

$$k_b = 2.2 \times 10^{40} T_e^{-4.5} \tag{5}$$

Following normal practice, it is assumed that in these reactions the governing temperatures are the electron temperatures. These rates were presented by Kang et al.[11] as part of an extensive reaction chemistry set, and results using this set yielded good agreement with electron probe measurements on the flank region of the RAM-C flight vehicle experiment. Both recombination coefficients, Eqs. (3) and (5), have the form resulting from elementary[12] and variational theory three-body collision theory,[13] and the coefficient is near the upper bound determined by Makin and Keck.[13] In fact, several figures in Ref. 11 are labeled "Results are for upper-bound reaction rate coefficients for de-ionization reactions."

Similar recombination rates were also used in reflected shock-tunnel nozzle flow investigations of C^+ recombination and O_2^+ and N_2^+ dissociative recombination in which good results were obtained.[14-16] However, as noted by the investigators, these experiments may not have been sensitive to these reactions since in one case the leading coefficient in Eq. (3) was varied by plus and minus two orders of magnitude with no effect on the data.[16] Also, these laboratory and flight experiments were for flows dominated by recombination and at lower electron densities and temperatures (2500–8000 K) than those that are of interest in the current investigation. Thus, although not establishing the validity of these rates for the present conditions, these experiments do not indicate that they are incorrect.

However, Park[17,18] measured the nitrogen ionic recombination rate at a nominal temperature of 10,000 K using an arc plasma wind tunnel and obtained values that corresponded to a recombination rate of

$$k_b = 5.02 \times 10^{42} T_e^{-5.27} \tag{6}$$

which is in reasonable agreement with the value of Kang et al.[11] He also suggested that the forward rate be obtained from

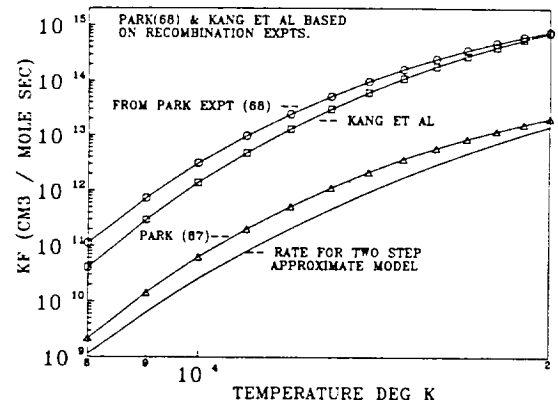

Fig. 1 Comparison of forward rate constants for $N + e^- = N^+ + e^- + e^-$.

the equilibrium constant, K_{eq}, via

$$K_{eq} = k_f / k_b \tag{7}$$

Both the Park forward rate corresponding to Eq. (6) and the Kang et al. forward rate given in Eq. (2) are plotted in Fig. 1. As can be seen, the agreement between the two rates over the range of electron temperatures of interest in the present study is good.

Now it should be recognized that, for the high temperatures of interest in the present effort, three-body deionization recombination will include significant electron capture into low-lying levels and collisional de-excitation should be rapid.[12] In addition, although the atomic electronic excited state populations may be in a Boltzmann distribution during recombination [i.e., local thermodynamic equilibrium (LTE)], at T_e, experimental evidence[19] indicates that many of the excited state population densities may not be in equilibrium with the number density of free electrons. As will be discussed later, this nonequilibrium with the free electrons during recombination is in contrast with the behavior that can be assumed to occur behind a shock wave during ionization.

Recently, Park[4] used a two-temperature ionizing air model and obtained good agreement with shock-tube, shock-tunnel, and flight measurements of phenomena immediately behind a shock front and/or in the stagnation zone and forward face region of blunt bodies. For these studies several of the reaction rates were adjusted in order to yield good comparisons with experimental data, and the forward rates for the reactions in Eq. (1) are considerably different from those given by Eqs. (2–7). These rates consist of the following:

For $N + e^- = N^+ + e^- + e^-$,

$$k_f = 2.5 \times 10^{33} T_e^{-3.82} \exp(-168{,}600/T_e) \tag{8}$$

For $O + e^- = O^+ + e^- + e^-$,

$$k_f = 3.9 \times 10^{33} T_e^{-3.78} \exp(-158{,}500/T_e) \tag{9}$$

and the forward rate for atomic nitrogen electron impact ionization is plotted in Fig. 1. Note that it is almost two orders of magnitude smaller than the rates based on recombination.

The second model for atomic ionization is an engineering approximation based on various theories involving the ionization of argon[20-24] and the application of these theories to nitrogen and oxygen.[25,26] This approach assumes that atomic ionization is not a one-step process but proceeds via a two-step chain involving excitation to an excited state followed by rapid ionization controlled by the local charged particle concentrations and the electron temperature. This concept applies not only to electron impact ionization but also to heavy particle ionization involving atom-atom and atom-ion collisions.

Unfortunately, because of the two-step process, the usual mass production rate formulation is not completely adequate.

For example, assume that the atom-atom ionization process proceeds as follows:

$$N_g + M = N^* + M \tag{10}$$

$$N^* = N^+ + e^- \tag{11}$$

where N* refers to atomic nitrogen in an excited state. By assuming that the first step is rate determining, that dN^*/dt is approximately zero, and that the ground state concentration approximately equals the atom concentration, kinetics yields the rate of species mass production per unit volume $\dot{\omega}_s$ to be

$$\dot{\omega}_{N^*,\,\mathrm{total}} = \mathfrak{M}_N\{k_f[N_g][M] - k_b[N^*][M]\} + \dot{\omega}_{N^*,11} \tag{12}$$

where k_f and k_r are for Eq. (10), brackets denote concentration, $\mathfrak{M}_s$ is the molecular weight of species s, and the subscript 11 refers to Eq. (11). However, by assumption,

$$\dot{\omega}_{N^*,\mathrm{total}} = 0$$

so that

$$\dot{\omega}_{N^*,11} = -\mathfrak{M}_N\{k_f[N_g][M] - k_b[N^*][M]\} \tag{13}$$

But k_f and k_r are related by the equilibrium constant for Eq. (10):

$$K_{eq} = \frac{g^* \exp(-E^*/kT)}{g_g} = \frac{k_f}{k_b}$$

where g is the degeneracy of the indicated energy level E, and k is the Boltzmann constant. Thus, Eq. (13) becomes

$$\dot{\omega}_{N^*,11} = -\mathfrak{M}_N k_f[N_g][M]\left\{1 - \frac{g_g \exp(E^*/kT)[N^*]}{g^*[N_g]}\right\} \tag{14}$$

At this point, a rate expression relating the excited state to the ions and free electrons could be introduced instead. However, based on experimental evidence for monoatomic gases,[19,24] it can be assumed as an approximation that the excited states of nitrogen are in equilibrium with the free electrons and ions at the electron temperature. Thus,

$$\frac{N_e N_{N^+}}{N_{N^*}} = \frac{Q^{el}_{N^+} Q_{e^-} \exp(-X/kT_e)}{g^*} \tag{15}$$

where X is the ionization potential from the excited state, Q^{el}_s is the electronic partition function of species s, and Q_{e^-} is the partition function for the electrons defined by

$$Q_{e^-} = 2\left(\frac{2\pi m_e kT_e}{h^2}\right)^{3/2}$$

where h is the Planck constant and m_e is the electron particle mass. Substituting Eq. (15) into Eq. (14) and noticing that

$$\dot{\omega}_{e,11} = (\mathfrak{M}_e/\mathfrak{M}_N)\dot{\omega}_{N^*,11}$$

yields, for $M = N$,

$$\dot{\omega}_{e,N} = \mathfrak{M}_e k_f[N]^2\left[1 - \frac{g_g \exp\left(\frac{E^*}{kT} + \frac{X}{kT_e}\right) AV[e^-][N^+]}{Q_{e^-} Q^{el}_{N^+}[N]}\right] \tag{16}$$

where AV is Avogadro's constant, and the subscript 11 is replaced by the incident particle for the two-step reaction, M.

A similar analysis for $M = N^+$ ionization yields

$$\dot{\omega}_{e,N^+} = \mathfrak{M}_e k_f[N][N^+] \times \left[1 - \frac{Q^{el}_N \exp\left(\frac{E^*}{kT} + \frac{X}{kT_e}\right) AV[e^-][N^+]}{Q_{e^-} Q^{el}_{N^+}[N]}\right] \tag{17}$$

whereas, for electron impact ionization, $M = e^-$, the result is

$$\dot{\omega}_{e,e} = \mathfrak{M}_e k_f[N][e^-]\left[1 - \frac{g_g \exp\left(\frac{I}{kT_e}\right) AV[e^-][N^+]}{Q_{e^-} Q^{el}_{N^+}[N]}\right] \tag{18}$$

Similar expressions could be obtained for atomic oxygen ionization.

Notice that the production rates involving heavy particles (atoms and ions) are governed by both the electron and the heavy particle temperature, whereas the production rate for the atom-electron reactions involves only the electron temperature but has the classical form. Furthermore, the forward rate coefficient is for the limiting step and only uses the energy of the assumed excited state and not the ionization energy. Wilson,[25] using the work of Petschek and Byron,[27] assumed that the rate-limiting step in the ionization process was the excitation of the atoms to the level involving the largest energy jump, i.e., to the $3s^4P$ for nitrogen and to the $3s^5S$ state for oxygen, and they proposed a form for the excitation rate. It should be noted that for oxygen and nitrogen this rate-limiting step is for the temperatures of interest here and differs from that used in Ref. 13, which was only 2.5 eV below the ionization level.

Using this theory, Wilson obtained good agreement with shock-tube data for ionization distances behind shock waves in air. Subsequently, these forms were used to deduce rates that were used to study nonequilibrium radiating phenomena behind reflected shock waves[26] and the AFE stagnation region.[6]

Thus, based on the theory and results presented in Refs. 24–26, reaction rates consistent with the two-step approximate model given by Eqs. (10–18) consist of the following:

For $N + e^- = N^+ + e^- + e^-$,

$$k_f = 4.16 \times 10^{13} T_e^{0.5} \exp(-120{,}000/T_e) \tag{19}$$

For $O + e^- = O^+ + e^- + e^-$,

$$k_f = 5.49 \times 10^{13} T_e^{0.5} \exp(-104{,}500/T_e) \tag{20}$$

For $N + N = N^+ + e^- + N$ and $N + N^+ = N^+ + e^- + N^+$,

$$k_f = 2.34 \times 10^{11} T^{0.5} \exp(-120{,}000/T) \tag{21}$$

The forward rate given by Eq. (19) is also shown in Fig. 1 and is in reasonable agreement with the ionization rate of Park.[4] As can be seen, both of the rates associated with ionization processes are considerably slower than those deduced from recombination experiments and theory. However, the difference might be due to fundamental differences in the processes involved. In the shock-tube case the process is dominated by forward ionization, and in the rate derivation it was assumed that the excited states were in equilibrium with the free electrons and ions. In the shock- and arc-tunnel experiments, the chemistry is dominated by recombination, and, as mentioned earlier, there is experimental evidence[19] that during

recombination the excited states may not be in equilibrium with the free electrons.

Electron Temperature Model

Besides chemical nonequilibrium, it is possible for a partially ionized gas to have regions of thermal nonequilibrium between electrons and the other heavier species. Such thermal nonequilibrium occurs because the rate of energy exchange between electrons and heavy particles is very slow due to the large mass differences in the species, and it is characterized by different free electron and heavy particle temperatures. Since atomic ionization and radiative transfer are dependent on and strongly coupled to the electron temperature, accurate models for computing it are essential.

Over the years a variety of models for determining the electron temperature have been presented[4-6,20-23,26,28-33] that differ in detail, level of complexity, and ease of solution. All of these start from the equation representing conservation of electron energy, which can be written as

$$\frac{D(\rho_e h_e)}{Dt} + \rho_e U_e \cdot \frac{D(u)}{Dt} + \frac{\partial}{\partial r} \cdot q_e + \rho_e h_e \left(\frac{\partial}{\partial r} \cdot u \right) - \frac{D(p_e)}{Dt} + [\tau_e] : \left[\frac{\partial}{\partial r} ; u \right] - N_e X_e \cdot U_e - \dot{\omega}_e \frac{u^2}{2} = \sum_{j=1}^{S} (\xi_{ej} + U_e \cdot P_{ej}) + Q_e \tag{22}$$

If Bremmstrahlung and viscous stress effects are ignored, this equation becomes, showing only one dimension for simplicity,

$$\rho_e u_e \frac{\partial h_e}{\partial x} - u \frac{\partial p_e}{\partial x} + \frac{\partial}{\partial x} \left(-\lambda_e \frac{\partial T_e}{\partial x} \right) + \frac{\partial}{\partial x} (\rho_e U_e h_e) + \dot{\omega}_e h_e - h_e \frac{\partial}{\partial x} (\rho_e U_e) - \dot{\omega}_e \frac{u^2}{2} = U_e \frac{\partial p_e}{\partial x} + \sum_{j=1}^{S} (\xi_{ej} + U_e P_{ej}) + Q_e \tag{23}$$

where the first term on the right side represents the effect of external forces and is obtained from the electron momentum equation; the second term accounts for the rate of energy gain by electrons due to elastic encounters because of thermal motion of the particles; the third term represents the energy gain resulting from elastic encounters because of the relative fluid motion of the electrons; and the last term represents energy change due to inelastic encounters. The velocity U_e is the electron diffusion velocity.

In the past, several investigators,[20-23,26] using the full electron energy equation, have obtained results which indicate that when significant ionization is present in the postshock nonequilibrium zone the electron temperature is essentially constant at a value 10–15% above the theoretical equilibrium temperature until the heavy particle temperature falls to that value. After that, the two temperatures are essentially the same. Obviously, the use of such a constant temperature would simplify the electron temperature calculations, and this approach has been used in approximate flowfield solutions[31,34] and was considered for the present study. However, preliminary calculations demonstrated the difficulty of selecting a priori an appropriate effective constant electron temperature, and this approach was abandoned.

Another approach successfully used in the past for AFE flowfields[4,6] is to assume that the nitrogen vibrational temperature and the electron temperature are equal and to combine the electron and vibrational energy equations. This method is based on experimental data[35] and theoretical calculations[4,5] which show that, near 7000 K, vibrational processes strongly influence the electron temperature. However, for the conditions of the present study, temperatures are normally above 10,000 K, dissociation occurs rapidly behind the shock front, and the concentration of N_2 is very low over most of the nonequilibrium zone. Thus, vibration electronic coupling should not be significant, and this approach was not utilized in the present study.

Another model that has been used in the past[32,33] is the "quasiequilibrium approximation," in which all derivative terms are neglected in the electron energy equation. If it is further assumed that the charge exchange cross section between atoms and ions is sufficient to ensure that they have the same diffusion velocity and, due to rapid dissociation, that the concentration of diatomic molecules is low over most of the shock layer, then diffusion terms can also be neglected. Thus, Eq. (23) becomes

$$\dot{\omega}_e h_e - \dot{\omega}_e \frac{u^2}{2} = \sum_{j=1}^{S} \xi_{ej} + Q_e \tag{24}$$

Since vibration electronic coupling has been neglected, the inelastic term Q_e is composed of effects due to chemical reactions involving electrons. When an electron is created by an electron-atom reaction, the electron that caused the ionization will lose energy equivalent to the ionization potential E_I plus the energy of the created electron, which on the average is, say, e_{av}. The original electrons will rapidly equilibrate by elastic collisions and will have collectively lost energy $E_I + e_{av}$. The equilibration between the original electrons and the newly created one will not affect the energy per unit volume since it only involves a transfer of energy from one particle to another. Thus, the net energy loss from an electron atom ionization process is E_I, and the total is $\dot{\omega}_{e,eA} E_I / m_e$.

Similarly, every time an atom-atom ionization occurs, an electron of average energy e_{AA} is created, and the total energy gain for these processes is $\dot{\omega}_{e,AA} e_{AA} / m_e$. This is also the case for atom-ion ionization. Thus,

$$Q_e = -\frac{\dot{\omega}_{e,eA} E_I}{m_e} + \frac{\dot{\omega}_{e,AA} e_{AA}}{m_e} + \frac{\dot{\omega}_{e,AI} e_{AI}}{m_e} \tag{25}$$

For the present conditions, however, the electron-atom process should be the dominant ionization mechanism and the last two terms should be negligible.[21,26] For the parts of the flowfield where the other reactions are important, the concentration of electrons should be low enough that any error resulting from neglecting them in Eq. (25) should be small. Thus, only the first term of Eq. (25) need be retained.

General forms for the elastic interaction terms have been derived using collision integral theory in Ref. 36. Since diffusion effects are ignored in the quasiequilibrium model, these interaction terms can be reduced to

$$\xi_{ej} = [(m_e T_e)^{1/2} / m_j] S_{ej} N_e N_j (1.03478 \times 10^{-23})(T - T_e) \tag{26}$$

where centimeter-gram-second units are assumed; terms involving m_e have been dropped relative to heavy particle masses; and S_{ej} is the collision cross section between electrons and species j.

By substituting Eqs. (25) and (26) into Eq. (24), dropping the small term involving u^2 and rearranging, an approximate equation for the free electron temperature is

$$T_e = T - \frac{1.23357 \times 10^{-10}}{T_e^{1/2} SX [e^-] m_e} \times \left(\dot{\omega}_{e,eN} E_{I_N} + \dot{\omega}_{e,eO} E_{I_O} + \dot{\omega}_e \frac{5}{2} k T_e \right) \tag{27}$$

where

$$SX = N_N S_{eN} + N_O S_{eO} + N_{N^+} S_{eN^+} + N_{eO^+} S_{eO^+} + \tfrac{1}{2}(N_{N_2} + N_{O_2}) S_{eM}$$

Note that this equation is nonlinear since the cross sections are functions of translational and electron temperature as well as concentrations and that the various production rates also depend on both temperatures. In the present study an iterative method for solving this equation has been developed and included in both the inviscid and viscous flowfield solvers.

Chemistry Models

Since the primary objective of the present effort is to use multitemperature flowfield models to investigate the effect of different impact ionization models, the reaction chemistry schemes have been kept as simple as possible. For air, the 10 species, 11 reaction model shown in Table 1 has been used. Although this scheme is not as complete as some others (Ref. 11, for example), it should be adequate for the present study. In addition, numerical experiments were conducted using for the nitrogen dissociation reaction a series of reaction rates that varied by several orders of magnitude. For the conditions investigated, no significant effects on the ionization processes were observed.

However, since the air model did not contain all possibilities, particularly with respect to dissociation and oxygen ionization, results have also been obtained assuming a pure nitrogen freestream. At the conditions of interest, nitrogen is a reasonable representation of nonequilibrium radiating air, and more details can be included using a smaller number of species and reactions. The nitrogen reaction chemistry set consisting of five species and eight reactions is shown in Table 2. Notice that charge exchange is included.

In general, with the exception of the atomic ionization reactions, the rates shown in Tables 1 and 2 are similar to those used by other investigators[3,6,26,33,35] and are in the form

$$k_{f,b} = AT^B \exp(-E/T)$$

As noted in the tables, computations involving the one-step ionization models and the rates in Eqs. (2-5) will be termed case 1, and those using the two-step ionization model and the rates in Eqs. (19) and (20) are case 2.

Vibration Dissociation Coupling

It is well established that, in general, vibration dissociation coupling strongly influences the dissociation of diatomic molecules.[4-6] However, at the temperatures and velocities associated with the present study, dissociation occurs rapidly, and the influence of vibration dissociation coupling on the ionization processes is small. To confirm this, numerical experiments were conducted with the inviscid flowfield model using vibrational equilibrium, coupled vibration-dissociation-vibration (CVDV) coupling, and modified CVDV (MCVDV) coupling, and no significant differences between the results regarding the ionization processes were observed. Consequently, in the inviscid flow solver, the MCVDV model developed in Ref. 6 has been used. This coupling model includes corrections to the Landau-Teller relaxation time correlation to prevent unrealistically short relaxation times at high temperatures and accounts for the diffusive nature of vibrational relaxation at high temperatures.[4]

In its original form the viscous shock-layer code, VSL3DNQ, did not contain any vibration dissociation coupling model. Since the inviscid studies indicated that, for conditions associated with Earth entry return from Mars, vibrational coupling effects were small, the VSL code has not been modified, and all viscous calculations have assumed vibrational equilibrium.

Radiation Model

At the lower velocities associated with the Earth return from Mars of an aeroassisted orbital transfer vehicle (AOTV), i.e., 12 km/s, radiative heat transfer and associated self-absorption effects should be important, but the total radiative losses from the flowfield should be sufficiently small so that there is not any significant radiative gasdynamic coupling. Thus, once a flowfield solution has been obtained for a given reaction chemistry system, the flowfield solution can be used to compute the body radiative heat transfer. In the present study, the tangent slab approximation has been used, the wall surface is assumed to be nonemitting and nonablating, and precursor effects are assumed negligible. Also, an eight-step nongray absorption coefficient model based on the work of Olstad[37] and similar to that used in Ref. 6 has been used. However, it has been modified to yield, under equilibrium conditions, results with respect to both magnitude and spectral distribution that in general agree with RADICAL, the NASA Langley version of a detailed radiation program documented in Ref. 38. Based on a series of calculations, these modifications consisted of a reduction in the effective absorption cross sections in the frequency range of 6.89-10.98 eV, which is composed not only of continuum radiation but also several important lines. This step model has yielded reasonable engineering results for AFE flowfields[6] and, in conjunction with an approximate flow solver, has correlated well with the Fire 2 flight experiment.[34]

A spectral comparison between stagnation-point radiative heating predictions obtained using the present eight-step model and RADICAL is shown in Fig. 2. These results were obtained using the viscous flow solver with 99 points between the shock and the wall, case 1 rates, and assuming an adiabatic wall, and almost the entire shock layer for this case was in chemical and thermal equilibrium. The presence of line contributions is evident in the RADICAL results by the tall narrow peaks on top of the continuum curves in the infrared (0-3.1 eV) and ultraviolet (8-12 eV). Since the radiative heating to the wall is the area under these curves, it can be seen that, in general, the two models agree quite well, and, in fact, the results are within 15% overall. [Note that the vacuum ultraviolet (VUV) band in the eight-step model that starts at 14.56 eV actually extends to 31 eV.] However, the eight-step model still does appear to slightly overpredict the heating in the range of 6.89-10.98 eV, and further improvements can probably still be made. Nevertheless, particularly when computational efficiency is considered, the modified eight-step absorption coefficient model should be adequate for engineering and comparison studies.

In addition, the present radiation model contains a method for computing approximate correction factors that account for the effects of local thermodynamic nonequilibrium (LTNE). Such LTNE can exist in the chemical nonequilibrium

Table 1 Air reaction system

Reaction		A	B	E	Direction
$O_2+M=2O$	$+M$	1.19×10^{21}	-1.5	59,380	Forward
$NO+M=N$	$+O+M$	5.18×10^{21}	-1.5	75,490	Forward
$N_2+M=2N$	$+M$	2.27×10^{21}	-1.5	0	Backward
$N+O_2=NO$	$+O$	1.00×10^{12}	0.5	3,120	Forward
$N_2+O=NO$	$+N$	7.00×10^{13}	0.0	38,016	Forward
$N+O=NO^+$	$+e^-$	1.80×10^{21}	-1.5	0	Backward
$N+N=N_2^+$	$+e^-$	1.40×10^{13}	0.0	67,800	Forward
$N+N=N$	$+N^++e^-$	2.34×10^{11}	0.5	120,000	Forward
$N+N^+=2N^+$	$+e^-$	2.34×10^{11}	0.5	120,000	Forward
$N+e^-=N^+$	$+2e^-$	Eqs. (2) and (3) for case 1, (19) for case 2			
$O+e^-=O^+$	$+2e^-$	Eqs. (4) and (5) for case 1, (20) for case 2			

Table 2 Nitrogen reaction system

Reaction		A	B	E	Direction
$N_2+N_2=2N$	$+N_2$	4.70×10^{17}	-0.5	113,000	Forward
$N_2+N=2N$	$+N$	4.085×10^{22}	-1.5	113,000	Forward
$N_2+M=2N$	$+M$	1.90×10^{17}	-0.5	113,000	Forward
$N_2+N^+=N_2^+$	$+N$	2.02×10^{11}	0.8	13,000	Forward
$N+N=N_2^+$	$+e^-$	1.40×10^{13}	0.0	67,800	Forward
$N+N=N$	$+N^++e^-$	2.34×10^{11}	0.5	120,000	Forward
$N+N^+=2N^+$	$+e^-$	2.34×10^{11}	0.5	120,000	Forward
$N+e^-=N^+$	$+2e^-$	Eqs. (2) and (3) for case 1, (19) for case 2			

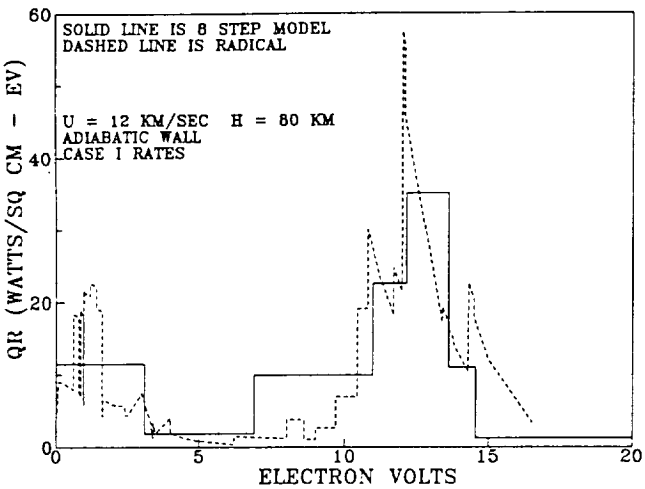

Fig. 2 Stagnation-point radiative heat transfer from RADICAL and eight-step model.

region immediately behind the shock front where, due to ionization via excited states, the populations of the electronic states may not be that predicted by an LTE assumption using the ground state. The rationale behind these factors and their derivation has been presented in Refs. 6 and 34, and similar factors have been used for monoatomic gases.[20–23] The inclusion of radiation nonequilibrium effects is essential for accurately predicting radiative heat transfer at high-altitude conditions.[4–6,34]

Originally, these LTNE factors were expressed in terms of the degree of dissociation and ionization,[6,34] which were often difficult to compute accurately. However, Greendyke[39] has pointed out that they can be more simply expressed in terms of the partition functions. Thus, the atomic nitrogen LTNE correction factor can be written as

$$\frac{N_{N^+} N_e Q_N^{el} \exp(169{,}000/T_e)}{N_N Q_{N^+}^{el} Q_{e^-}} \tag{28}$$

For radiation processes involving the ground state, this factor is multiplied by the blackbody function for that region to yield the effective source function, and the absorption coefficient is unchanged. On the other hand, for processes involving excited states, the factor is multiplied by the absorption cross section to yield the effective absorption coefficient, and the source function for that spectral region is unchanged. Additional details are presented in Ref. 6, and similar forms can be obtained for molecular radiation.

For cases where the reaction chemistry set is such that an opposite rate is obtained from a forward or reverse rate in conjunction with an equilibrium coefficient computed from partition functions, the correction factor form given in Eq. (28) is appropriate. This situation is the case with the two-step ionization model, whose rates have been designated case 2. In other words, in that case the factor predicted by Eq. (28) will go to one as the flow approaches ionization equilibrium.

However, when the one-step ionization rates of Kang et al.[11] are used, case 1, the ionization equilibrium coefficient is determined by the ratio of the forward-to-reverse rates [Eqs. (2–5)] and not by partition functions. In that case the atomic nitrogen LTNE correction factor should be computed using

$$(N_{N^+} N_e)/N_N A V K_{eq} \tag{29}$$

and the equilibrium coefficient is given by

$$K_{eq} = k_f/k_b = 5 \times 10^{-9} T_e^{1.36} \exp(-169{,}000/T_e) \tag{30}$$

If this approach is not taken, the factors will not approach one as chemical equilibrium is approached, and ridiculous answers may result.

For viscous cases in which a cool wall is considered, recombination processes will dominate in the wall thermal layer, and, as mentioned earlier, there is evidence that during recombination the excited states may not be in equilibrium with the free electrons and ions and the electronic states may all be populated according to a Boltzmann distribution, i.e., in LTE with the ground state. Consequently, in the wall thermal layer, the radiation should be computed using the local electron temperature and nonequilibrium species concentrations, and the LTNE factors should not be used (or set to unity).

Discussion of Results

Inviscid and viscous results have been obtained for the stagnation region of a 2.3-m nose radius axisymmetric blunt body for a freestream velocity of 12 km/s at an altitude of 80 km. This condition was selected because it is within the range of possible Martian return trajectories, and yet the velocity is low enough that radiation losses should be minor, at the most a few percent, compared to the total flow energy. Thus, radiation cooling and gasdynamic coupling effects should be small. Each inviscid solution covers the region between the shock and the body and from the centerline up to 10 cm above the axis and is typically composed of over 10,000 computational points. Inviscid solutions using both air and nitrogen freestreams have been obtained. Viscous solutions have been obtained along the stagnation streamline for nitrogen freestreams for adiabatic and cool wall situations. In both cases the wall was assumed to be nonemitting and noncatalytic, and in the cool wall case the wall temperature was assumed to be 1650 K, which is representative of nonablating heat shield materials.

Inviscid Results

Although flowfield properties along 21 different streamlines in the stagnation region were actually computed, details will only be presented for streamline C, which crossed the shock front 1.5 cm above the axis. This streamline is shown in Fig. 3 as a solid line, along with several other streamlines, the shock front, and the body. Depending on the reaction chemistry system, streamline C was typically composed of 700–2000 spatial grid points.

Figure 4 shows air results obtained using the one-step ionization model with case 1 rates, the quasiequilibrium electron temperature model, and MCVDV vibration dissociation coupling. Although individual vibrational temperatures were computed for N_2, O_2, NO, NO^+, and N_2^+, for clarity they are not included on the plots. Immediately behind the shock front, the heavy particle temperature T is almost 70,000 K, whereas the electron temperature T_e is at the freestream value, 180.65 K. Initially, T_e rapidly rises to about 10,000 K, whereas the heavy particle temperature falls sharply due to the rapid

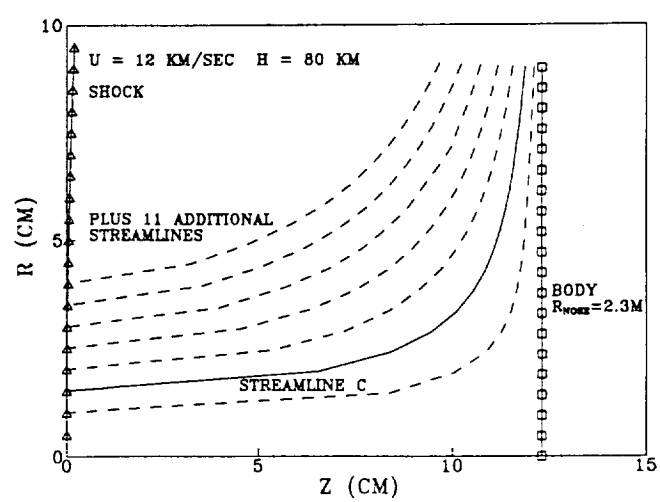

Fig. 3 Solution region for inviscid cases showing streamline C.

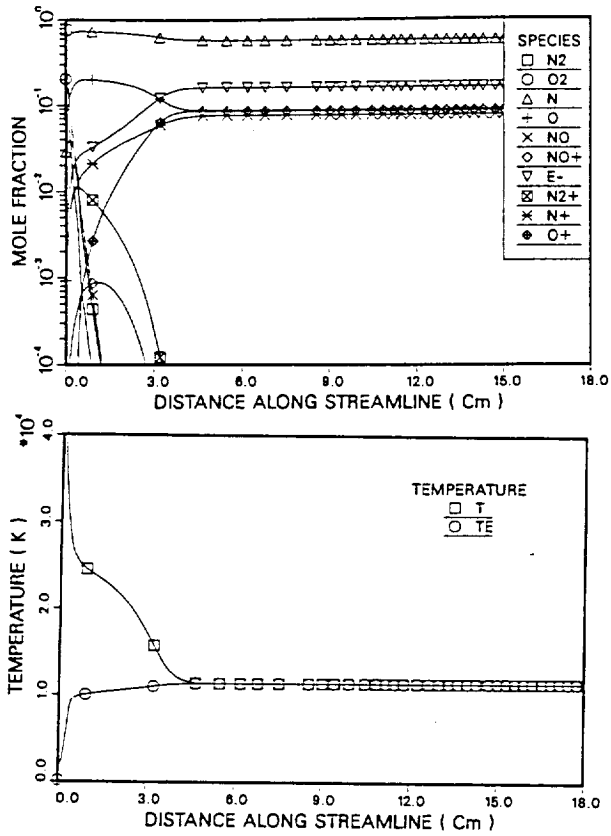

Fig. 4 Species and temperature profiles for air along streamline C, inviscid flow, case 1.

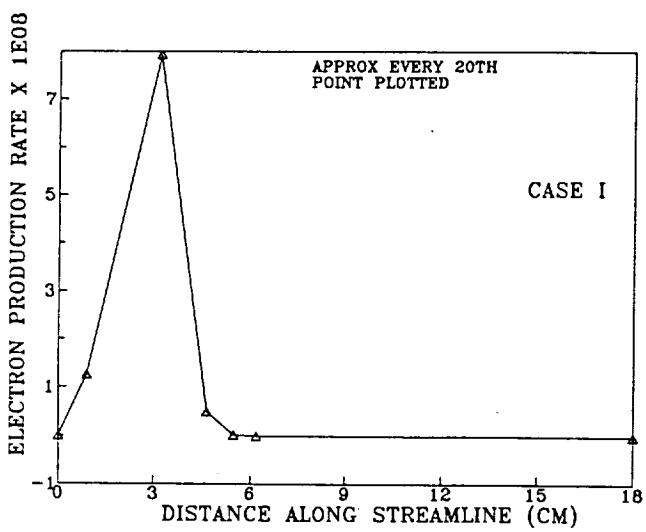

Fig. 5 Electron mass production rate along streamline C, inviscid case 1.

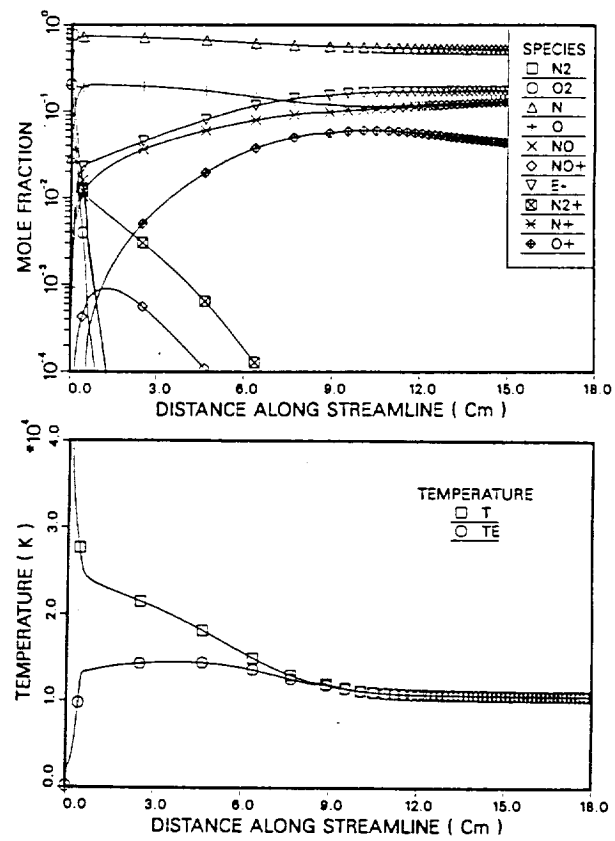

Fig. 6 Species and temperature profiles for air along streamline C, inviscid flow, case 2.

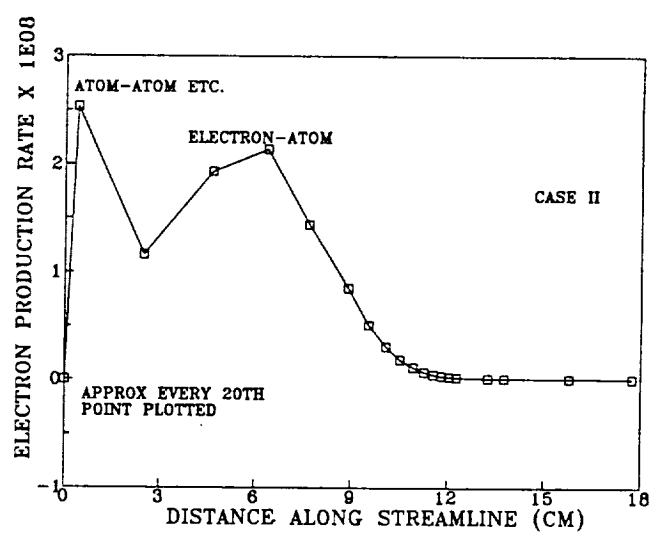

Fig. 7 Electron mass production rate along streamline C, inviscid case 2.

dissociation of N_2 and O_2. Subsequently, the electron temperature gradually increases until it equilibrates with the heavy particle temperature.

As can be seen on the concentration profiles, in the region immediately behind the shock front the concentration of atomic nitrogen and oxygen rises extremely rapidly, indicating that dissociation essentially occurs in the shock "front" as has been assumed in some approximate solutions.[25,34] Also N_2^+, NO, and NO^+ peak rapidly and essentially "disappear," and from a practical standpoint the entire nonequilibrium portion of the flowfield is dominated by atomic ionization. Interestingly, at the end of the equilibrium zone, the concentrations of N^+ and O^+ are similar. Furthermore, the heavy particle temperature and $[e^-]$ profiles exhibit a change in curvature around 2.5 cm, which is associated with the onset of electron avalanche from the electron impact ionization reactions.

The magnitude of this phenomena is shown in Fig. 5, which portrays the total electron production rate [in g/(cm^3-s)] for this case. Although the plot is somewhat lacking in detail since only approximately every twentieth point is plotted, it can be seen that avalanche starts at about 1 cm along the streamline. Apparently, by this point other ionization reactions have produced sufficient electrons, and the electron temperature has risen sufficiently to permit electron impact ionization to dominate. Both Figs. 4 and 5 indicate that for the case 1 rates the flow equilibrates in about 4.5 cm. It should be noted that the high electron production rate associated with the case 1 impact ionization rates prevents the free electron temperature from peaking and instead leads to its gradual rise until equilibrium is attained.

Inviscid results obtained using the two-step approximate ionization model with case 2 rates are shown for air in Figs. 6

and 7. The [N] and [O] profiles indicate rapid dissociation and are similar to those with the one-step model shown in Fig. 4. Likewise, the peak values for $[N_2^+]$ and $[NO^+]$ are similar but occur slightly later. The electron temperature initially rises to about 14,000 K, after which it remains relatively constant until it equilibrates with the heavy particle temperature. As can be seen by comparing the values in Figs. 7 and 5, the electron production rate for this case is significantly lower than that for the case 1 situation, and as a result the electron temperature is higher over most of the nonequilibrium region.

The biggest difference, however, between the case 1 and case 2 air results is in the behavior and length of the atomic ionization region. After the initial dissociation, the decrease in heavy particle temperature and increase in electron concentration is, by comparison, slow, and equilibrium is not achieved until 11 cm along the streamline. In addition, the $[N^+]$ concentration is significantly higher than the $[O^+]$ value. This latter difference is due to the fact that in this case the equilibrium composition is determined from the equilibrium coefficient computed by partition functions, whereas for the one-step case 1 rates it is specified by the ratio of the forward and reverse rates in Eqs. (2-5). At the present equilibrium temperatures, these two approaches yield equilibrium constants that differ by an order of magnitude, with resultant differences in final composition and temperatures.

In addition, Fig. 7 shows that the electron production rate for the two-step ionization model is different from that for the one-step case. Initially, electrons are created due to NO^+, N_2^+, atom-atom, and atom-ion reactions, and the production from these reactions rapidly peaks and then decreases. However, once $[e^-]$ becomes sufficiently high, electron-atom processes become important, the electron production rate increases, and electron avalanche occurs. However, since the two-step electron-atom ionization rate is less, the process is slower than in the one-step model and the time and distance to equilibrium is longer.

It is believed that these inviscid results demonstrate that predictions of ionization relaxation are strongly dependent on the atomic ionization model and the electron impact ionization rate.

Viscous Results

Using the nitrogen reaction chemistry set given in Table 2, viscous results have been obtained for the stagnation streamline with the modified VSL3DNQ code. In all cases, 99 points have been used between the shock front and the wall, and binary diffusion between molecular and atomic species has been included. Unlike the inviscid solver, which primarily used the partition function approach, the thermodynamic properties in the viscous solutions were computed using the curve fits presented by Gnoffo et al.[40]

Figure 8 shows temperature and concentration profiles for the cool wall case (T_w = 1650 K) for the case 1 electron impact ionization rate. Notice that computational points have been clustered in the region immediately behind the shock front where nonequilibrium effects should be important and in the region near the wall where thermal and concentration gradients could be large. In the outer portion of the shock layer, these results are almost identical to the equivalent inviscid case in that dissociation is rapid behind the shock front, the electron temperature "peaks" and then gradually rises to equilibrate with the heavy particle temperature, and about two-thirds of the shock layer is in chemical equilibrium. In addition, the results show that the cool wall thermal layer affects about 20% of the shock layer and that in this region ion and molecular recombination processes are dominant. For this case the shock standoff distance was 11.8 cm and the computed convective heating rate to the noncatalytic wall was 46.7 W/cm^2.

Stagnation profiles for the two-step ionization model and the case 2 electron impact ionization are presented in Fig. 9. For the nonequilibrium zone behind the shock front, the dissociation is rapid and N_2^+ rapidly peaks and disappears; two-thirds or more of the shock layer is affected by ionization nonequilibrium relaxation. In addition, the relaxing temperature profile never reaches a constant plateau but smoothly merges into the wall thermal layer. For this case the shock detachment length was 12.0 cm and the convective heating was 44.4 W/cm^2.

The electron production rate for this cool wall case is presented in Fig. 10. Although there are some differences between this profile and the inviscid curve shown in Fig. 7 due to

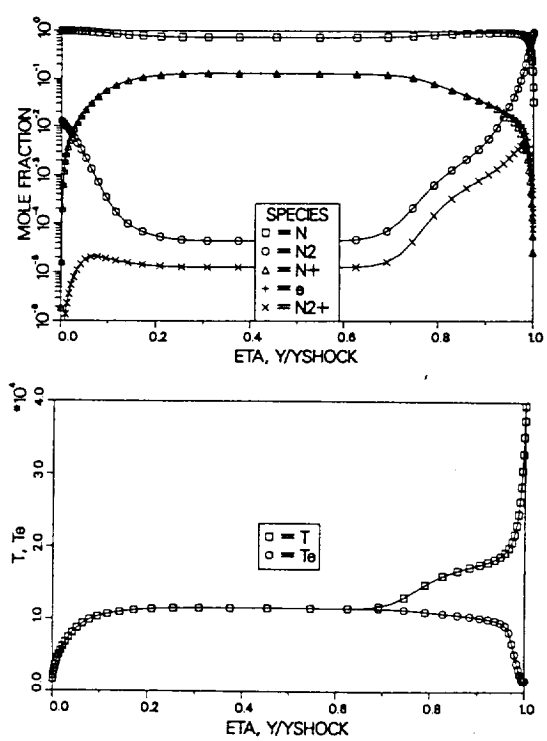

Fig. 8 Stagnation streamline species and temperature profiles, viscous case 1.

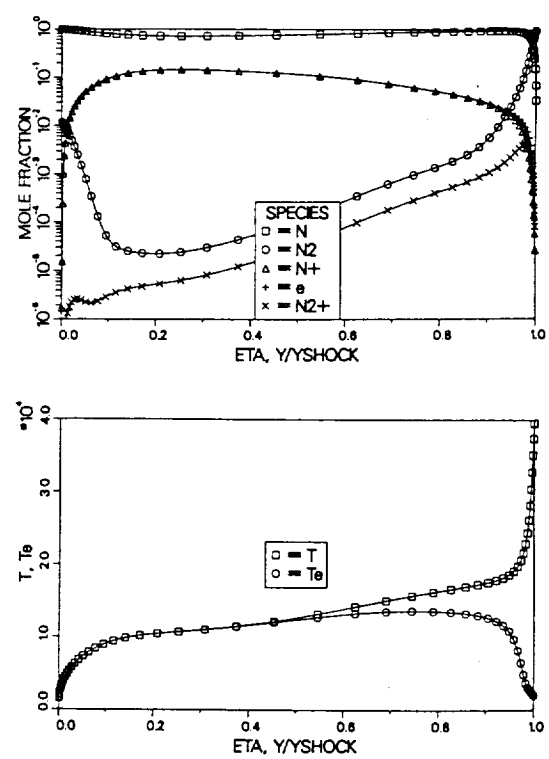

Fig. 9 Stagnation streamline species and temperature profiles, viscous case 2.

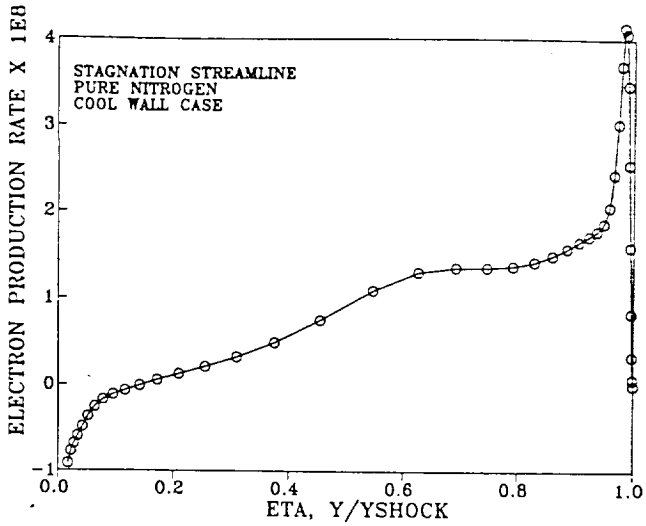

Fig. 10 Stagnation streamline electron mass production rate, viscous flow, case 2.

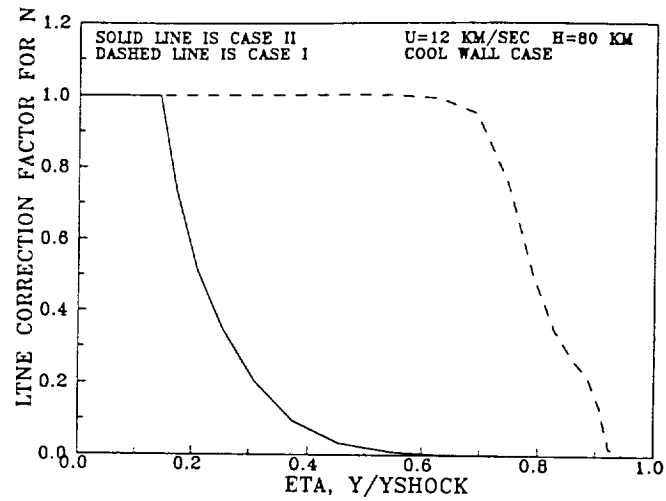

Fig. 11 Nonequilibrium radiation correction factors along stagnation streamline.

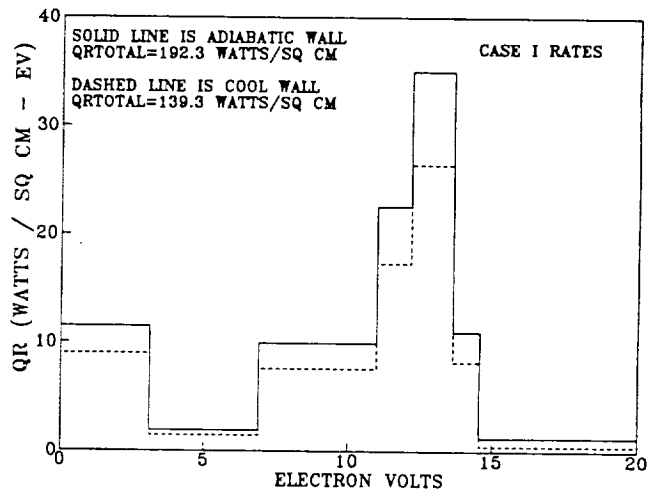

Fig. 12 Stagnation-point radiative heat transfer for case 1.

differences in velocity along and location of the streamlines, the overall pattern is similar. Initially, electron production is high due to N_2^+ ionization, atom-atom, and atom-ion reactions, and then it decreases. Subsequently, electron-atom ionization becomes important, as evidenced by the plateau around y/yshock of 0.8, followed by an approach toward equilibrium. Unlike Fig. 8, no second peak appears in the viscous profile, possibly due to diffusion effects and to the influence of the charge exchange reaction. Also, the electron production rate indicates that an equilibrium region is never achieved along the stagnation streamline, but that the flow simply transitions from an ionizing flow to one involving recombination (negative production rates) in the wall thermal layer.

Obviously, the different species concentration and temperature profiles between the case 1 and case 2 models and rates will greatly influence the predicted radiative heat transfer to the vehicle surface, since radiative heating depends on both electron temperature and species concentrations. However, it also depends on the extent of radiative nonequilibrium or the degree to which the excited state populations are depleted due to ionization. This nonequilibrium has previously been referred to as local thermodynamic nonequilibrium (LTNE) in the discussion concerning the radiation model, and it can be approximately accounted for via LTNE correction factors such as those in Eqs. (28) and (29).

Values for the correction factors for atomic nitrogen radiation are shown in Fig. 11 for both the case 1 and case 2 rates and models. For the one-step case 1 model, the correction factor is small in the chemical nonequilibrium zone, but then it rises rapidly and is essentially unity through the rest of the stagnation layer. Thus, for the one-step impact ionization model most of the shock layer is in local thermodynamic equilibrium radiatively. Similarly, the two-step case 2 factors are also very small in the chemical nonequilibrium zone, but they subsequently increase only slowly, and only very near the body in the wall thermal layer do they become one. Hence, for the case 2 flowfield, radiative nonequilibrium or LTNE effects are very important. Interestingly, when the approximate technique of Ref. 34 is applied to this case, it also predicts that most of the stagnation region is in LTNE.

In examining these results it should be realized that the two-step ionization chemistry and LTNE radiation models are approximate and are the most optimistic from the standpoint of reducing radiation and the rate of ionization, since they assume that the excited states are in equilibrium with the ions and free electrons. In actuality, the rate of ionization from the excited state, Eq. (11), may be finite, and the extent of LTNE indicated by the case 2 results on Fig. 11 may be less. Thus, the two sets of results in Fig. 11 could be viewed as bracketing the problem.

Stagnation-Point Radiative Heat Transfer

The viscous stagnation streamline nonequilibrium flowfields have been used to compute the radiative heat transfer to the wall. In all cases the wall has been assumed to be nonemitting and nonablating, and results have been obtained for both an adiabatic and the cool wall case. Considering the many factors involved in the current models, these radiative heating results should not be construed as definitive and should be used primarily for comparison purposes and model development until they have been verfied by more detailed models and/or experiments. Nevertheless, these results do include both the ultraviolet and the visible-infrared spectrum, emission and absorption phenomena, the variation of absorption coefficients with wavelength, chemical and thermal nonequilibrium, and radiative nonequilibrium. Thus, the present results include many effects not accounted for in other studies,[8] which assumed the gas cap to be in equilibrium and transparent and only included emission in the visible and infrared (IR) spectrum.

Figures 12 and 13 present stagnation-point radiative heat transfer for the present cases as a function of energy, and several significant points are evident. First, there is an order of magnitude difference in heat transfer both totally and in the individual spectral regions between the one-step case 1 flowfield and the two-step case 2 results. This difference is due to the larger chemical nonequilibrium region predicted by the

case 2 rates and the subsequent greater extent of the radiative nonequilibrium zone. Second, for both ionization models most of the radiation reaching the wall for the region below 6.89 eV (above 1800 Å), which is often referred to as the visible region since it is optically visible through quartz and sapphire windows, is in the region below 3.1 eV and is due to IR continuum and lines.

Third, the absorption effects of the cool wall thermal layer may not be as great as previously hoped.[5,8,33] With the present data, the effect of the wall thermal layer can be determined by comparing the cool wall results with the adiabatic wall values. For the case 1 situation in Fig. 12, lowering the wall temperature to 1650 K reduces the overall radiative heating 28%, and in the separate spectral bands the reduction is 22–25%, except for the VUV band from 14.56–31 eV. For that band the reduction is 61%, indicating that the far vacuum ultraviolet is extensively absorbed in the cool wall layer. Likewise, for the case 2 rates, Fig. 13 shows a reduction due to wall cooling of 46% in the total radiative heating. In this case, since the total input is considerably less than that for the one-step model, the thermal boundary layer has more of an effect. In the individual bands the reduction ranges from 39 to 44%, but again in the 14.56–31-eV VUV band the reduction is large (72%). Obviously, for both cases, although a cool wall significantly attenuates the far VUV and somewhat reduces the heating from other regions of the spectrum, significant radiative heat transfer still reaches the wall. This trend is consistent with previous approximate calculations at similar conditions.[34]

Fourth, there is significant radiative heat input to the wall from the spectral region above 6.89 eV (below 1801 Å). In fact, for both ionization models approximately 75% of the total radiative heating is from this region. This result is consistent with what has been observed and predicted for the Fire 2 experiment,[1,33,41] and it is also consistent with the shock-tube experiments of Wood et al.[42] Wood and co-workers conducted measurements with and without a quartz window and determined that 50–75% of the total radiant intensity was from the ultraviolet region of the spectrum. Interestingly, they also concluded from their experiments that a cool boundary layer would not absorb appreciably.

Comparison with Experimental Data

Based on the temperature, species, and radiative heat transfer profiles discussed earlier, it is apparent that the choice of ionization model and electron impact ionization rate greatly affects the resultant predictions, and it would be desirable to determine which model is more appropriate for blunt-body calculations. Although there is almost no radiation experimental data at the present velocity and pressure conditions, Wilson[25] did make measurements of the ionization rate of air behind shock waves having velocities between 9 and 12.5 km/s. By making IR measurements at around 6.1 μ, he was able to determine variations in electron density and thus the ionization relaxation distances.

Consequently, the concentration and temperature profiles for the present inviscid air data along streamline C have been used to compute theoretical IR emission profiles similar to those measured by Wilson for both the case 1 and case 2 models. These profiles are shown in Fig. 14 and have the same general shape as the signals measured by Wilson. Following his procedure the intercept with the equilibrium value of a line drawn through the maximum slope of the rising signal has been used to determine an ionization distance, denoted by the vertical dashed line on the figure, for each ionization model. Then the shock-tube data of Wilson have been used, accounting for differences in freestream pressure and for particle velocity differences behind a normal shock and along streamline C, to determine an experimental ionization distance for the present case. These distances are shown by the square symbols on Fig. 14. The center symbol is the nominal value, whereas the endpoints correspond to the data scatter and error band limits indicated in Ref. 25. As can be seen, the agreement between the shock-tube data and the prediction obtained using the two-step ionization model and the case 2 electron impact ionization rates is very good. Thus, it appears that a two-step ionization model in conjunction with ionization reaction rates based on forward processes should be used for the computation of nonequilibrium blunt-body flowfields associated with Earth aerocapture from Mars.

However, this conclusion does not mean that the ion recombination rates used by Kang et al.[11] or measured by Park[17] are in error. Unfortunately, there are many possible explanations for the observed differences. First, there could be an error in the experimental data[25] or its interpretation to the present problem. Second, at the current electron densities and temperatures, the results of Hinnov and Hirschberg[19] and of Bates et al.[43] indicate that the effective recombination rate is not strictly a function of electron temperature and that radiative recombination is still significant. Thus, the flow may not be totally collision-dominated. In such a situation, if a measured or effective reverse rate were used via an equilibrium constant to determine a forward rate, the resulting forward rate would be too large. As pointed out by Park,[18,44,45] the effective forward and reverse rates are only related via the equilibrium constant if the flow is collision-dominated. Third, there is the possibility[18] that, in the region immediately behind the shock front and due to the time scales involved, the forward and reverse rates are not related by the equilibrium constant and reasonable chemistry can only be predicted using a proper forward rate. Fourth, there exists the possibility that the elec-

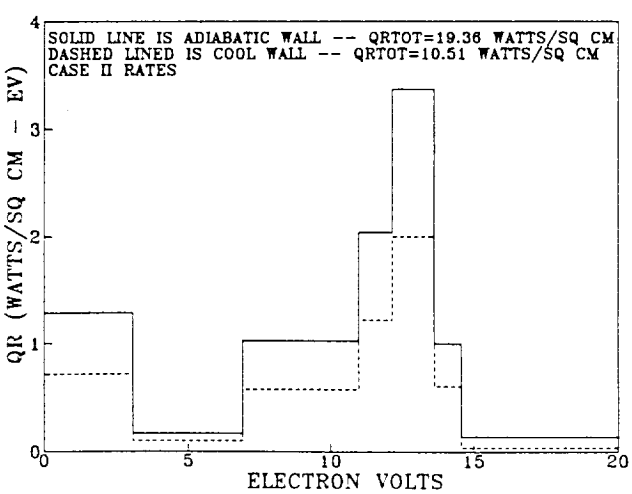

Fig. 13 Stagnation-point radiative heat transfer for case 2.

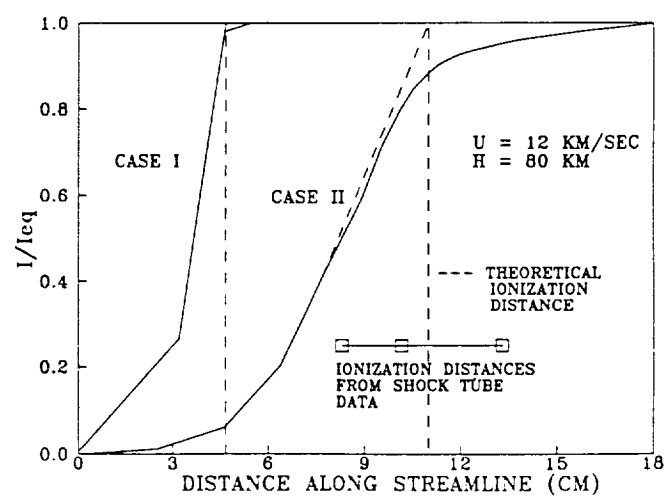

Fig. 14 Theoretical emission profiles and ionization distances for streamline C.

tronic temperatures are not in reality the same as the free electron temperature, and this fact requires the use of a different set of rates. A discussion of this situation and also of the details of atomic ionization are presented in Refs. 45 and 46. Finally, as mentioned previously, there exists the possibility that ionic recombination in a nozzle or arc tunnel is not the direct inverse of atomic ionization behind a shock wave. If anything, the present results indicate the difficulty of creating engineering models for these problems and the need for further analytical and experimental investigation. Nevertheless, based on the results presented here and the reaction rates discussed in Ref. 47, it is believed that the present two-step model with case 2 rates is appropriate for stagnation region computations.

Future Efforts

In the near future there are plans to continue these studies by developing a nonequilibrium radiation model based upon RADICAL. This new model will be incorporated into the VSL code along with radiation gasdynamic coupling. In addition, there exists a need to improve the ionization chemistry model and the LTNE correction factors by taking into account finite-rate processes between excited state atoms and ions. Also, there is a definite need for additional experimental data at velocities and pressures appropriate for a Mars return AOTV. This data should be for an ionizing, as opposed to a recombining, flow and probably could be obtained in a shock tube, although flight data would be desirable. Finally, the inclusion of preshock precursor, photoionization and recombination, and shock and wall slip effects would be desirable.

Conclusion

Based on the results presented, it appears that an approximate two-step ionization model in conjunction with quasiequilibrium electron temperature model is suitable for the computation of nonequilibrium blunt-body flowfields associated with Earth aerocapture from Mars. Also, nonequilibrium chemical and radiation effects are important at these conditions throughout the entire stagnation zone, and, compared to equilibrium predictions, these nonequilibrium phenomena can lead to a reduction in radiative heating. Furthermore, compared to an adiabatic wall, a cool wall results in a significant reduction in radiative heating due to absorption near the wall. However, the present results also indicate a need for further analytical and experimental investigations.

Acknowledgments

The authors gratefully acknowledge the assistance of the Associate Provost for Computing for providing a portion of the computational resources used in this effort. This work was initiated under a subportion of NASA Grant NAG 9-192 from the NASA Johnson Space Center (JSC). The authors thank the technical monitor, Carl Scott, Aerosciences Branch, JSC, for his suggestions, and Ken Sutton, Aerothermodynamics Branch, NASA Langley Research Center, for his comments and assistance in providing the RADICAL and VSL3DNQ programs. T. A. Gally is partially supported by a NASA Graduate Student Researchers Fellowship through the NASA Johnson Space Center.

References

[1]Sutton, K., "Air Radiation Revisited," *Progress in Astronautics and Aeronautics: Thermal Design of Aeroassisted Orbital Transfer Vehicles*, Vol. 96, edited by H. F. Nelson, AIAA, New York, 1985, pp. 419–441.

[2]Moss, J. N., Bird, G. A., and Dogra, V. K., "Nonequilibrium Thermal Radiation for an Aeroassist Flight Experiment Vehicle," AIAA Paper 88-0081, Jan. 1988.

[3]Gnoffo, P. A., and Green, F. A., "A Computational Study of the Flowfield Surrounding the Aeroassist Flight Experiment Vehicle," AIAA Paper 87-1575, June 1987.

[4]Park, C., "Assessment of Two Temperature Kinetic Model for Ionizing Air," AIAA Paper 87-1574, June 1987.

[5]Candler, G., and Park, C., "The Computation of Radiation from Nonequilibrium Hypersonic Flows," AIAA Paper 88-2678, June 1988.

[6]Carlson, L. A., Bobskill, G. J., and Greendyke, R. B., "Comparison of Vibration Dissociation Coupling and Radiative Heat Transfer Models for AOTV/AFE Flowfields," AIAA Paper 88-2673, June 1988.

[7]Li, C. P., and Wey, T.C., "Numerical Simulation of Hypersonic Flow Over an Aeroassist Flight Experiment Vehicle," AIAA Paper 88-2675, June 1988.

[8]Park, C., and Davies, C. B., "Aerothermodynamics of Manned Mars Mission," AIAA Paper 89-0313, Jan. 1989.

[9]Grosse, W. L., "A Thin Shock Layer Solution for Nonequilibrium, Inviscid Flows in Earth, Martian, and Venusian Atmospheres," NASA TN D-6529, Dec. 1971.

[10]Thompson, R. A., "Comparison of Nonequilibrium Viscous Shock Layer Solutions with Windward Surface Shuttle Heating Data," AIAA Paper 87-1473, June 1987.

[11]Kang, S. W., Jones, W. L., and Dunn, M. G., "Theoretical and Measured Electron Density Distributions at High Altitudes," *AIAA Journal*, Vol. 11, No. 2, 1973, pp. 141–149.

[12]Zeldovich, Y. B., and Raizer, Y. P., *Physics of Shock Waves and High Temperature Hydrodynamic Phenomena*, Academic, New York, 1966, pp. 407–413.

[13]Makin, B., and Keck, J. C., "Variational Theory of Three-Body Electron Ion Recombination Rates," *Physical Review Letters*, Vol. 11, No. 6, Sept. 15, 1963, pp. 281–283.

[14]Dunn, M. G., "Measurement of $C^+ + e^- + e^-$ and $CO^+ + e^-$ Recombination in Carbon Monoxide Flows," *AIAA Journal*, Vol. 9, No. 11, 1971, pp. 2184–2191.

[15]Dunn, M. G., and Lordi, J. A., "Measurement of $O_2^+ + e^-$ Dissociative Recombination in Expanding Oxygen Flows," *AIAA Journal*, Vol. 8, No. 4, 1970, pp. 614–618.

[16]Dunn, M. G., and Lordi, J. A., "Measurement of $N_2^+ + e^-$ Dissociative Recombination in Expanding Nitrogen Flows," *AIAA Journal*, Vol. 8, No. 2, 1970, pp. 339–345.

[17]Park, C., "Measurement of Ionic Recombination Rate of Nitrogen," *AIAA Journal*, Vol. 6, No. 11, 1968, pp. 2090–2094.

[18]Park, C., "Collisional Ionization and Recombination Rates of Atomic Nitrogen," *AIAA Journal*, Vol. 7, No. 8, 1969, pp. 1653–1654.

[19]Hinnov, E., and Hirschberg, J. G., "Electron-Ion Recombination in Dense Plasmas," *Physical Review*, Vol. 125, No. 3, 1962, pp. 795–801.

[20]Nelson, H. F., and Goulard, R., "Structure of Shock Waves with Nonequilibrium Radiation and Ionization," *Physics of Fluids*, Vol. 12, No. 8, 1969, pp. 1605–1617.

[21]Chapin, C. E., "Nonequilibrium Radiation and Ionization in Shock Waves," Purdue Univ., Lafayette, IN, AA&ES Rept., June 1967.

[22]Foley, W. H., and Clarke, J. H., "Shock Waves Structured by Nonequilibrium Ionizing and Thermal Phenomena," *Physics of Fluids*, Vol. 16, No. 3, 1973, pp. 373–383.

[23]Vinolo, A. R., and Clarke, J. H., "Interrelated Structures of the Transport Shock and Collision Relaxation Layer in a Multitemperature, Multilevel Ionized Gas," *Physics of Fluids*, Vol. 16, No. 10, 1973, pp. 1612–1620.

[24]Zeldovich, Y. B., and Raizer, Y. P., *Physics of Shock Waves and High Temperature Hydrodynamic Phenomena*, Academic, New York, 1966, pp. 382-396, 505-515.

[25]Wilson, J., "Ionization Rate of Air Behind High Speed Shock Waves," *Physics of Fluids*, Vol. 9, No. 10, 1966, pp. 1913–1921.

[26]Carlson, L. A., "Radiative Gasdynamic Coupling and Nonequilibrium Effects Behind Reflected Shock Waves," *AIAA Journal*, Vol. 9, No. 5, 1971, pp. 858–865.

[27]Petschek, H., and Byron, S., "Approach to Equilibrium Ionization Behind Strong Shock Waves in Argon," *Annals of Physics*, Vol. 1, No. 3, 1957, pp. 270–315.

[28]Dix, D. M., "Energy Transfer Processes in a Partially Ionized Two Temperature Gas," *AIAA Journal*, Vol. 2, No. 12, 1964, pp. 2081–2090.

[29]Dix, D. M., "The Governing Macroscopic Equations of Partially Ionized Gases," Aerospace Corporation Rept. TDR-69-2330-04 TN-2, July 1962.

[30]Lee, J. H., "Basic Governing Equations for the Flight Regimes of Aeroassisted Orbital Transfer Vehicles," *Progress in Astronautics and Aeronautics: Thermal Design of Aeroassisted Orbital Transfer Vehicles*, Vol. 96, edited H. F. Nelson, AIAA, New York, 1985, pp. 3–53.

[31]Carlson, L. A., "Radiative Cooling and Nonequilibrium Chemistry Coupling Behind Normal Shock Waves," *AIAA Journal*, Vol. 10, No. 2, 1972, pp. 230–232.

[32]Tiwari, S. N., and Szema, K. Y., "Effects of Precursor Heating on Radiative and Chemically Reacting Viscous Flow Around a Jovian Entry Body," NASA CR-3186, Oct. 1979.

[33]Gupta, R. N., "Navier Stokes and Viscous Shock Layer Solutions for Radiating Hypersonic Flows," AIAA Paper 87-1576, June 1987.

[34]Carlson, L. A., "Approximations for Hypervelocity Nonequilibrium Radiating, Reacting, and Conducting Stagnation Regions," AIAA Paper 88-2672, June 1988.

[35]Carlson, L. A., and Rieper, R. G., "Electron Temperature and Relaxation Phenomena Behind Shock Waves," *Journal of Chemical Physics*, Vol. 57, No. 2, 1972, pp. 760–766.

[36]Carlson, L. A., "Expressions for the Exchange of Energy and Momentum Between Gases at Different Temperatures and Velocities," *Physics of Fluids*, Vol. 13, No. 7, 1970, pp. 1869–1870.

[37]Olstad, W. B., "Nongray Radiating Flow about Smooth Symmetric Bodies," *AIAA Journal*, Vol. 9, No. 1, 1971, pp. 122–130.

[38]Nicolet, W., "User's Manual for the Generalized Radiation Transfer Code (RAD/EQUIL)," NASA CR-116353, Oct. 1969.

[39]Greendyke, R. B., Private Communication, Analytical Methods and Services Corp., Hampton, VA, 1989.

[40]Gnoffo, P. A., Gupta, R. N., and Shinn, J., "Governing Equations and Physical Models for Hypersonic Air Flows in Thermal and Chemical Nonequilibrium," NASA TP-2867, 1989.

[41]Bird, G. A., "Nonequilibrium Radiation During Reentry at 10 km/sec," AIAA Paper 87-1543, June 1987.

[42]Wood, A. D., Hoshizaki, H., Andrews, J. C., and Wilson, K. H., "Measurements of the Total Radiant Intensity of Air," *AIAA Journal*, Vol. 7, No. 1, 1969, pp. 130–139.

[43]Bates, D. R., Kingston, A. E., and McWhirter, R. W. P., "Recombination Between Electrons and Atomic Ions. I. Optically Thin Plasmas," *Proceedings of the Royal Society of London, Series A*, Vol. 267, No. 1330, 1962, pp. 297–312.

[44]Park, C., "Spectral Line Intensities in a Nonequilibrium Nitrogen Plasma," *Journal of Quantitative Spectroscopy and Radiative Transfer*, Vol. 8, No. 10, 1968, pp. 1633–1653.

[45]Park, C., "Comparison of Electron and Electronic Temperatures in Recombining Nozzle Flow of Ionized Nitrogen-Hydrogen Mixture. Part 1. Theory," *Journal of Plasma Physics*, Vol. 9, No. 2, 1973, pp. 187–215.

[46]Kunc, J. A., and Soon, W. H., "Nonequilibrium of High Temperature Nitrogen and Oxygen," AIAA Paper 88-2779, June 1988.

[47]Park, C., "A Review of Reaction Rates in High Temperature Air," AIAA Paper 89-1740, June 1989.